

UNIVERSITÀ DI BOLOGNA

DOTTORATO DI RICERCA IN  
INGEGNERIA CIVILE, AMBIENTALE E DEI  
MATERIALI

XXVIII CICLO

SETTORE SCIENTIFICO-DISCIPLINARE ICAR/08

SETTORE CONCURSALE 08/B2

**First-order and buckling analysis  
of thin-walled members with  
deformable cross-section within  
the Generalized Beam Theory**

*Presentata da:*

Domenico MELCHIONDA

*Coordinatore Dottorato:*

Prof. Alberto LAMBERTI

*Relatore:*

Prof. Stefano DE MIRANDA

*Correlatore:*

Prof. Francesco UBERTINI

Prof. Viorel UNGUREANU

Esame finale anno 2016



To my family and Carla  
for their love, patience and encouragement.



# Contents

<b>Introduction</b>	<b>xvii</b>
<b>1 Mechanics of thin-walled members</b>	<b>1</b>
1.1 Cold-formed members . . . . .	1
1.2 Composite members . . . . .	8
1.3 Modeling framework . . . . .	14
<b>2 The shear deformable Generalized Beam Theory</b>	<b>23</b>
2.1 Shear deformable Generalized Beam Theory: from the original formulation to the last developments . .	24
2.2 Shear deformable Generalized Beam Theory: kine- matics . . . . .	29
2.2.1 Deformation modes . . . . .	32
2.3 Flexural formulation . . . . .	34
2.3.1 Generalized stresses and forces . . . . .	34
2.3.2 Generalized inertia forces . . . . .	37
2.3.3 Dynamic equilibrium equations . . . . .	38
2.3.4 Constitutive law . . . . .	39
2.3.5 Modal transformation . . . . .	40
2.4 Nonlinear warping formulation . . . . .	42

---

<b>3</b>	<b>Constitutive relations and consistency</b>	<b>45</b>
3.1	Strain field . . . . .	46
3.2	Kinematic constraints . . . . .	47
3.3	A new approach for constitutive relations . . . . .	49
3.3.1	Classical approaches . . . . .	49
3.3.2	An alternative unified approach . . . . .	51
3.4	Consistency . . . . .	53
3.5	Numerical examples . . . . .	58
3.5.1	Example 1: Shearing load . . . . .	60
3.5.2	Example 2: Distortional load . . . . .	63
<b>4</b>	<b>Flexibility-based GBT finite element</b>	<b>67</b>
4.1	Summary of the beam governing equations . . . . .	68
4.2	Analytical solutions . . . . .	70
4.2.1	Classic modes . . . . .	70
4.2.2	Higher-order modes . . . . .	75
4.3	Flexibility-based GBT finite element . . . . .	77
4.3.1	Variational framework . . . . .	78
4.3.2	Assumed stresses . . . . .	79
4.3.3	Finite element equations . . . . .	84
4.3.4	Recovery of the generalized displacements along beam axis . . . . .	85
4.4	Numerical tests . . . . .	86
4.4.1	Z-section cantilever beam . . . . .	87
4.4.2	Clamped-clamped rack-section beam . . . . .	90

---

4.4.3	Cantilever beam with non-conventional cross-section . . . . .	96
<b>5</b>	<b>EuroCode3-compliant design approach: ESA</b>	<b>113</b>
5.1	Design of thin-walled profiles according to EC3 . . .	114
5.1.1	EuroCode3 simplified and general methods . . .	114
5.1.2	ESA approach . . . . .	117
5.2	Stability check: ESA vs EC3 simplified method . . .	119
<b>6</b>	<b>GBT-based ECBL approach</b>	<b>127</b>
6.1	Erosion of Critical Bifurcation Load . . . . .	128
6.1.1	Classical ECBL approach . . . . .	129
6.1.2	Modified ECBL approach . . . . .	131
6.2	Numerical results . . . . .	132
6.2.1	Interaction points . . . . .	133
6.2.2	Erosion of buckling strength and ECBL buckling curves . . . . .	136
	<b>Conclusions</b>	<b>145</b>
	<b>Bibliography</b>	<b>149</b>



# List of Figures

1.1	Most common cold-formed cross-sections . . . . .	3
1.2	Z and C sections used as: a) purlins; b) girts. . . . .	3
1.3	Cold-formed sections used as primary structural elements. . . . .	4
1.4	Profiled sheets and linear trays . . . . .	4
1.5	Cold-formed roofing panels. . . . .	4
1.6	Composite concrete steel structure. . . . .	5
1.7	Stages in roll forming a single section . . . . .	6
1.8	Industrial roll forming lines. . . . .	6
1.9	Forming of folding . . . . .	6
1.10	Press braking process: a) Forming steps; b) Industrial brake press. . . . .	7
1.11	Evidence of flexural residual stresses in a lipped channel cold-formed steel section . . . . .	8
1.12	Examples of composite beams ( <a href="http://www.dragonplate.com">www.dragonplate.com</a> ). . . . .	10
1.13	a) FRP pedestrian bridge in Lleida, Spain; b) Aerofoil-powered generator (Hans Hillewaert). . . . .	10
1.14	Schematic of prepregging machine. . . . .	11

1.15	Assembly of prepreg bagged composite. . . . .	12
1.16	Aerospace autoclave. . . . .	12
1.17	Schematic of filament winding process ( <a href="http://www.nuplex.com">www.nuplex.com</a> ). . . . .	13
1.18	Schematic of pultrusion process ( <a href="http://www.nuplex.com">www.nuplex.com</a> ). . . . .	14
1.19	Buckling modes . . . . .	15
1.20	C-section: first 3 additional modes . . . . .	18
1.21	TE modelling approach . . . . .	19
1.22	LE modelling approach . . . . .	20
1.23	Finite strip discretization, strip DOFs. . . . .	21
2.1	Thin-walled cross-section. . . . .	25
2.2	Sketch of the main difference between classical shear deformable GBT and the present formulation: (a) undeformed elementary beam, (b) bending strain component, (c) corresponding shear strain component in the classical GBT, (d) corresponding shear strain component in the Timoshenko beam theory and in the present theory. . . . .	27
2.3	Deformation modes. (a) Out-of-plane displacement for fundamental flexural-shear: piecewise linear $\varphi$ ; (b) in-plane displacement for fundamental flexural-shear: $\boldsymbol{\mu} = -\partial_s \varphi$ and cubic $\psi$ ; (c) in-plane displacement for local flexural-shear: cubic $\psi$ (with null $\boldsymbol{\mu}$ and $\varphi$ ); (d) out-of-plane displacement for nonlinear warping: piecewise linear $\varphi$ (with null $\boldsymbol{\mu}$ and $\psi$ ). . . . .	33

---

2.4	Wall thickness resultants of bulk loads. . . . .	36
2.5	C cross-section: in- and out-of-plane displacements corresponding to the six fundamental flexural modes after modal decomposition. . . . .	44
3.1	Orthotropic case: material $(x_1, x_2, x_3)$ and wall $(z, s, n)$ reference systems. . . . .	51
3.2	C-section cantilever beam. . . . .	58
3.3	Loading conditions: (a) shearing load, (b) distor- tional load. . . . .	60
3.4	Example 1 - Deformed configurations obtained with the GBT by using settings $S4$ with refinement $C$ for various material orientations: (a) $0^\circ$ , (b) $30^\circ$ , (c) $60^\circ$ , (b) $90^\circ$ . . . . .	62
3.5	Example 2 - Deformed configurations obtained with the GBT by using settings $S4$ with refinement $C$ for various material orientations: (a) $0^\circ$ , (b) $30^\circ$ , (c) $60^\circ$ , (b) $90^\circ$ . . . . .	65
4.1	Z-section cantilever beam: (a) geometry; (b) self- equilibrated load; (c) torsional load. . . . .	87
4.2	Z-section cantilever beam: in-plane configurations of cross-section deformation modes. . . . .	88

4.3	Z-section cantilever beam with self-equilibrated load - Deformed shape: (a) reference solution; (b) GF- element (1 finite element); (c) GC-element (1 finite element). . . . .	89
4.4	Z-section cantilever beam with self-equilibrated load: $\bar{y}$ -displacement of natural node 1. . . . .	90
4.5	Z-section cantilever beam with self-equilibrated load - Classic generalized stresses: (a) $B$ ; (b) $T$ ; (c) $V_\phi$ . . . . .	91
4.6	Z-section cantilever beam with self-equilibrated load - Higher-order generalized stresses associated to mode 6: (a) $S_6$ ; (b) $M_6$ ; (c) $T_6$ ; (d) $V_6$ . . . . .	92
4.7	Z-section cantilever beam with torsional load - Clas- sic generalized stresses: (a) $B$ ; (b) $T$ ; (c) $V_\phi$ . . . . .	93
4.8	Z-section cantilever beam with torsional load - Higher- order generalized stresses associated to mode 6: (a) $S_6$ ; (b) $M_6$ ; (c) $T_6$ ; (d) $V_6$ . . . . .	94
4.9	Clamped-clamped rack-section beam: (a) geometry; (b) load applied at section A. . . . .	97
4.10	Clamped-clamped rack-section beam: in-plane con- figurations of cross-section deformation modes. . . . .	98
4.11	Clamped-clamped rack-section beam - Deformed shape: (a) reference solution; (b) GF-element (3 finite ele- ments); (c) GC-element (3 finite elements). . . . .	99
4.12	Clamped-clamped rack-section beam: $y$ -displacement of natural node 1. . . . .	101

4.13	Clamped-clamped rack-section beam - Classic generalized stresses: (a) $M_y$ ; (b) $V_x$ ; (c) $B$ ; (d) $T$ ; (e) $V_\phi$ . . . . .	103
4.14	Clamped-clamped rack-section beam - Higher-order generalized stresses associated to mode 5: (a) $S_5$ ; (b) $M_5$ ; (c) $T_5$ ; (d) $V_5$ . . . . .	104
4.15	Clamped-clamped rack-section beam - Higher-order generalized stresses associated to mode 9: (a) $S_9$ ; (b) $M_9$ ; (c) $T_9$ ; (d) $V_9$ . . . . .	105
4.16	Clamped-clamped rack-section beam - Higher-order generalized stresses associated to mode 15: (a) $S_{15}$ ; (b) $M_{15}$ ; (c) $T_{15}$ ; (d) $V_{15}$ . . . . .	106
4.17	Cantilever beam with non-conventional cross-section: (a) geometry; (b) loads applied at section A and section B. . . . .	107
4.18	Cantilever beam with non-conventional cross-section: in-plane configurations of cross-section deformation modes. . . . .	107
4.19	Cantilever beam with non-conventional cross-section: $\bar{x}$ -displacement of natural node 2. . . . .	108
4.20	Cantilever beam with non-conventional cross-section - Classic generalized stresses: (a) $M_y$ ; (b) $V_x$ ; (c) $M_x$ ; (d) $V_y$ ; (e) $B$ ; (f) $T$ ; (g) $V_\phi$ . . . . .	109

4.21	Cantilever beam with non-conventional cross-section - Higher-order generalized stresses associated to mode 5: (a) $S_5$ ; (b) $M_5$ ; (c) $T_5$ ; (d) $V_5$ . . . . .	110
4.22	Cantilever beam with non-conventional cross-section - Higher-order generalized stresses associated to mode 7: (a) $S_7$ ; (b) $M_7$ ; (c) $T_7$ ; (d) $V_7$ . . . . .	111
5.1	EC3 simplified method: a) Effective Width Method workflow, b) Effective Thickness Method workflow. . . . .	116
5.2	Cantilever beam: a) geometry, load and boundary conditions; b) $\alpha_{cr,op}^{GBT}$ , $\alpha_{cr,op}^{GBT_r}$ comparison. . . . .	120
5.3	ESA/EC3 stability check. . . . .	121
5.4	$\bar{\beta}$ parameter. . . . .	122
5.5	Buckling modes of C150x50x15x2 with length a) 500mm and b) 2000mm. . . . .	122
5.6	Buckling modes of C220x60x20x2 with length a) 1000mm and b) 2500mm. . . . .	123
5.7	Buckling modes of C280x70x25x2.5 with length a) 1500mm and b) 3000mm. . . . .	124
5.8	Buckling modes of C350x80x25x3 with length a) 1500mm and b) 3000mm. . . . .	125
6.1	Sketch of two mode interaction . . . . .	128
6.2	Interactive buckling model based on the ECBL ap- proach. . . . .	130
6.3	Variation of $\alpha_{th}$ depending on $\psi_{th}$ , $\bar{N}_{L/D,pr}$ and $\bar{N}_{L/D,th}$ . . . . .	133

6.4	Variation of $\alpha_{th}$ depending on $\psi_{th}$ and $\bar{N}_{L/D,pr}$ for a) $\bar{N}_{L/D,th} = 0.1$ b) $\bar{N}_{L/D,th} = 1.0$ c) $\bar{N}_{L/D,th} = 2.0$ . . .	134
6.5	Variation of $\alpha_{th}$ depending on $\psi_{th}$ and $\bar{N}_{L/D,th}$ for a) $\bar{N}_{L/D,pr} = 0.1$ b) $\bar{N}_{L/D,pr} = 0.5$ c) $\bar{N}_{L/D,pr} = 1.0$ . . .	135
6.6	Theoretical buckling curves for RSB125x3.2: a) GL and b) GD. . . . .	137
6.7	Theoretical buckling curves for RSB95x2.6: a) GL and b) GD. . . . .	138
6.8	Failure mode for RSB125x3.2 in a) $C_{th}$ and b) $C_{pr}$ . .	141
6.9	Failure mode for RSB95x2.6 in a) $C_{th}$ and b) $C_{pr}$ . . .	142
6.10	a) Theoretical buckling curves for RSB125x3.2 and b) buckling strength curves for RSB125x3.2. . . . .	143
6.11	a) Theoretical buckling curves for RSB95x2.6 and b) buckling strength curves for RSB95x2.6. . . . .	144



# List of Tables

3.1	FFS modes - Degree of the $s$ variable in the polynomial representation of strain and stress components.	56
3.2	LFS and NLW modes - Degree of the $s$ variable in the polynomial representation of strain components. The symbol 'pw' indicates piecewise polynomial representations. . . . .	56
3.3	Mechanical properties of the adopted orthotropic material. Young and shear moduli are expressed in $MPa$ .	59
3.4	Numerical results for Example 1. . . . .	61
3.5	Numerical results for Example 2. . . . .	64
4.1	Z-section cantilever beam with self-equilibrated load. $\bar{x}$ - and $\bar{y}$ -displacement of natural node 1 at $z/L = 1$ and strain energy $\Phi$ of the beam. . . . .	90
4.2	Z-section cantilever beam with self-equilibrated load. Generalized stresses at $z/L = 1$ . . . . .	95
4.3	Z-section cantilever beam with torsional load. Generalized stresses at $z/L = 1$ . . . . .	96

4.4	Clamped-clamped rack-section beam. $x$ - and $y$ -displacement of natural node 1 at $z/L = 2/3$ and strain energy $\Phi$ of the beam. . . . .	96
4.5	Clamped-clamped rack-section beam. Classic generalized stresses at $z_1 = 0.65L$ and $z_2 = 0.68L$ . . . . .	97
4.6	Clamped-clamped rack-section beam. Higher-order generalized stresses at $z_1 = 0.65L$ and $z_2 = 0.68L$ . . . . .	100
4.7	Cantilever beam with non-conventional cross-section. $\bar{x}$ - and $\bar{y}$ -displacement of natural node 2 and strain energy $\Phi$ of the beam. . . . .	101
4.8	Cantilever beam with non-conventional cross-section. Generalized stresses at $z/L = 1$ . . . . .	102
6.1	Base material properties for studied sections (mean values). . . . .	136

# Acknowledgements

A sincere thanks to Stefano de Miranda for introducing and guiding me in the research world, for his constant support and his advices that helped me during my PhD and, for sure, will be a reference for the next years.

Thanks to Francesco Ubertini for his precious suggestions and also thanks to Antonio Madeo, an indispensable support during my researches.

Thanks to Dan Dubina and Viorel Ungureanu for hosting me in Timisoara and, together with the guys at the Department of Steel Structures, for sharing their knowledge and for giving me their hospitality.

Thanks, finally, to the LAMC and DIMES guys, their friendship is unique, unforgettable.



# Introduction

A thin-walled beam can be defined as a slender beam composed by several plates or shells connected together at their common edges: the plate thickness is assumed to be much smaller than the other representative dimensions of the cross-section, which, in turn, are small with respect to the beam length. Thin-walled beams enables to form freely the cross-section and, thus, maximize the mechanical properties of the material. Therefore, they have been used in sport and automotive industry, aerospace and civil engineering. A snowboard, a ski or poles can be mentioned as an example, as well as the crane girders, the structural components of automobiles, aircraft fuselages and wings, supporting structures of walls and roofs of large halls and warehouses. Thin-walled structural elements have several advantages, such as simple manufacturing technology, dimensional diversity and an optimized use of mechanical properties of the material due to ad hoc design of the cross-section, which also implies a low strength/weight ratio. On the other hand, due to their geometrical characteristics, thin-walled beams have a complex mechanical behaviour. In fact, such structures may operate in complex loading environment where combined axial, bending, shearing and

torsional loads, as well as cross-section distortions and local effects, are present. Such complex mechanical behaviour requires the development of an ad hoc analysis tools, both of theoretical, numerical and practical/design type. Some recent developments about these issues are presented in this thesis. In the following, the main topics discussed in the thesis are summarized, together with their framing into the state-of-the-art.

In the first chapter of the thesis the fabrication methods and the peculiarities of both cold-formed steel and composite thin-walled beams are outlined, together with a brief description of their use and history. After this introduction to the subject, some of the most relevant models formulated for thin-walled beams are introduced. As it is well known, classical beam models like Eulero-Bernoulli and Timoshenko models are not suitable for describing the complex kinematic of thin-walled members, and the theory of Vlasov [1], based on a description of the cross-section warping related to a non-uniform distribution of torsional rotation, was the first approach to the modeling of thin-walled beams. From this original model, considerable work has been done over the decades to enhance and extend the Vlasov theory by different methods, such as the incorporation of higher-order parameters in the displacement field. For example, Vlasov theory was the inspiring model for Kang and Yoo [2] who developed a model to study large displacement behaviour in curved beams. Other interesting contributions are those of Kim [3], Wilson [4] and Stavridis [5] that studied the vibration

and stability of thin-walled profiles. These are some examples of contributions aimed at enhancing and extending the Vlasov theory. However, these formulations maintain the basic Vlasov hypotheses like (i) the rigid cross-section in its own plane and (ii) the null shear deformability. About the second of these, Capurso [6, 7] extended the model of Vlasov to include the shear deformation over the cross-section midline by generalizing the description of warping. Then, the concept of generalized warping functions has been used further by many authors: Savoia [8, 9], Bauchau [10], De Lorenzis and La Tegola [11], Ferradi and Cespedes [12]. Other interesting contributions regarding the inclusion of shear deformability on Vlasov-like beam models for vibration and stability analysis are the works of Piovan [13], Gendy and Saleeb [14], and Kim [15]. However, beam models based on the kinematics of Vlasov fail to take into account the effects of cross-section distortion and local in-plane deformation of the walls. Much effort has been spent by many authors to solve this weakness. Carrera [16] developed the Carrera Unified Formulation (CUF) that provides, using an asymptotic method, two-dimensional (plate and shell) theories and one-dimensional (beam) theories able to take into account section distortions. Recently, Genoese et al. [17, 18] developed a generalized beam model splitting the 3D elasticity problem into a 2D discrete cross-section analysis and a variable parametrization along the beam axis including classical and high-order deformation modes. It is also worth to note the Finite Strip Method (FSM) and the Constrained Finite Strip

Method [19], a semi-analytical procedure that stands in between the classical Rayleigh-Ritz method and a Finite Element Method (FEM) solution able to take into account enriched warping description and in-plane section deformations.

In this context, the Generalized Beam Theory (GBT), originally proposed by Schardt [20, 21] in the 1980s, has been proven to be an effective way to consistently account for cross-section distortion along with the classical beam kinematics in a comprehensive fashion, by expressing the deformation of the member as the superposition of a series of cross-sectional modes (which are known beforehand) multiplied by unknown functions depending on the beam axial coordinate. Following the work of Schardt, many authors have contributed to the improvement of the GBT by extending it beyond its original formulation for open unbranched cross-sections [22, 23] and by adding nonlinear effects for the analysis of buckling problems [24, 25] or by presenting new formulations for the dynamic analysis of open-section members subjected to initial perturbations or acting loads [26]. Another interesting development on GBT is an improved beam element based on semi-analytical solutions [27]. Recently, the application of the GBT to analyze cold-formed roof systems has been presented in [28, 29], an effective equilibrium-based procedure for the reconstruction of the three-dimensional stresses in GBT members in [30], the discussion of analogies between the GBT and the constrained FSM in [31] and [32] and the analogies between the GBT and the Generalized Eigenvectors method in [33].

A formulation of the GBT for the elastic-plastic analyses of thin-walled members experiencing arbitrary deformations and made of non-linear materials has been developed in [34, 35] and used for the modal decomposition of equilibrium/collapse configurations in the context of an inelastic member analysis [36]. Moreover, a GBT-based method capable of identifying the modal participation of the fundamental deformation modes from a general buckling mode determined by using the FEM has been presented by Nedelcu in [37] for elements without holes and in [38] for perforated members. Following an opposite way, Casafont used the GBT to constraint FEM shell models [39]. The GBT has also been studied in case of variable cross-section members [40, 41]. Moreover, the selection of the cross-section deformation modes (usually referred to as cross-section analysis) has received extensive attention in the research community over the years. On this regard, in the spirit of the semi-variational method, an interesting approach that reverses the classical methodology of GBT cross-section analysis has been proposed in [42, 43].

Much attention has also been devoted to the shear deformability. Silvestre and Camotim [44]-[45] were the first to remove the Vlasov constraint of null shear deformation in the GBT, considering a constant warping displacement over the wall thickness. However it leads to a null shear strain between the direction of the beam axis and that orthogonal to the wall midline, not allowing an exact recovery of classical shear deformable beam theories. Recently, in

[46, 47], a new formulation of the GBT that coherently accounts for shear deformation has been presented. Guaranteeing a coherent matching between bending and shear strains components of the beam, the new formulation allows to clearly identify the classical degrees of freedom of the beam. This target is reached by introducing the shear deformation along the wall thickness direction besides that along the wall midline. The cross-section analysis procedure is now based on a unique modal decomposition for both flexural and shear modes, posing the attention on the mechanical interpretation of the deformation parameters in modal space. This new GBT formulation is adopted in the present work and described in the second chapter.

As well as many other structural models, the GBT-based beam model can be viewed as a one-dimensional model deduced from a parent three-dimensional one by the introduction a kinematic ansatz. Of course, depending on the kinematic ansatz, this can lead to a poor (or even null) representation of the three-dimensional strain components over the cross-section (i.e. in the co-dimension of the model) and, in turn, to an over-stiffening which limits the predictive capabilities of the beam model. Such behaviour has been well documented by Silva et al. in various papers, see for example [48–50]. In particular, in [48], it has been shown that the buckling load in some cases can be dramatically overestimated (up to 300%), by using improperly derived GBT finite elements. Indeed, this is a typical problem of structural models with constrained kinematics

and it is usually dealt with by properly adjusting the constitutive relationship. A remarkable example of this strategy is represented by shear correction factors usually employed in Timoshenko beams and in shear-deformable plate models. In the case of non-standard beam models, such an approach leads to some drawbacks. In particular, the value of such coefficients depends on the stress distribution on the cross-section so that, on one side, their value is problem dependent and, on the other, it might change from section to section. Also in GBT based models the problem is tackled by modifying the constitutive relations, by adopting a different treatment for the membrane part of the strain field (pertaining to the cross-section midline) and for the bending one (outside the cross-section midline). Moreover, in this respect, it should be noticed that in the GBT literature, this different treatment is carried out in a non-univocal way for isotropic and orthotropic beams. As it can be easily argued, the arbitrary adoption of two different constitutive relations for the membrane and the bending parts is not desirable. In fact, this way of proceeding on one side does not give a clear insight on the physical meaning of such an approach and, on the other side, it might lead to non-univocal choices if the displacement field is enriched or laminated beams considered. In order to overcome these difficulties, following the ideas presented in [51], an approach able to automatically identify constitutive relations consistent with the adopted kinematic hypotheses is presented in the third chapter of this work. In the proposed approach, constitutive relations are

obtained via complementary energy and there is no distinction between membrane and bending parts, nor isotropic and orthotropic materials. Indeed, the different treatment of the membrane and bending parts, as well as the alternative approach presented in the third chapter of this thesis, suffices to overcome the over-stiffening problems in the case of isotropic material, but does not in that of orthotropic material. In this case, in fact, due to the coupling introduced by the constitutive relationship it is necessary to ensure the coherence between the representations over the cross-section of the stress and strain components which, through energetic equivalence, contribute to the definition of the cross-section stiffness matrix. In this thesis, this idea is formalized in a rigorous analysis by means of the concept of consistency. This concept was early introduced by Prathap and his co-workers (see [52] and the references therein) with regards to the assumed displacement finite element model in constrained media elasticity. They showed that consistency offers a conceptual scheme to delineate some well-known deficiencies of the assumed displacement approach and suggests the way to construct variationally correct procedures to overcome these shortcomings [53, 54]. Later, the same concept was successfully extended to coupled problems [55–57] and used as formal basis to develop an integrated procedure to recover consistent stresses for displacement based finite elements [58]. The effectiveness of the arguments exposed are illustrated on some numerical examples.

From the numerical point of view, the solution of the GBT equa-

tions is typically obtained resorting to the finite element method. In particular, the standard assumed displacement (compatible) approach is usually followed. On the other hand, it is well known that mixed/hybrid stress approaches can yield higher performance and, in particular, higher accuracy in the stress evaluation. Mixed/hybrid stress approaches have been successfully used for the analysis of beams (see, for example, [59, 60]) as well as of plates (see, for example, [61, 62]). In the fourth chapter of the thesis, following the ideas presented in [63], a 2-node flexibility-based GBT finite element is developed. The element formulation is based on the hybrid complementary energy functional, involving nodal displacements and equilibrating stresses within each element as independent variables. Assumed stresses can be discontinuous at the element boundaries and the stress parameters can be eliminated at the element level. Thus, the resultant discrete equations take the simple form of standard assumed displacement elements. As it is well known, the choice of the stress approximation is a crucial issue in developing reliable assumed stress finite elements. Here this is pursued based on a rational approach. Firstly, analytical solutions of the GBT equations referred to some particular cases are derived. Then, these are used to set-up the initial element stress approximation, assumed as an appropriate uncoupled expansion based on the stresses associated to the analytical solutions. Finally, stresses are constrained to satisfy the equilibrium equations pointwise. Of course, assumed stresses depend on the number of modes used to describe the kine-

matics of the GBT beam. However, this is automatically accounted for. Regarding the displacements, as anticipated, the element formulation involves only nodal displacements, hence no displacement approximation within the element is required. The displacement in the interior of the element is recovered a posteriori, interpolating nodal values by shape functions based on the same analytical solutions used to derive the stress approximation. The performance of the proposed element is tested on several numerical examples, involving beams under different loading conditions. Numerical results show that the element exhibits high accuracy in the evaluation of both displacements and generalized stresses. The reference solution is accurately predicted using very rough meshes, often one or two finite elements.

In the field of Civil Engineering, thin-walled beams are usually made by cold-forming of steel laminates. From a practical point of view, thin-walled cold-formed profiles are commonly classified as Class 4 in the current standards [64–68]. The design of Class 4 members is more complex with respect to the design of their hot-rolled counterparts, and this probably still nowadays impedes an even more large usage of these profiles. Designing against local and lateral-torsional buckling (the latter is here named “global buckling”) is a task well covered by reliable methods available in many international codes. Designing against distortional buckling can be more complicated, and rules provided by codes (for instance EC3 [65]) are not always applicable. The structural theory, or the numer-

ical tool, adopted for performing the linear buckling analysis deeply influences the design approach. In the fifth chapter, following the main steps presented in [69], a new design approach based on the EC3 “general method” (point 6.3.4 of [65]), is presented. This approach is named Embedded Stability Analysis (ESA) to underline the fact that embeds a stability analysis of the members to be verified. In particular, the stability analysis is based on the GBT, that allows to coherently consider distortional buckling together with local and global ones. The ESA approach is compared with current EC3 design methods and, in order to highlight its peculiarities, the results of an extensive numerical campaign are shown.

When dealing with buckling, an important issue that must be considered is that actual buckling curves are always conditioned by the erosion of ideal buckling curves. In case of compact sections the erosion is due to the imperfections, while for thin-walled members, supplementary erosion is induced by the phenomenon of coupled instabilities [70, 71], that represent a characteristic of thin-walled steel members in compression or bending. This erosion, as remarked by Gioncu [72], enables to classify the interaction types, which range from weak class to very strong class interaction. Obviously, an appropriate framing of each type of coupled instability into the relevant class is very important because the methods of analysis used for design have to be different from one class to another. In case of weak or moderate interaction, structural reliability will be provided by simply using safety coefficients, while

in case of strong or very strong interaction, special methods are needed. In [73] Dubina summarized the main coupled instability case which may appear within the bar members. Then, based on the concept of Erosion of Critical Bifurcation Load (ECBL), Dubina proposed an approach to evaluate the ultimate strength in local/distortional-global interactive buckling. This approach enables to use the Ayrton-Perry format of European buckling curves [64, 72–74] to calibrate appropriate buckling curves for any kind of interactive local/distortional-global buckling. In the spirit of [75], in the sixth chapter of the thesis, the GBT is used to find the interaction points of buckling modes and, based on that, to evaluate the erosion coefficient and propose a modified version of the ECBL approach. In particular, some pallet rack uprights in compression are analysed. The analysis consists in two steps. In the first step, the instability mode interaction points and their related imperfections are identified using GBT bifurcation analyses. In the second step, imperfection factors associated to the modified version of the ECBL approach are calculated in terms of the erosion coefficients computed in the first step. The buckling curves related to the modified and classic ECBL approaches are thus obtained and compared with experimental results [76, 77]. The comparison shows that the modified ECBL approach is in very good agreement with experimental results, while results from the classical ECBL approach are not always on the safe side.

# Chapter 1

## Mechanics of thin-walled members

### Abstract

In this chapter, thin-walled members like cold-formed and composite profiles, which are the main thin-walled beam products of interest of this work, are presented. A brief description of their use, history, and fabrication methods is outlined along with the peculiarities of these members. A theoretical framework is outlined, describing some of the most important analysis tools for the modelling of these members, with special attention being paid to beam models. The finite strip method is also briefly presented as a numerical option commonly used in this kind of analysis.

### 1.1 Cold-formed members

During the 20th century and early 21st century the progress of structural engineering has led to an increased use of structural elements characterized by a lower strength/weight ratio. Thin walled cold-formed members play an important role in this framework.

The improvement of the production technologies, the increasing of the materials strength and the development of specific design codes are the actors that are driving the development of these elements. Previously, the use of cold-formed members was confined in well delimited industrial contexts where the weight savings was the most relevant research way, such as in aeronautical, rail and automotive industries. Currently these elements are used in civil engineering and can be produced in steel or aluminum.

Winter [78], was one of the first pioneers in the study of the cold-formed members. Through a systematic research he pointed out the advantages of using the cold-forming techniques, optimizing roofing systems and leading in general to a wider use of cold-formed members in the field of industrial buildings.

Cold-formed members can be subdivided in two main categories:

- individual structural elements (monodimensional elements);
- panels and decks (bidimensional elements).

With reference to the first category, Fig. 1.1 shows some cold-formed cross-sections typically used in frame structures. The most common shapes are C-sections, Z-sections, angles, I sections, T and tubular sections. Usually the cold-formed section heights vary from 50 to 300mm, and the thicknesses between 1.0 and 7.0mm. In some cases, the height can reach 500mm and thickness 15mm. These sections are widely used as secondary structural elements for buildings

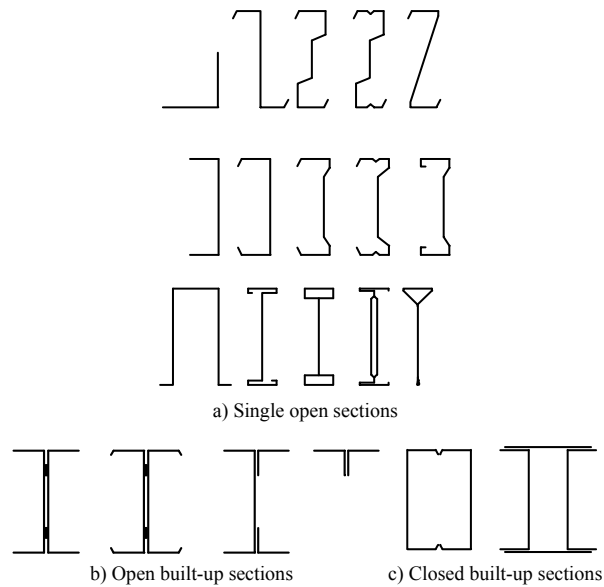


Figure 1.1: Most common cold-formed cross-sections [79].

like purlins and girts for roofing and lateral walls (Fig. 1.2) and also as primary structural elements (Fig. 1.3). The second main



Figure 1.2: Z and C sections used as: a) purlins; b) girts.

category includes all cold-formed applications about the building envelope, for example like roofing panels (Fig. 1.4). The height of these elements ranges between 35 to 200mm with thickness ranging between 0.5 to 2mm. Also in this case there is large variety of section typologies (Fig. 1.5) with very interesting applications in



Figure 1.3: Cold-formed sections used as primary structural elements.

decking solutions like composite concrete steel structures, Fig. 1.6.

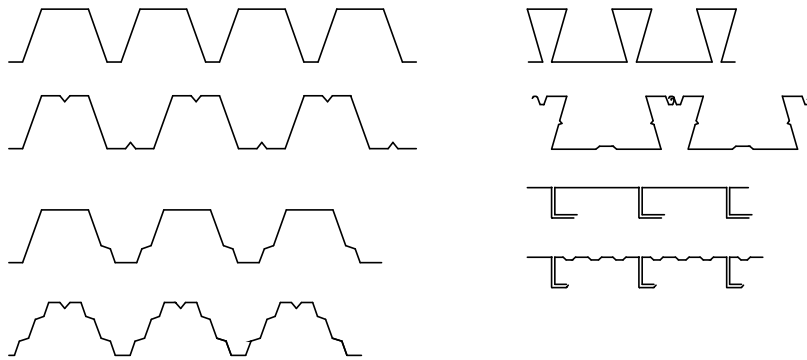


Figure 1.4: Profiled sheets and linear trays [79].



Figure 1.5: Cold-formed roofing panels.

## Manufacturing

Cold-formed members are produced starting from coated or uncoated hot-rolled or cold-rolled flat strips or coils. The sectional

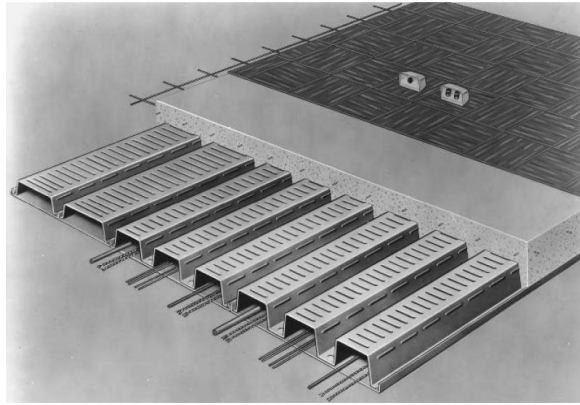


Figure 1.6: Composite concrete steel structure.

shape is obtained by two processing methods:

- roll forming;
- folding and press braking.

The process of cold-rolling, shown in Fig. 1.7-1.8. The final cross-section is obtained from a planar metal sheet by a folding operation using a series of rotating rolls placed along an production line. The number of rollers depends on the complexity of the sectional shape, the thickness and the strength of the sheet. Usually these production lines are equipped with a cutting machine that "cuts" the element to the required length and a welder, useful to weld the opposing edges of the strip before final rolling into a closed shape. In case of simple cross-section shapes and limited number of required elements it is convenient to use the hydraulic bending process (Fig. 1.9) or press braking (Fig. 1.10). The machines useful to apply these methods are composed by a mobile part and a fixed one. On the fixed part it is possible to apply the molds with the desired shapes.

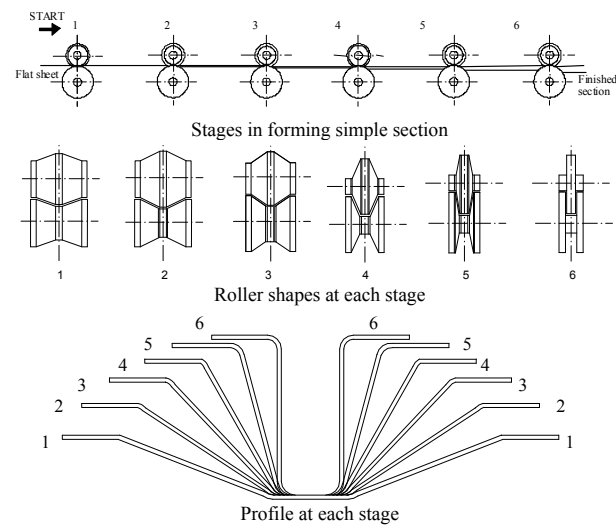


Figure 1.7: Stages in roll forming a single section [80].

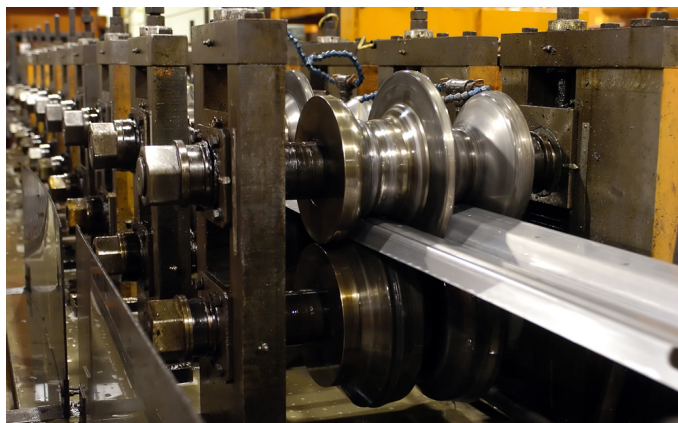


Figure 1.8: Industrial roll forming lines.

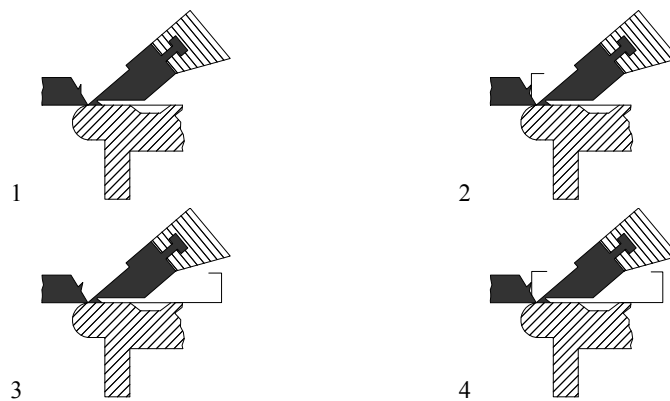


Figure 1.9: Forming of folding [79].

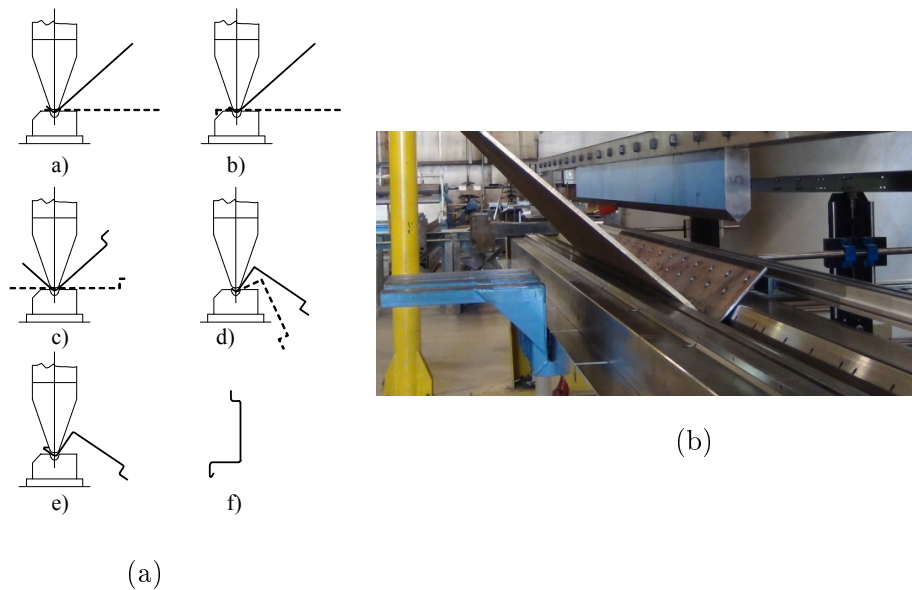


Figure 1.10: Press braking process: a) Forming steps [79]; b) Industrial brake press.

## Residual stresses

The varying stretching forces acting in the manufacturing processes of cold-formed steel section induce a particular characteristic in the final product, the residual stresses. These processes cause a changing of the strain-stress curve of the steel. In particular there is an increase of yield strength and sometimes also an increase of the ultimate strength in the corners composing the cross-section. The increase of yield strength is due to strain hardening and depends on the type of steel. The increase of ultimate strength is related to strain aging with a decrease of ductility. The residual stresses of cold-formed profiles are mainly of flexural type with respect to hot-rolled ones where the residual stresses, due to hot-rolling manufacturing processes, are mainly of membranal type. This behaviour is shown in Fig. 1.11. It is important to consider the influence

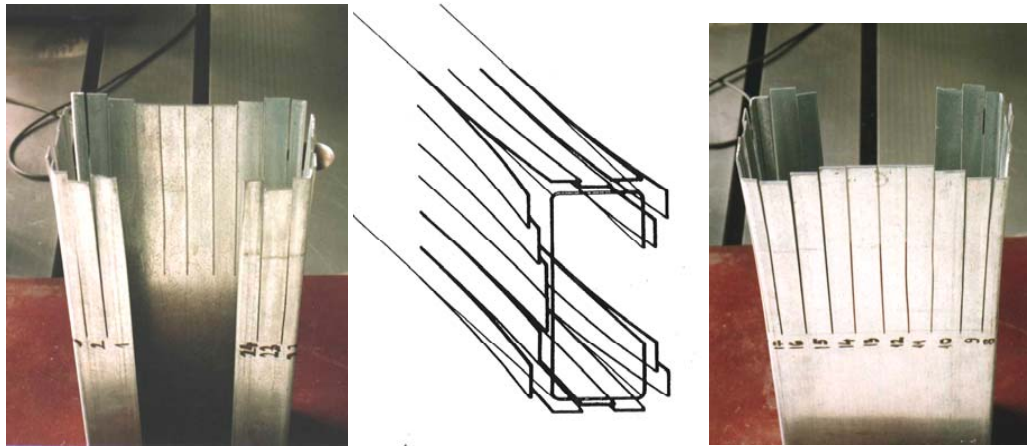


Figure 1.11: Evidence of flexural residual stresses in a lipped channel cold-formed steel section [81].

of residual stresses specially when a nonlinear analysis has to be performed.

## 1.2 Composite members

Since the early dawn of civilization the research of more resistant and lighter materials has always fascinated mankind. The use of composite materials fully answers to this request. A structural composite is a material system consisting of two or more phases on a macroscopic scale, whose mechanical performance and properties are designed to be superior to those of the constituent materials acting independently. The constituent materials of a composite are the reinforcement, usually discontinuous, stiff and strong and a matrix, weaker than the reinforcement and continuous. It is important to underline the historical milestones related to the development of these materials. A big improvement in composite materials is addressed

to the time of World War II, when fiberglass polymer matrix composites started to be used and studied. It had large applications in the 1950s with missiles and, after the invention of high-strength carbon fibers in the 1960s, the composite materials were used to build aircraft components from 1968. Starting in the late 1970s, after the development of Kevlar (or aramid) fibers (Dupont) in 1973, the application of composites expanded widely to the marine, automotive and biomedical industries. The 1990s, thanks to composite materials price dropping, marked a big expansion also in civil engineering (Fig. 1.12) with a large application in pedestrian bridges (Fig. 1.13a) and specific infrastructural buildings (Fig. 1.13b).

## **Manufacturing**

The manufacturing process is one of the most important steps in the application of composite materials. The manufacturing method has to be selected in conjunction with the material selection and structural design in a unified process. From this unified process depends the properties of the final product. A large number of fabrication methods are in use today like autoclave, vacuum bag and compression molding, filament winding, fiber placement, injection molding, pultrusion and resin transfer molding (RTM). Some of them are briefly explained in the following.



(a)



(b)

Figure 1.12: Examples of composite beams ([www.dragonplate.com](http://www.dragonplate.com)).



(a)



(b)

Figure 1.13: a) FRP pedestrian bridge in Lleida, Spain; b) Aerofoil-powered generator (Hans Hillewaert).

### Autoclave molding

The autoclave molding process is used for fabrication of high-performance composites like in military, aerospace and infrastructure applications. This process use the material in "prepreg" form (Fig. 1.14) where the matrix and the reinforcement are combined in a layer of parallel or woven fibers preimpregnated with resin. The material

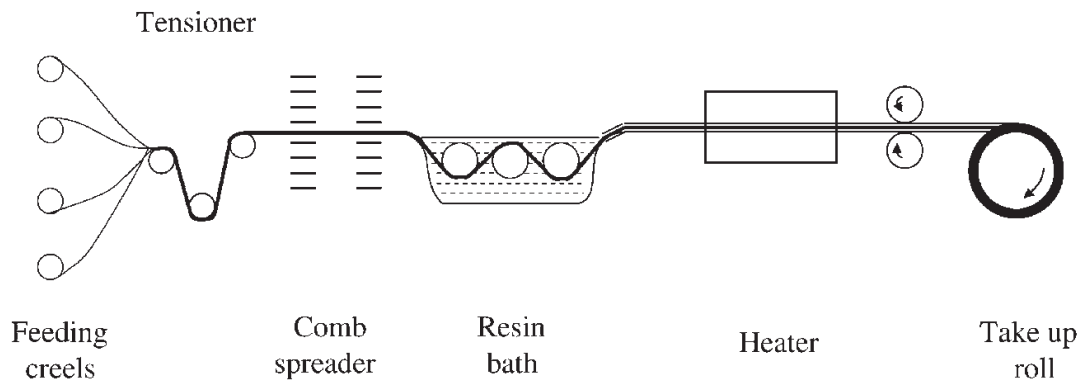


Figure 1.14: Schematic of prepregging machine.

in prepreg form is cutted, oriented as desired and stacked to form a layup. The final layer goes in a vacuum bag (Fig. 1.15) which is placed into an autoclave (Fig. 1.16) where the materials (usually thermoset ones) require temperature and pressure on the order of  $175^{\circ}C$  and  $600kPa$ . The main advantage of this process is the ability to process a large variety of materials with an excellent dimensional stability of finished product but limiting the production to well defined maximum dimensions.

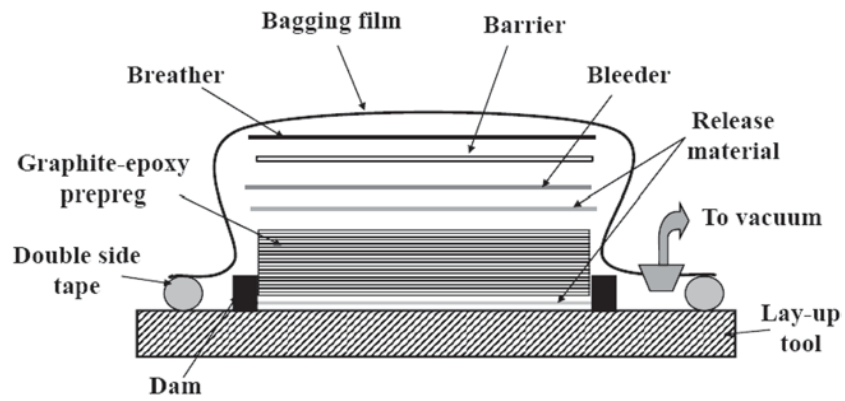


Figure 1.15: Assembly of prepreg bagged composite.

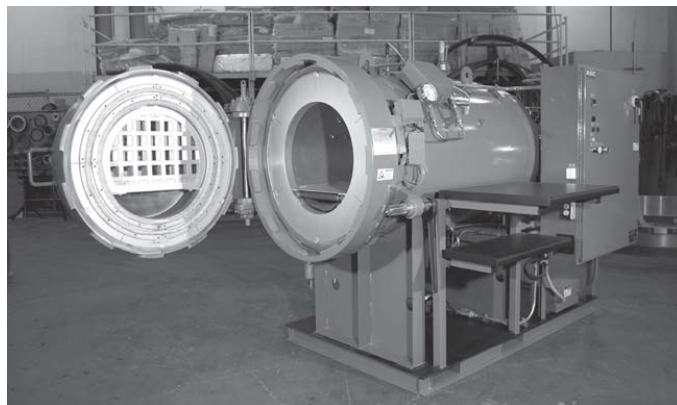


Figure 1.16: Aerospace autoclave.

### Filament winding

Filament winding process is usually applied to make composite pressure vessels, storage tanks, pipes. It ensures excellent strength-to-weight ratio and consists in winding a preimpregnated or resin coated (under tension) reinforcement around a rotating mandrel (Fig. 1.17). It can be applied only on products having surfaces revolutions. This process guarantees a good uniformity of resin distribution in finished parts.

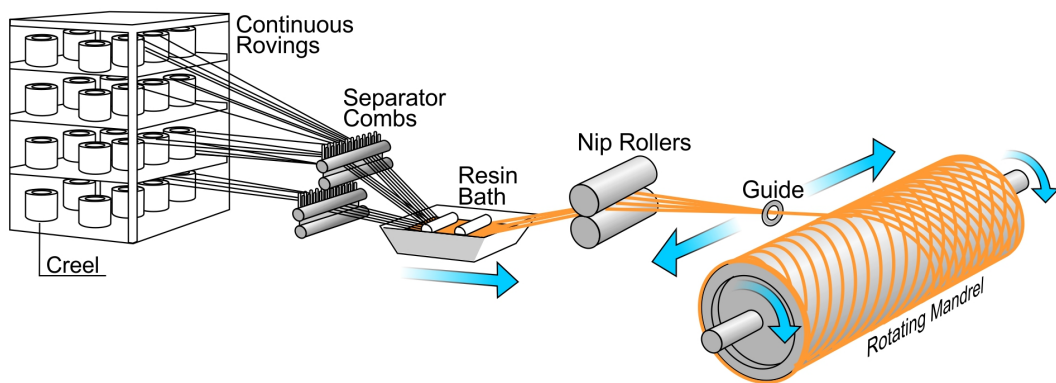


Figure 1.17: Schematic of filament winding process ([www.nuplex.com](http://www.nuplex.com)).

### Pultrusion

Fig. 1.18 shows a representation of the four steps required in a pultrusion process. In this process the fibers are routed through a series of guides (step 1) and impregnated with a thermosetting resin (step 2). Then the fibers are pulled through a heated die (step 3) where the resin flows and wets the fibers. The resin, in this step, cures and the fiber/resin system became solid. Finally the composite is pulled by a puller and cutted (step 4). The pultrusion

process does not provide flexibility (only simple shapes production) and uniformity of product control and automation but ensures high output.

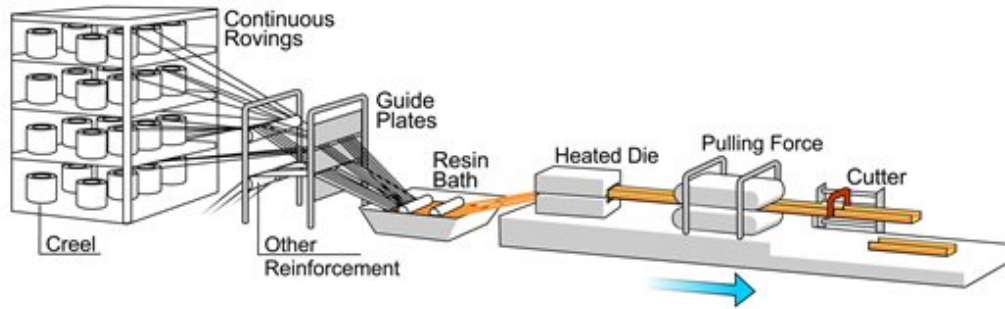


Figure 1.18: Schematic of pultrusion process ([www.nuplex.com](http://www.nuplex.com)).

### 1.3 Modeling framework

When the torsional rigidity of a beam is very small, as happens in thin-walled open cross-sections, buckling may take place with a rotation of the cross-section around a longitudinal axis and it may be accompanied by deflection in one or both the principal planes of inertia. These kind of instabilities appear for load values which are much below the lower of the two Eulerian critical loads and are known as torsional instability and flexural-torsional instability. In this cases it is important to handle the problem with a beam model able to catch the torsional behavior. The model of Vlasov [1] in the 1940s, also known as the Theory of the Sectorial Area, is characterized by a kinematics that comprises a warping function that describes the non-uniform torsion along the beam axis. Vlasov theory has been enriched by the efforts of many authors. Timoshenko and

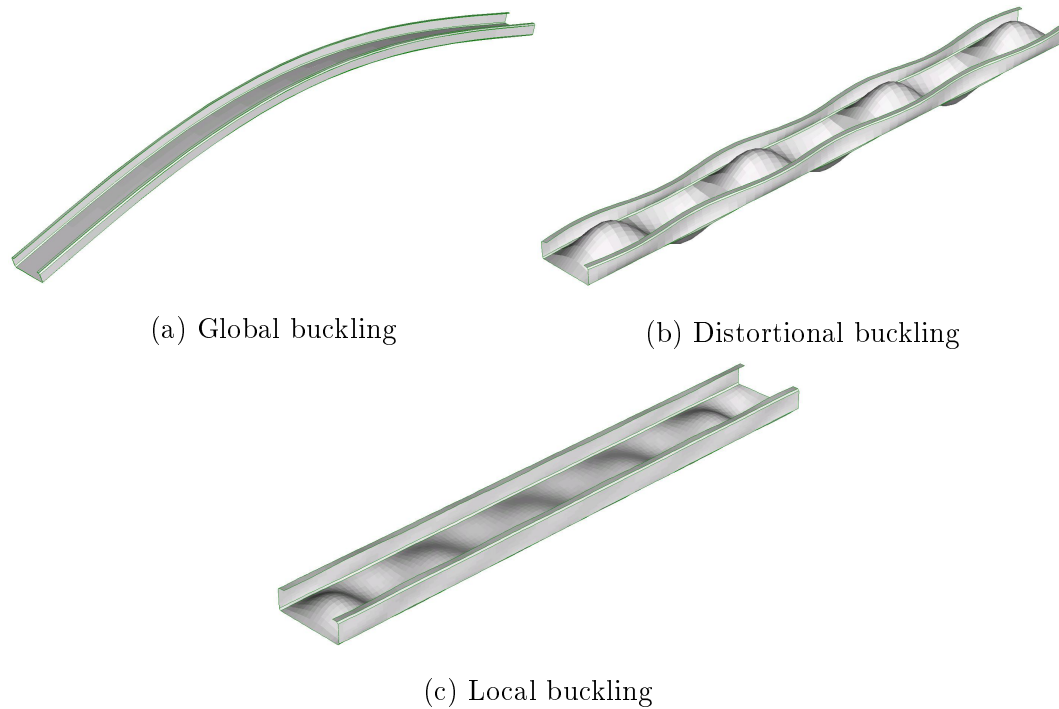


Figure 1.19: Buckling modes

Gere [82] described the stability of thin-walled beams under different loading conditions. Murray [83] applied the theory to standard design practices and Wilson et al. [4] and Kim et al. [3] worked on the stability of thin-walled profiles. However, despite the importance of the Vlasov theory, it has some limitations: the cross-section is considered to be perfectly rigid in its own plane, the shear strains in the middle surface of the wall are neglected, and the transverse normal stresses in the walls are ignored along with normal stresses tangent to the midsurface of the wall. These limitations may lead to an incomplete mechanical description of thin-walled beams that can be the reason of a not correct prediction of the thin-walled beams behavior. In fact, thin-walled beams are essentially folded plates and, above the flexural and torsional behaviors, can be sub-

jected to cross-sectional in-plane deformations like distortions and local effects along with richer out-of-plane deformations (see Fig. 1.19) and all these kinematic phenomena can appear in a coupled manner. Some interesting beam models, already introduced, overcome the limits of Vlasov theory. In particular, the Capurso beam theory, Garcea's generalized beam model and CUF, due to their particular characteristics, deserve to be mentioned and briefly described. Of course the Generalized Beam Theory belongs in this set and will be extensively exposed in the next chapter.

### **Capurso beam theory**

The Capurso Beam Theory, introduced by Michele Capurso in the 1960s [6], consists in a generalization of the cross-section's degree of freedom concept. Capurso, starting from the Vlasov beam theory, added a series of warping functions over the cross-section describing all the possible shapes in which the cross-section could warp and maintaining the six classical degree of freedom of a Vlasov beam: axial displacement, displacements and rotations over the two main axes of inertia and non-uniform torsion. This description also eliminates the assumption of null shear strains in the middle surface of the wall. The Capurso beam is one of the first instances of a modal description of the mechanics of thin-walled beams over the theory of Vlasov. In fact, since each new warping function added to the kinematic description is weighed depending on the beam loading, the Capurso beam theory can be defined as a modal theory. The

model of Capurso remains valid today and it has been extended to transversely isotropic materials and applied to the analysis of pultruded fiber-reinforced polymer (FRP) thin-walled beams [84][11]. However this theory lacks in considering the cross-section distortion, not allowing the description of in-plane deformations of the cross-section and local phenomena. This kinematic constraint limits its application to beams with distributed shear diaphragms but with a free to warp sections.

### **Garcea's generalized beam model**

Garcea and his co-workers developed a beam model [85], [17], [18], [86] obtained by splitting the 3D elasticity problem into a 2D discrete cross-section analysis (Generalized Eigenvectors method), see Fig. 1.20, and a variable parametrization along the beam axis. It is achieved using a semi-analytical formulation. This formulation leads to a set of differential equations along the beam and is characterized by a group of generalized eigenvectors associated to null eigenvalues, extending the classical de Saint Venant solution to generic anisotropic beams. This kind of model can also include high-order deformation modes, obtained as end-tip effects. The finite element is obtained by considering a mixed, stress and displacement, Hellinger-Reissner variational formulation, together with the implicit co-rotational method in order to handle large displacements and finite rotations [87], [88]. Recently, Garcea also proposed a simplified version of the model, using a compatible dis-

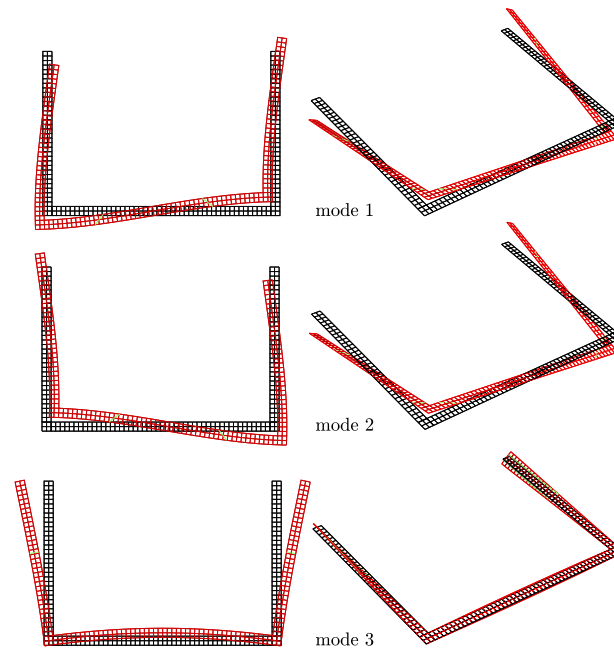


Figure 1.20: C-section: first 3 additional modes [17].

placement description, in order to compare the generalized beam model with the GBT [33]. The cross-section analysis is performed without simplifying assumptions such as plane stress and kirchhoff hypothesis. Consequently it is applicable to both thin-walled and thick-walled sections and it gives the possibility to handle problems where the 3D stresses are relevant. In this model the cross-section analysis returns naturally hierarchic modes but lacks in strain criteria useful to discard specific components. It could be useful to avoid locking problems and perform targeted analyses.

### **CUF: Carrera Unified Formulation**

The CUF, proposed by Carrera [16], provides one-dimensional (beam) and also two-dimensional (plate and shell) high-order structural models. About the beam model, called CUF 1D, the displacement

fields are expressed over the cross-section in terms of basis functions whose forms and orders are arbitrary. CUF 1D reproduces results that are usually provided by 3D elements, and can be subdivided in two model classes: the Taylor-Expansion class (TE) and the Lagrange-Expansion class (LE). TE class exploit  $N$ -order Taylor-like polynomials to define the displacement field above the cross-section with  $N$  as a free parameter of the formulation. It can be defined as a one-dimensional model with  $N$ th-order displacement field. LE class is based on Lagrange-like polynomials to discretize the cross-section displacement field, having only pure displacement variables. It can be defined as a one-dimensional model with a surface-based geometry and pure displacement variable. Fig. 1.21 and 1.22 summarize the TE and LE modelling approach. Both

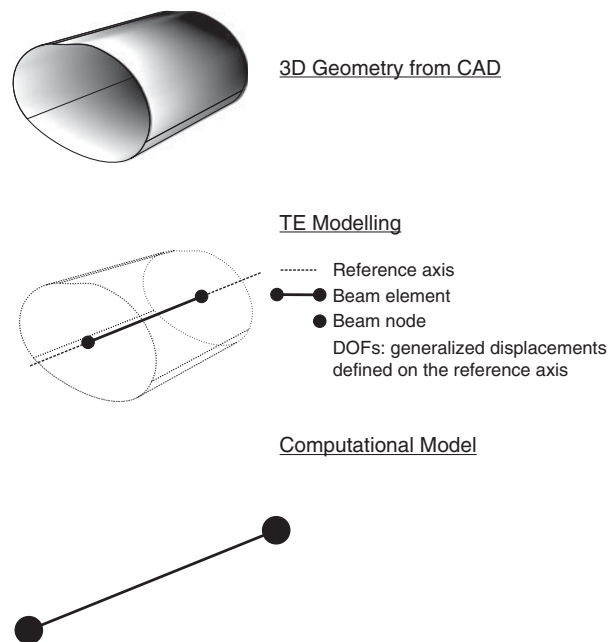


Figure 1.21: TE modelling approach [16].

model classes account for warping and distortional phenomena, de-

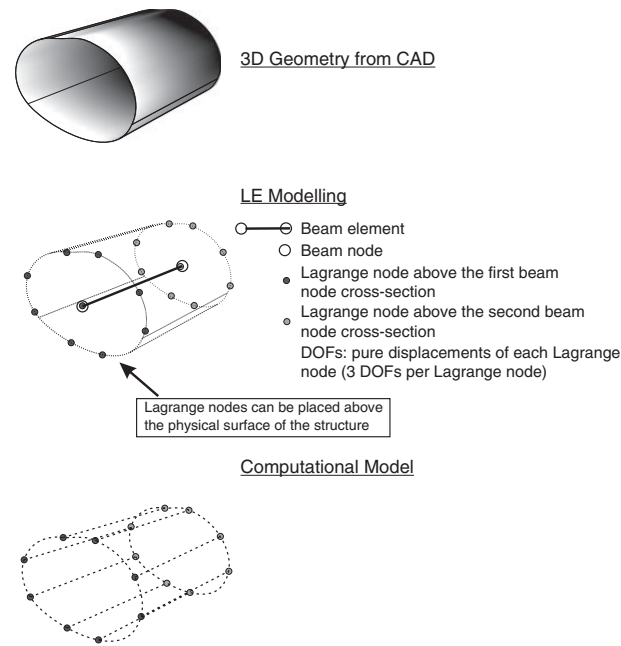


Figure 1.22: LE modelling approach [16].

tecting 3D-like results with low computational cost. Depending on the application, TE class or LE class model can be properly used [89], [90]. However in CUF a modal decomposition, able to select and classify specific mechanical behaviours, is not provided. Moreover in LE class model, although these elements can deal directly with the 3D geometry given by a CAD model, it is not possible to apply "classical" beam boundary conditions, showing a solid-like geometrical setting.

### The Finite Strip Method

The FEM is the most powerful and versatile tool to evaluate the solutions in structural analysis. However in many cases, where the geometry and the boundary conditions are regular (like in most cases related to the thin-walled beams), the accurate results com-

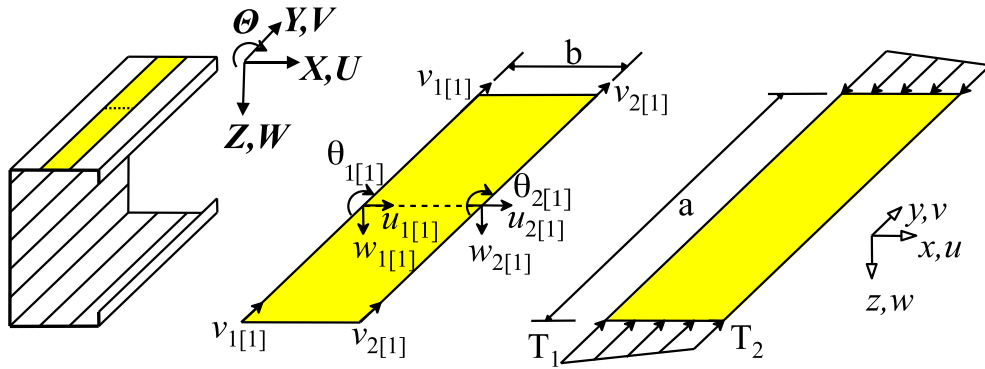


Figure 1.23: Finite strip discretization, strip DOFs.

ing from a full finite element analysis have a high computational cost. In this field, the Finite Strip Method (FSM) [91] is an alternative method useful to reduce the computational effort ensuring accurate results in case of regular geometry and regular boundary conditions, taking into account not only the enriched warping description present in the Capurso theory but also the distortion of the cross-section and local effects. FSM is a semi-analytical procedure that stands in between the classical Rayleigh-Ritz method and a FEM solution. It uses a separation of variables, in a similar way to that of Kantorovich [92], between the axial and cross-sectional directions. The beam is divided in strips, adjacent among themselves (Fig. 1.23), characterized by (i) a set of displacement functions acting in the direction parallel to the beam axis and (ii) a set of displacement functions over the cross-section. In the more recent versions of FSM, spline functions are used as displacement functions. This sort of discretization leads to a solving system of equations characterized by less unknowns than a FEM approach.

Since each strip is considered to be under a plane stress state and based on the Kirchhoff thin plate theory, the FSM allows to take into account not only the enriched warping description present in the Capurso theory, but also the distortion of the cross-section and local effects. However, the family of solutions obtained is difficult to classify into meaningful modes, so most current applications of the FSM introduce specific mechanical criteria to separate the displacement field into distinct subspaces. These mechanical criteria, directly motivated by the GBT [31], form the basis of the so-called Constrained Finite Strip Method (cFSM) that allows to separate the displacement field into distinct subspaces, allowing to differentiate global, distortional and local behaviors. The cFSM has been successfully used by Shafer to analyze cold-formed steel members [19]. However, some cons should be highlighted like (i) the impossibility to impose boundary conditions over the member and (ii), despite the use of specific mechanical criteria (cFSM), the modes coming from the analysis haven't a clear mechanical meaning, leading to an incorrect stress recovery.

## Chapter 2

# The shear deformable Generalized Beam Theory

### Abstract

In this chapter, an overview of the evolution of the shear deformable Generalized Beam Theory (GBT) is presented. The starting point is the original GBT formulation proposed by Shardt. This formulation, assuming Vlasov's hypothesis, neglects shear deformability along the midline of the cross-section. Camotim and Silvestre, in order to remove Vlasov's hypothesis, proposed a revised version of GBT kinematics introducing shear deformability in a similar way as in the theory of Capurso. Anyway this solution didn't solve the problem of a non-perfect coherence between bending and shear strain components. A new GBT formulation proposed by de Miranda et al. [46, 47] solved the problem allowing to establish a clear relationship between the results of the GBT and those of the classical beam theories. This improved kinematics is extensively discussed in this chapter and used in the following of the thesis.

This chapter is organized as follows. After a brief overview of

the original GBT formulation proposed by Schardt [20, 21] and of the revised version of Camotim and Silvestre [44, 45] given in Section 2.1, the kinematics of the new GBT formulation proposed in [47] is presented in Section 2.2 and the complete formulation of the GBT for the flexural deformation modes in Section 2.3. Finally, the new GBT formulation for nonlinear warping modes is presented in Section 2.4.

## **2.1 Shear deformable Generalized Beam Theory: from the original formulation to the last developments**

The GBT is a beam theory with enriched kinematics where the hypothesis of rigid cross-section is removed, allowing cross-section in-plane distortions. This theory was proposed by Shardt in 1980s [20, 21].

The GBT can be viewed as a one-dimensional theory deduced from a parent three-dimensional theory basing on some kinematical ansatzs. In particular, the displacement field of the beam is assumed as a linear combination of predefined cross-section deformation modes multiplied by generalized displacements that depend on the beam axial coordinate. In the original GBT [20, 21], the following displacement field is assumed for the generic  $i$ -th wall of the

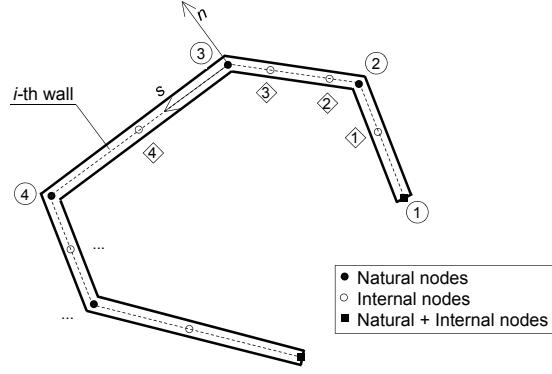


Figure 2.1: Thin-walled cross-section.

cross-section (see Fig. 2.1):

$$d_n(n, s, z, t) = \boldsymbol{\psi}(s)\mathbf{v}(z, t), \quad (2.1)$$

$$d_s(n, s, z, t) = [\boldsymbol{\mu}(s) - n\partial_s\boldsymbol{\psi}(s)]\mathbf{v}(z, t), \quad (2.2)$$

$$d_z(n, s, z, t) = [\boldsymbol{\varphi}(s) - n\boldsymbol{\psi}(s)]\partial_z\mathbf{v}(z, t), \quad (2.3)$$

where  $d_n$  is the displacement orthogonal to the wall midline,  $d_s$  is the displacement tangent to the wall midline,  $d_z$  is the displacement in the beam axial direction,  $\boldsymbol{\psi}$ ,  $\boldsymbol{\mu}$  and  $\boldsymbol{\varphi}$  are row matrices collecting the assumed cross-section deformation modes (depending only on  $s$  and  $n$ ), and  $\mathbf{v}$  is a vector that collect the unknown kinematic parameters (depending only on abscissa  $z$  and time  $t$ ). Moreover,  $\partial_s$  and  $\partial_z$  denote the derivative with respect to the  $s$  coordinate and to the  $z$  coordinate, respectively. In the following, the term *natural nodes* is used to refer to the vertices of the cross-section midline, while *internal nodes* to intermediate points along the wall midline, as shown in Fig. 2.1. The original GBT formulation engender null shear strain  $\gamma_{zs}$  according with the theory of Vlasov.

Silvestre and Camotim [44, 45] were the first to account for shear

deformation by removing the Vlasov constraint. To this purpose, they added further modes  $\boldsymbol{\varphi}_s$ , called *shear modes*, that involve non-null warping together with null in-plane displacement. This leads to the following kinematics [48, 93–95]:

$$d_n(n, s, z, t) = \boldsymbol{\psi}(s)\mathbf{v}(z, t), \quad (2.4)$$

$$d_s(n, s, z, t) = [\boldsymbol{\mu}(s) - n\partial_s\boldsymbol{\psi}(s)] \mathbf{v}(z, t), \quad (2.5)$$

$$d_z(n, s, z, t) = [\boldsymbol{\varphi}(s) - n\boldsymbol{\psi}(s)] \partial_z\mathbf{v}(z, t) + \boldsymbol{\varphi}_s(s)\boldsymbol{\delta}(z, t), \quad (2.6)$$

where a term is added in the expression of the warping displacement  $d_z$ . It is worth to note that modes  $\boldsymbol{\varphi}_s$  introduce non-linear variation of the warping displacement along the wall midline, but assume constant warping displacement along the wall thickness. These modes are formally analogous to those proposed by Capurso [6, 7]. Adding  $\boldsymbol{\varphi}_s$  shear modes results in relaxing the Vlasov constraint of null shear strain  $\gamma_{zs}$  along the midline of the cross-section. Anyway, due to the constant warping displacement along the wall thickness, they lead to null shear strain  $\gamma_{zn}$  between the direction of the beam axis and that orthogonal to the wall midline. This engender a non-perfect coherence between the bending and shear strain components of the beam. Fig. 2.2 shows that, due to the null  $\gamma_{zn}$ , the shear component in the classical shear deformable GBT exhibits a mismatch through the wall thickness with the bending strain component of the beam. This implies to use an ad hoc modal decomposition procedure for shear modes, different from the flexural one and classical shear deformable beam theories are not recov-

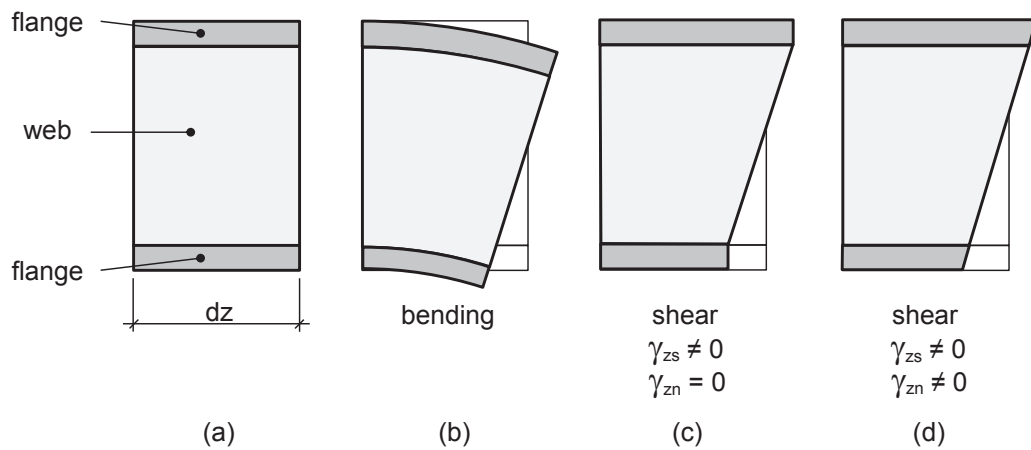


Figure 2.2: Sketch of the main difference between classical shear deformable GBT and the present formulation: (a) undeformed elementary beam, (b) bending strain component, (c) corresponding shear strain component in the classical GBT, (d) corresponding shear strain component in the Timoshenko beam theory and in the present theory.

ered exactly. Due to the lack of cross-section rotations as degrees of freedom it is not possible to readily apply corotational approaches [87, 88, 96], limiting the developing of geometrically nonlinear formulations.

Recently, de Miranda et al. [46] proposed a revised Generalized Beam Theory kinematics correctly accounting for shear deformation. In particular it introduces the variability of the warping displacement along the wall thickness besides that along the wall midline engendering non-null shear strains  $\gamma_{zn}$  and  $\gamma_{zs}$ . This formulation guarantees that the bending and the shear strain components of the beam match through the wall thickness too. The following expressions are assumed for the displacement field of the  $i$ -th wall

(Fig. 2.1):

$$d_n(n, s, z, t) = \boldsymbol{\psi}(s)\mathbf{v}(z, t), \quad (2.7)$$

$$d_s(n, s, z, t) = [\boldsymbol{\mu}(s) - n\partial_s\boldsymbol{\psi}(s)]\mathbf{v}(z, t), \quad (2.8)$$

$$d_z(n, s, z, t) = [\boldsymbol{\varphi}(s) - n\boldsymbol{\psi}(s)][\partial_z\mathbf{v}(z, t) + \boldsymbol{\delta}(z, t)] + \boldsymbol{\varphi}^h(s)\boldsymbol{\delta}^h(z, t). \quad (2.9)$$

Shear deformation is introduced by two types of shear modes: *basic shear modes* and *additional shear modes*. Basic shear modes, related to  $\boldsymbol{\delta}$  kinematic parameters, are in the same number of flexural ones. The classical shear strain components of the Timoshenko beam theory are recovered: the cross-section out-of-plane rotation does not coincide anymore with the derivative of the transverse displacement. The additional shear modes, related to  $\boldsymbol{\delta}^h$  kinematic parameters, are not essential to run a GBT analysis but can be introduced to further enrich the sole warping description along the wall direction. These additional shear modes coincide with those originally introduced by Silvestre and Camotim. It is worth to note that a reviewed form of the cross-section analysis procedure is devised for this kinematics [46]. It is based on a unique modal decomposition for flexural and shear modes. It is then possible to clearly separate the single flexural and shear contributions and to recover classical beam degrees of freedom and, as special cases, the standard beam theories.

In order to allow to establish a clear relationship between the GBT results and those of the classical beam theories, the GBT presented by de Miranda et al. [46] is reformulated by introducing different

definitions of the kinematic parameters and of the generalized deformations as proposed in [47]. This new formulation, more attractive for current engineering applications, is presented in the next Section and it will be used as basis for the following developments.

## 2.2 Shear deformable Generalized Beam Theory: kinematics

The following displacement field is assumed for the generic  $i$ -th wall of the cross-section (Fig. 2.1):

$$d_n(s, z, t) = \boldsymbol{\psi}(s)\mathbf{v}(z, t), \quad (2.10)$$

$$d_s(n, s, z, t) = \boldsymbol{\xi}(s, n)\mathbf{v}(z, t), \quad (2.11)$$

$$d_z(n, s, z, t) = \boldsymbol{\omega}(s, n)\mathbf{w}(z, t), \quad (2.12)$$

where  $\boldsymbol{\psi}$ ,  $\boldsymbol{\xi}$  and  $\boldsymbol{\omega}$  are row matrices collecting the assumed cross-section deformation modes (depending only on  $s$  and  $n$ ), and  $\mathbf{v}$  and  $\mathbf{w}$  are vectors that collect the unknown kinematic parameters (depending only on  $z$  and  $t$ ). In accordance with the hypothesis that the generic wall behaves as a Kirchhoff plate, cross-section deformation modes  $\boldsymbol{\xi}$  and  $\boldsymbol{\omega}$  are assumed to depend linearly on  $n$  in the form:

$$\boldsymbol{\xi}(n, s) = \boldsymbol{\mu}(s) - n\partial_s\boldsymbol{\psi}(s), \quad \boldsymbol{\omega}(n, s) = \boldsymbol{\varphi}(s) - n\boldsymbol{\psi}(s), \quad (2.13)$$

where  $\boldsymbol{\mu}$  and  $\boldsymbol{\varphi}$  are predefined shape functions. It can be easily verified that, by a suitable redefinition of the generalized displacements  $\mathbf{w}$ , the above kinematics coincides with that reported in (2.7)-(2.9)

(in absence of additional shear modes  $\varphi^h$ ) and proposed in [46]. Equations (2.10)-(2.12) can be recast in the following matrix form:

$$\mathbf{d}(n, s, z, t) = \mathbf{U}(s, n)\mathbf{u}(z, t), \quad (2.14)$$

where:

$$\mathbf{d} = \begin{bmatrix} d_n \\ d_s \\ d_z \end{bmatrix}, \quad \mathbf{U} = \begin{bmatrix} \boldsymbol{\psi} & \mathbf{0} \\ \boldsymbol{\xi} & \mathbf{0} \\ \mathbf{0} & \boldsymbol{\omega} \end{bmatrix}, \quad \mathbf{u} = \begin{bmatrix} \mathbf{v} \\ \mathbf{w} \end{bmatrix}. \quad (2.15)$$

Strains can be computed from Eqs. (2.10)-(2.13) by means of the three-dimensional compatibility equations yielding  $\varepsilon_{nn} = 0$ ,  $\gamma_{sn} = 0$  and:

$$\boldsymbol{\varepsilon}(n, s, z, t) = \mathbf{E}(s, n)\mathbf{e}(z, t), \quad (2.16)$$

where

$$\boldsymbol{\varepsilon} = \begin{bmatrix} \varepsilon_{ss} \\ \varepsilon_{zz} \\ \gamma_{zs} \\ \gamma_{zn} \end{bmatrix}, \quad (2.17)$$

$$\mathbf{E} = \begin{bmatrix} \partial_s \boldsymbol{\xi} & \mathbf{0} & \mathbf{0} & \mathbf{0} \\ \mathbf{0} & \boldsymbol{\omega} & \mathbf{0} & \mathbf{0} \\ \mathbf{0} & \mathbf{0} & -2n\partial_s \boldsymbol{\psi} + \partial_s \boldsymbol{\varphi} + \boldsymbol{\mu} & \frac{1}{2}(\boldsymbol{\mu} - \partial_s \boldsymbol{\varphi}) \\ \mathbf{0} & \mathbf{0} & \mathbf{0} & \boldsymbol{\psi} \end{bmatrix}, \quad (2.18)$$

and  $\mathbf{e}$  is the vector collecting the independent  $z$ -fields governing the strain components, hereinafter denoted as generalized deformation parameters:

$$\mathbf{e}^T = \left[ \boldsymbol{\alpha}^T \quad \boldsymbol{\chi}^T \quad \boldsymbol{\beta}^T \quad \boldsymbol{\gamma}^T \right], \quad (2.19)$$

$$\boldsymbol{\alpha} = \mathbf{v}, \quad \boldsymbol{\chi} = \partial_z \mathbf{w}, \quad \boldsymbol{\beta} = \frac{1}{2}(\partial_z \mathbf{v} + \mathbf{w}), \quad \boldsymbol{\gamma} = \partial_z \mathbf{v} - \mathbf{w}. \quad (2.20)$$

As it can be noted, the strains components comprise terms not depending on  $n$  and terms proportional to  $n$ . In the following, the former will be called "membrane" part of the strain and denoted by  $\boldsymbol{\lambda}$ , and the latter will be called "bending" part and denoted by  $\boldsymbol{\chi}$ . Finally, combining Eqs. (2.19) and (2.20) leads to the following generalized displacement-deformation relationship:

$$\mathbf{e} = \mathbf{D}\mathbf{u}, \quad (2.21)$$

$$\mathbf{u} = \begin{bmatrix} \mathbf{v} \\ \mathbf{w} \end{bmatrix}, \quad \mathbf{D} = \mathbf{I}_m \otimes \mathcal{L}, \quad \mathcal{L} = \begin{bmatrix} 1 & 0 \\ 0 & \partial_z \\ \frac{1}{2}\partial_z & \frac{1}{2} \\ \partial_z & -1 \end{bmatrix},$$

where  $\mathbf{I}_m$  is the  $m$ -order unit matrix being  $m$  the number of the deformation modes, and symbol  $\otimes$  denotes the Kronecker product. According to Eq. (2.21), the differential operator  $\mathbf{D}$  can be interpreted as the compatibility operator of the beam model. Indeed, it is worth to note that parameters  $\mathbf{e}$  are not free from cross-section rigid-body motions. Even if similar, the above kinematics differs from that presented in [46] for some specific aspects that it is worth to remark here. The most evident difference lies in the different choice of the kinematic parameters. In particular, in the present formulation they do not include any derivatives, while in [46], as well as in the classical GBT,  $\partial_z \mathbf{v}$  is included between the kinematic parameters. This leads to a beam compatibility opera-

tor, Eq. (2.21), involving only first-order derivatives in the axial direction and not also second-order ones like in [46] and in the classical GBT. This is somehow similar to what happens passing from the Euler-Bernoulli to the Timoshenko beam theory and, as it is well known, can have important consequences if finite element modelling, or other numerical modelling, has to be developed. Another issue regards the definition of the generalized deformation parameters given in Eq. (2.20), different form that used in [46]. This choice allows for a clear identification of the relationship between the present generalized deformations parameters and those of classical and non-classical beam theories [47]. However, notwithstanding the remarked differences, the selection of the cross-section deformation modes and the modal decomposition procedure of the present formulation follow the same path outlined in [46].

### 2.2.1 Deformation modes

In the following, the term natural nodes is used to refer to the vertices of the cross-section midline, while internal nodes to intermediate points along the wall midline, as shown in Fig. 2.1. Deformation modes are subdivided in flexural-shear modes and nonlinear warping modes. Flexural-shear modes are governed by parameters  $\mathbf{v}$  and  $\mathbf{w}$  and are subdivided into fundamental flexural-shear modes (FFS), based on natural nodes, and local flexural-shear modes (LFS), based on internal nodes. Both the fundamental and local flexural-shear modes are the same as those of the original GBT and are summa-

rized in Fig. 2.3. As it can be easily verified, fundamental flexural-

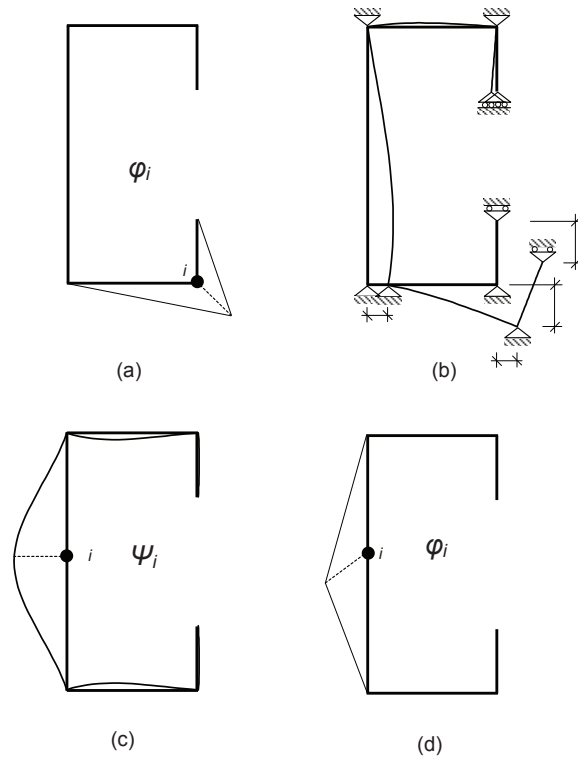


Figure 2.3: Deformation modes. (a) Out-of-plane displacement for fundamental flexural-shear: piecewise linear  $\varphi$ ; (b) in-plane displacement for fundamental flexural-shear:  $\boldsymbol{\mu} = -\partial_s \varphi$  and cubic  $\psi$ ; (c) in-plane displacement for local flexural-shear: cubic  $\psi$  (with null  $\boldsymbol{\mu}$  and  $\varphi$ ); (d) out-of-plane displacement for nonlinear warping: piecewise linear  $\varphi$  (with null  $\boldsymbol{\mu}$  and  $\psi$ ).

shear modes engender null  $\lambda_{ss}$  and  $\chi_{zn}$  and piecewise constant (i.e. constant on each wall)  $\lambda_{zs}$  along the section midline. In particular, matrix  $\mathbf{E}$  for these modes takes the following form:

$$\mathbf{E} = \begin{bmatrix} -n\partial_{ss}\psi & \mathbf{0} & \mathbf{0} & \mathbf{0} \\ \mathbf{0} & \boldsymbol{\omega} & \mathbf{0} & \mathbf{0} \\ \mathbf{0} & \mathbf{0} & -n2\partial_s\psi & -\partial_s\varphi \\ \mathbf{0} & \mathbf{0} & \mathbf{0} & \psi \end{bmatrix}. \quad (2.22)$$

Nonlinear warping modes (NLW) can be introduced to enrich the sole warping description along the wall direction. They coincide with those originally introduced by Silvestre and Camotim [44][45] and are typical of beam theories with enriched warping description such as that of Capurso [6][7]. These modes are ruled by parameters  $\mathbf{w}$  and summarized in Fig. 2.3. These modes engender  $\varepsilon_{ss} = \gamma_{zn} = 0$  and matrix  $\mathbf{E}$  takes the following form:

$$\mathbf{E} = \begin{bmatrix} \mathbf{0} & \mathbf{0} & \mathbf{0} & \mathbf{0} \\ \mathbf{0} & \varphi & \mathbf{0} & \mathbf{0} \\ \mathbf{0} & \mathbf{0} & \partial_s \varphi & -\frac{1}{2} \partial_s \varphi \\ \mathbf{0} & \mathbf{0} & \mathbf{0} & \mathbf{0} \end{bmatrix}. \quad (2.23)$$

## 2.3 Flexural formulation

In this section, the formulation of the GBT for flexural-shear modes is presented. In the following, all the expressions are given for fundamental flexural-shear modes. The corresponding expressions for local flexural-shear modes can be obtained by simply putting  $\boldsymbol{\mu} = \boldsymbol{\varphi} = \mathbf{0}$ .

### 2.3.1 Generalized stresses and forces

The generalized stresses  $\mathbf{s}$  are defined as the work-conjugates of the generalized deformations  $\mathbf{e}$  according to the following work equivalence condition:

$$\int_A \boldsymbol{\sigma}^T \boldsymbol{\varepsilon} \, dA = \mathbf{s}^T \mathbf{e}, \quad (2.24)$$

where  $\boldsymbol{\sigma} = \begin{bmatrix} \sigma_{ss} & \sigma_{zz} & \tau_{zs} & \tau_{zn} \end{bmatrix}^T$  is the vector collecting the three-dimensional stress components. Using Eq. (2.16), the above condition yields:

$$\mathbf{s} = \int_A \mathbf{E}^T \boldsymbol{\sigma} \, dA, \quad (2.25)$$

being  $A$  the area of the cross-section of the beam. As observed in the previous section, parameters  $\mathbf{e}$  are not free from cross-section rigid-body motions. Of course, the  $\mathbf{s}$  parameters corresponding to such modes are meaningless. Assuming  $\mathbf{s}^T = \begin{bmatrix} \mathbf{S}^T & \mathbf{M}^T & \mathbf{T}^T & \mathbf{V}^T \end{bmatrix}$  and substituting Eq. (2.22) in Eq. (2.25), the following expressions for the components of  $\mathbf{s}$  are obtained:

$$\mathbf{S} = - \int_A n \partial_{ss} \boldsymbol{\psi}^T \sigma_{ss} dA, \quad (2.26)$$

$$\mathbf{M} = \int_A \boldsymbol{\omega}^T \sigma_{zz} dA, \quad (2.27)$$

$$\mathbf{T} = - \int_A 2n \partial_s \boldsymbol{\psi}^T \tau_{zs} dA, \quad (2.28)$$

$$\mathbf{V} = - \int_A (\partial_s \boldsymbol{\varphi}^T \tau_{zs} + \boldsymbol{\psi}^T \tau_{zn}) dA = - \int_A \nabla \boldsymbol{\omega} \big|_{n=0} \boldsymbol{\tau}_z dA, \quad (2.29)$$

with  $\boldsymbol{\tau}_z^T = \begin{bmatrix} \tau_{zs} & \tau_{zn} \end{bmatrix}$ . In the same fashion of the generalized stresses, the generalized forces are defined as the work-conjugates of the kinematic parameters  $\mathbf{u}$ . Denoting by  $\mathbf{b}^T = \begin{bmatrix} b_n & b_s & b_z \end{bmatrix}$  the vector collecting the bulk loads applied on the  $i$ -th wall, the generalized bulk forces  $\mathbf{f}^{(b)}$  are defined as:

$$\mathbf{f}^{(b)} = \int_A \mathbf{U}^T \mathbf{b} \, dA. \quad (2.30)$$

Using Eq. (2.15), the above equation can be rewritten as:

$$\mathbf{f}_v^{(b)} = - \int_l \nabla \boldsymbol{\omega} \big|_{n=0} \cdot \mathbf{q}_{in} \, ds - \int_l \partial_s \boldsymbol{\psi}^T m_s \, ds, \quad (2.31)$$

$$\mathbf{f}_w^{(b)} = \int_l \boldsymbol{\varphi}^T q_z ds + \int_l \boldsymbol{\psi}^T m_z ds, \quad (2.32)$$

being  $\mathbf{f}^{(b)T} = \begin{bmatrix} \mathbf{f}_v^{(b)T} & \mathbf{f}_w^{(b)T} \end{bmatrix}$ ,  $l$  the cross-section midline length, and  $\mathbf{q}_{in}^T = \begin{bmatrix} q_s & q_n \end{bmatrix}$ ,  $q_z$ ,  $m_s$  and  $m_z$  the thickness resultants (see Fig. 2.4):

$$q_z = \int_h b_z dn, \quad q_s = \int_h b_s dn, \quad q_n = \int_h b_n dn, \quad (2.33)$$

$$m_z = - \int_h n b_z dn, \quad m_s = \int_h n b_s dn, \quad (2.34)$$

with  $h$  denoting the thickness of the wall. As it can be noted,  $\mathbf{f}_v^{(b)}$  denotes the generalized forces associated to bulk loads acting in the plane of the cross-section,  $b_s$  and  $b_n$ , and  $\mathbf{f}_w^{(b)}$  the generalized forces associated to  $b_z$ . The generalized surface forces  $\mathbf{f}^{(p)}$  are defined

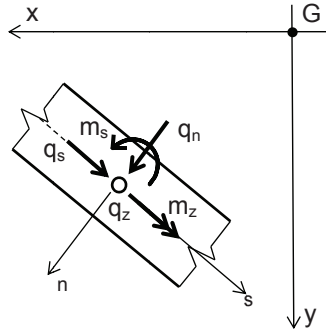


Figure 2.4: Wall thickness resultants of bulk loads.

following the same path outlined for  $\mathbf{f}^{(b)}$ . In particular, it can be easily verified that they can be written as:

$$\mathbf{f}_v^{(p)} = - \int_l \nabla \boldsymbol{\omega} |_{n=0} (\mathbf{p}_{in}^{(+)} + \mathbf{p}_{in}^{(-)}) ds - \int_l \partial_s \boldsymbol{\psi}^T \left( \frac{p_s^{(+)} - p_s^{(-)}}{2} \right) h ds,$$

$$\mathbf{f}_w^{(p)} = \int_l \boldsymbol{\varphi}^T (p_z^{(+)} + p_z^{(-)}) ds + \int_l \boldsymbol{\psi}^T \left( \frac{p_z^{(+)} - p_z^{(-)}}{2} \right) h ds, \quad (2.35)$$

being  $\mathbf{f}^{(p)\text{T}} = \begin{bmatrix} \mathbf{f}_v^{(p)\text{T}} & \mathbf{f}_w^{(p)\text{T}} \end{bmatrix}$ , and  $\mathbf{p}_{in}^{\text{T}} = \begin{bmatrix} p_s & p_n \end{bmatrix}$  and  $p_z$  the loads on the bottom and top faces of the walls, identified with the superscript (+) or (−) according to the sign of  $n$  on said surfaces. Finally, the generalized forces  $\mathbf{f}^{\text{T}} = \begin{bmatrix} \mathbf{f}_v^{\text{T}} & \mathbf{f}_w^{\text{T}} \end{bmatrix}$  are obtained as sum of the bulk and surface generalized forces:

$$\mathbf{f}_v = \mathbf{f}_v^{(b)} + \mathbf{f}_v^{(p)}, \quad \mathbf{f}_w = \mathbf{f}_w^{(b)} + \mathbf{f}_w^{(p)}. \quad (2.36)$$

### 2.3.2 Generalized inertia forces

Generalized inertia forces  $\mathbf{f}^{(i)}$  can be written as:

$$\mathbf{f}^{(i)} = -\mathbf{m}\ddot{\mathbf{u}}, \quad (2.37)$$

where a superposed dot denotes the time derivative and  $\mathbf{m}$  is the generalized inertia matrix, defined according to the following kinetic energy equivalence condition:

$$\frac{1}{2} \int_A \rho \dot{\mathbf{d}}^{\text{T}} \dot{\mathbf{d}} \, dA = \frac{1}{2} \int_A \dot{\mathbf{u}}^{\text{T}} \mathbf{m} \dot{\mathbf{u}} \, dA. \quad (2.38)$$

Substituting Eq. (2.15) in Eq. (2.38) and integrating over the wall thickness yield:

$$\mathbf{m} = \int_A \rho \mathbf{U}^{\text{T}} \mathbf{U} \, dA = \begin{bmatrix} \mathbf{m}_v & \mathbf{0} \\ \mathbf{0} & \mathbf{m}_w \end{bmatrix}, \quad (2.39)$$

where

$$\begin{aligned} \mathbf{m}_v &= \int_A \rho (\boldsymbol{\psi}^{\text{T}} \boldsymbol{\psi} + \boldsymbol{\xi}^{\text{T}} \boldsymbol{\xi}) \, dA \\ &= \int_l \rho \left( h |\nabla \boldsymbol{\omega}|_{n=0}^2 + \frac{h^3}{12} \partial_s \boldsymbol{\psi}^{\text{T}} \partial_s \boldsymbol{\psi} \right) \, ds, \end{aligned} \quad (2.40)$$

$$\mathbf{m}_w = \int_A \rho \boldsymbol{\omega}^{\text{T}} \boldsymbol{\omega} \, dA = \int_l \rho \left( h \boldsymbol{\varphi}^{\text{T}} \boldsymbol{\varphi} + \frac{h^3}{12} \boldsymbol{\psi}^{\text{T}} \boldsymbol{\psi} \right) \, ds. \quad (2.41)$$

### 2.3.3 Dynamic equilibrium equations

Invoking the D'Alembert form of the Principle of Virtual Work, it is possible to write the dynamic equilibrium equations in the form:

$$\mathbf{D}^* \mathbf{s} = \mathbf{f} - \mathbf{m}\ddot{\mathbf{u}}, \quad (2.42)$$

where  $\mathbf{D}^*$  is the equilibrium operator,  $\mathbf{D}^* = \mathbf{I}_m \otimes \mathcal{L}^*$ , being  $\mathcal{L}^*$  the differential operator adjoint to  $\mathcal{L}$ . Expressing  $\mathbf{s}$ ,  $\mathbf{f}$  and  $\mathbf{m}$  in terms of their components, the equilibrium equations (2.42) take the form:

$$\mathbf{S} - \frac{1}{2} \partial_z \mathbf{T} - \partial_z \mathbf{V} - \mathbf{f}_v + \mathbf{m}_v \ddot{\mathbf{v}} = \mathbf{0}, \quad (2.43)$$

$$-\partial_z \mathbf{M} + \frac{1}{2} \mathbf{T} - \mathbf{V} - \mathbf{f}_w + \mathbf{m}_w \ddot{\mathbf{w}} = \mathbf{0}. \quad (2.44)$$

Moreover, the same variational framework yields also the following boundary conditions:

$$\begin{aligned} \mathbf{M} = \pm \bar{\mathbf{W}} & \quad \text{or} \quad \mathbf{w} = \bar{\mathbf{w}}, \\ \frac{\mathbf{T}}{2} + \mathbf{V} = \pm \bar{\mathbf{Q}} & \quad \text{or} \quad \mathbf{v} = \bar{\mathbf{v}}, \end{aligned} \quad (2.45)$$

where a superposed bar denotes a quantity assigned on the extreme bases. In particular, in the above equations the following definitions have been introduced:

$$\bar{\mathbf{W}} = \int_A \boldsymbol{\omega} t_z dA, \quad \bar{\mathbf{Q}} = \int_A (\boldsymbol{\psi} t_n - \partial_s \boldsymbol{\varphi} t_s) dA - \int_A n \partial_s \boldsymbol{\psi} t_s dA, \quad (2.46)$$

where  $t_s$ ,  $t_n$  and  $t_z$  are the surface forces applied on the extreme bases of the beam, in direction  $s$ ,  $n$  and  $z$ , respectively. It is worth to note that the second boundary condition involve the quantity  $\frac{\mathbf{T}}{2} + \mathbf{V}$  that, as discussed in [47], leads to the total twisting moment.

### 2.3.4 Constitutive law

The material is assumed linearly elastic and isotropic. Since the beam model is based on a kinematic ansatz that leads to internal constraints it tends to be over stiff. In the framework of the classic GBT, a typical way to address this problem is to properly adjust the constitutive equations. In particular, the following form is usually assumed:

$$\boldsymbol{\sigma} = \mathbb{C}^\lambda \boldsymbol{\lambda} + \mathbb{C}^\chi \boldsymbol{\chi} \quad (2.47)$$

where

$$\mathbb{C}^\lambda = \begin{bmatrix} E & 0 & 0 & 0 \\ 0 & E & 0 & 0 \\ 0 & 0 & G & 0 \\ 0 & 0 & 0 & G \end{bmatrix}, \quad \mathbb{C}^\chi = \begin{bmatrix} \bar{E} & \nu \bar{E} & 0 & 0 \\ \nu \bar{E} & \bar{E} & 0 & 0 \\ 0 & 0 & G & 0 \\ 0 & 0 & 0 & G \end{bmatrix}, \quad (2.48)$$

and  $\boldsymbol{\lambda}$  and  $\boldsymbol{\chi}$  are the vectors collecting, respectively, the membrane and the bending parts of the strain components. Also,  $E$  is the Young's modulus,  $G$  the shear modulus and  $\bar{E} = E/(1 - \nu^2)$  being  $\nu$  the Poisson coefficient. It should be noted that the same result could be obtained by assuming the same biaxial constitutive law for both the membrane and bending part and, then, assuming null the Poisson coefficient for the membrane part. Indeed, alternative proposals can be found in the literature. For example, in [97] a uniaxial constitutive law is assumed for both the membrane and bending parts, so neglecting any coupling of axial and transverse strain, and the plate type elasticity modulus  $\bar{E}$  is used in the trans-

verse direction.

The cross-section stiffness matrix  $\mathbf{C}$  (that is the constitutive law of the beam model) can be derived by the following work-equivalence condition

$$\int_A [\boldsymbol{\lambda} + \boldsymbol{\chi}]^T [\mathbf{C}^\lambda \boldsymbol{\lambda} + n\mathbf{C}^\chi \boldsymbol{\chi}] dA = \mathbf{e}^T \mathbf{C} \mathbf{e}, \quad (2.49)$$

and takes the form

$$\mathbf{C} = \begin{bmatrix} \mathbf{C}_S^{(f)} & \mathbf{C}_{SM}^{(f)} & \mathbf{0} & \mathbf{0} \\ \mathbf{C}_{SM}^{(f)} & \mathbf{C}_M^{(f)} & \mathbf{0} & \mathbf{0} \\ \mathbf{0} & \mathbf{0} & \mathbf{C}_T^{(f)} & \mathbf{0} \\ \mathbf{0} & \mathbf{0} & \mathbf{0} & \mathbf{C}_V^{(f)} \end{bmatrix}, \quad (2.50)$$

where:

$$\mathbf{C}_S^{(f)} = E \int_A n^2 \partial_{ss} \boldsymbol{\psi}^T \partial_{ss} \boldsymbol{\psi} dA, \quad (2.51)$$

$$\mathbf{C}_{SM}^{(f)} = \nu \bar{E} \int_A n^2 \partial_{ss} \boldsymbol{\psi}^T \boldsymbol{\psi} dA, \quad (2.52)$$

$$\mathbf{C}_M^{(f)} = \int_A (\bar{E} n^2 \boldsymbol{\psi}^T \boldsymbol{\psi} + E \boldsymbol{\varphi}^T \boldsymbol{\varphi}) dA = E \int_A \bar{\boldsymbol{\omega}}^T \bar{\boldsymbol{\omega}} dA, \quad (2.53)$$

$$\mathbf{C}_T^{(f)} = 4G \int_A n^2 \partial_s \boldsymbol{\psi}^T \partial_s \boldsymbol{\psi} dA = G \frac{t^3}{3} \int_l \partial_s \boldsymbol{\psi}^T \partial_s \boldsymbol{\psi} ds, \quad (2.54)$$

$$\mathbf{C}_V^{(f)} = G \int_A (\nabla \boldsymbol{\omega}^T |_{n=0} \nabla \boldsymbol{\omega} |_{n=0}) dA \quad (2.55)$$

$$= G \int_A (\partial_s \boldsymbol{\varphi}^T \partial_s \boldsymbol{\varphi} + \boldsymbol{\psi}^T \boldsymbol{\psi}) dA, \quad (2.56)$$

and

$$\bar{\boldsymbol{\omega}} = \boldsymbol{\varphi} - n \sqrt{\frac{\bar{E}}{E}} \boldsymbol{\psi}. \quad (2.57)$$

### 2.3.5 Modal transformation

In general, the various submatrices composing the cross-stiffness matrix  $\mathbf{C}$  are full, so determining an high coupling among the gen-

eralized deformation parameters and, hence, in the final governing equations. In addition, the mechanical meaning of the generalized deformation parameters is not at all obvious and, in particular, the classical parameters of standard beam theories cannot be clearly distinguished. However, a modal transformation is sufficient to gain a partial uncoupling among the generalized parameters and, what is most important, to shed light on their mechanical meaning. The new basis is termed as modal base and the transformation as modal decomposition. Hereinafter, whenever a generic matrix/vector "." is expressed in the modal space, the symbol "hat" is used. In the modal space, matrices  $\hat{\mathbf{C}}_S^{(f)}$  and  $\hat{\mathbf{C}}_M^{(f)}$  are diagonal and can be written as:

$$\left\{ \hat{\mathbf{C}}_S^{(f)} \right\}_{ii} = \bar{E} \Lambda_i, \quad \left\{ \hat{\mathbf{C}}_M^{(f)} \right\}_{ii} = E I_i, \quad (2.58)$$

where  $\Lambda_i = \int_A n^2 \partial_{ss} \psi_i \, dA$ ,  $I_i = \int_A \bar{\omega}_i^2 \, dA$ .

To fix the ideas, in Fig. 2.5 the displacements corresponding to the six fundamental flexural modes of a C-shaped cross-section after the modal decomposition are shown. It can be seen how the classical generalized deformations of a Vlasov beam are recovered, such as axial extension (mode 1), major and minor axis bending (mode 2 and 3), and twisting rotation about the shear centre (mode 4). Mode 5 and 6 are typical GBT higher-order flexural deformations involving section distortion. The interested reader can refer to [46] for further details on the modal decomposition procedure.

## 2.4 Nonlinear warping formulation

In this section, the GBT formulation for nonlinear warping deformation modes is presented. Recalling the expression of matrix  $\mathbf{E}$  for nonlinear warping deformation modes, Eq. (2.23), and following the same path outlined in Section 2.3 for the flexural formulation, it can be easily verified that, for the nonlinear warping modes, the generalized stresses read as:

$$\mathbf{M} = \int_A \boldsymbol{\varphi}^T \sigma_{zz} dA, \quad (2.59)$$

$$\mathbf{T} = \int_A \partial_s \boldsymbol{\varphi}^T \tau_{zs} dA, \quad (2.60)$$

$$\mathbf{V} = -\frac{1}{2} \int_A \partial_s \boldsymbol{\varphi}^T \tau_{zs} dA, \quad (2.61)$$

and the cross-section stiffness matrix as:

$$\mathbf{C} = \begin{bmatrix} \mathbf{0} & \mathbf{0} & \mathbf{0} & \mathbf{0} \\ \mathbf{0} & \mathbf{C}_M^{(w)} & \mathbf{0} & \mathbf{0} \\ \mathbf{0} & \mathbf{0} & \mathbf{C}_T^{(w)} & \mathbf{C}_{TV}^{(w)} \\ \mathbf{0} & \mathbf{0} & \mathbf{C}_{TV}^{(w)} & \mathbf{C}_V^{(w)} \end{bmatrix}, \quad (2.62)$$

being

$$\mathbf{C}_M^{(w)} = E \int_A \boldsymbol{\varphi}^T \boldsymbol{\varphi} dA, \quad (2.63)$$

$$\mathbf{C}_T^{(w)} = G \int_A \partial_s \boldsymbol{\varphi}^T \partial_s \boldsymbol{\varphi}, \quad (2.64)$$

$$\mathbf{C}_V^{(w)} = \frac{G}{4} \int_A \partial_s \boldsymbol{\varphi}^T \partial_s \boldsymbol{\varphi} dA, \quad (2.65)$$

$$\mathbf{C}_{TV}^{(w)} = -\frac{G}{2} \int_A \partial_s \boldsymbol{\varphi}^T \partial_s \boldsymbol{\varphi} dA. \quad (2.66)$$

Of course, if both the flexural-shear and the nonlinear warping deformation modes are considered, then the cross-section stiffness

matrix should be obtained by superposing those of Eqs. (2.50) and (2.62) and adding the coupling terms between the two classes of modes (that can be evaluated using the same arguments employed to obtain the other terms). This case is not reported here for the sake of brevity. The modal decomposition procedure follows the same lines of that given in [46].

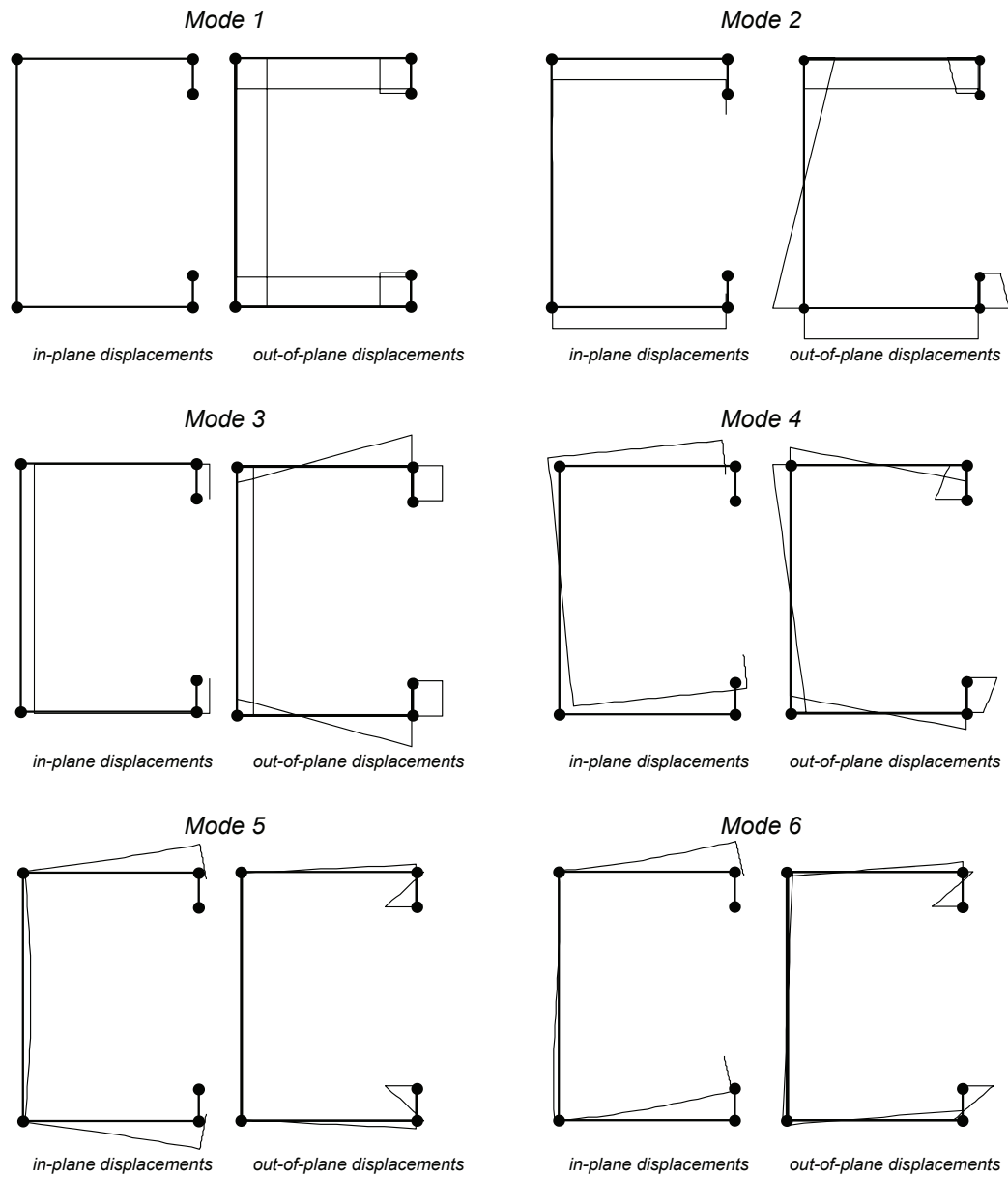


Figure 2.5: C cross-section: in- and out-of-plane displacements corresponding to the six fundamental flexural modes after modal decomposition.

# Chapter 3

## Constitutive relations and consistency

### Abstract

This chapter focuses on the constitutive assumptions, both for the isotropic and orthotropic cases, and consistency in the framework of the Generalized Beam Theory. In particular, following the ideas presented in [51], a novel approach based on energetic arguments is discussed. Moreover, the concept of consistency of a GBT-based model is established and a consistency analysis is shown. This yields a formal rational basis to investigate the effects of the various families of cross-section deformation modes in terms of predictive capabilities of the GBT model. Some numerical examples illustrate the arguments exposed in this chapter.

This chapter is organized as follows. In Section 3.1, in view of further developments, the GBT strain field is rewritten by splitting it into the membrane and bending parts. The GBT kinematic constraints are discussed in section 3.2, while Sections 3.3 and 3.4

are devoted to the development of a novel approach able to automatically select appropriate constitutive relations in accordance with the GBT kinematics and of the consistency analysis. Some numerical examples (Section 3.5) close this chapter.

### 3.1 Strain field

Start from the strain field presented in Eq. (2.16) (considering for simplicity the static case) and rewrite the equation splitting it into a membrane part, not depending on  $n$  and denoted by  $\boldsymbol{\lambda}$ , and a bending part, depending on  $n$  and denoted by  $\boldsymbol{\chi}$ . This leads to

$$\boldsymbol{\varepsilon} = \boldsymbol{\lambda} + n\boldsymbol{\chi}, \quad (3.1)$$

where

$$\boldsymbol{\lambda} = \begin{bmatrix} \lambda_{zz} \\ \lambda_{ss} \\ \lambda_{zs} \\ \lambda_{zn} \end{bmatrix} = \mathbf{E}^\lambda \mathbf{e}, \quad \boldsymbol{\chi} = \begin{bmatrix} \chi_{zz} \\ \chi_{ss} \\ \chi_{zs} \\ \chi_{zn} \end{bmatrix} = \mathbf{E}^\chi \mathbf{e}, \quad (3.2)$$

being

$$\mathbf{E}^\lambda = \begin{bmatrix} 0 & \phi & 0 & 0 \\ \partial_s \mu & 0 & 0 & 0 \\ 0 & 0 & \mu + \partial_s \phi & \frac{1}{2}(\mu - \partial_s \phi) \\ 0 & 0 & 0 & \psi \end{bmatrix}, \quad \mathbf{E}^\chi = \begin{bmatrix} 0 & -\psi & 0 & 0 \\ -\partial_{ss} \psi & 0 & 0 & 0 \\ 0 & 0 & -2\partial_s \phi & 0 \\ 0 & 0 & 0 & 0 \end{bmatrix}. \quad (3.3)$$

Using Eq. (3.1), Eq. (2.24) (integrated over  $n$ ) takes the form:

$$\mathbf{e}^T \mathbf{s} = \int_s (\boldsymbol{\lambda}^T \mathbf{n} + \boldsymbol{\chi}^T \mathbf{m}) \, ds, \quad (3.4)$$

where  $\mathbf{n}$  and  $\mathbf{m}$  collect the plate-like stress resultants:

$$\mathbf{n} = \begin{bmatrix} n_{zz} \\ n_{ss} \\ n_{zs} \\ n_{zn} \end{bmatrix} = \int_n \begin{bmatrix} \sigma_{zz} \\ \sigma_{ss} \\ \tau_{zs} \\ \tau_{zn} \end{bmatrix} dn, \quad \mathbf{m} = \begin{bmatrix} m_{zz} \\ m_{ss} \\ m_{zs} \\ m_{zn} \end{bmatrix} = \int_n n \begin{bmatrix} \sigma_{zz} \\ \sigma_{ss} \\ \tau_{zs} \\ \tau_{zn} \end{bmatrix} dn. \quad (3.5)$$

Assuming the constitutive relation for  $\boldsymbol{\lambda}$  and  $\boldsymbol{\chi}$  given by Eq. (2.47), the relationship defining the cross-section stiffness matrix takes the form:

$$\mathbf{e}^T \mathbf{C} \mathbf{e} = \int_s [\boldsymbol{\lambda}^T \mathbf{C}^\lambda \boldsymbol{\lambda} + \boldsymbol{\chi}^T \mathbf{C}^\chi \boldsymbol{\chi}] ds, \quad (3.6)$$

being

$$\mathbf{C}^\lambda = \int_n \mathbf{C}^\lambda dn, \quad \mathbf{C}^\chi = \int_n n^2 \mathbf{C}^\chi dn. \quad (3.7)$$

Comparing Eqs. (3.4), (2.49) and (3.6), it is then possible to recognize the classical plate constitutive relations as

$$\mathbf{n} = \mathbf{C}^\lambda \boldsymbol{\lambda}, \quad \mathbf{m} = \mathbf{C}^\chi \boldsymbol{\chi}. \quad (3.8)$$

## 3.2 Kinematic constraints

The particular mode functions described above induce a series of constraints on the beam kinematics. In particular, it can be easily verified that FFS and LFS modes engender null  $\lambda_{ss}$  and  $\chi_{zn}$  and piecewise constant (i.e. constant on each wall)  $\lambda_{zs}$  along the section midline. Moreover, NLW modes engender  $\varepsilon_{ss} = \gamma_{zn} = 0$ . In

addition to this,  $\chi_{zn}$ ,  $\varepsilon_{nn}$  and  $\gamma_{sn}$  are always null stemming from the displacement field of the GBT formulation. From these considerations, we can define three distinct types of kinematic constraint present in the GBT:

**Type 1** - The first type of constraint is that in which a certain strain component is completely null (i.e. both the membrane and the bending part are null). This is the case for  $\varepsilon_{nn}$  and  $\gamma_{sn}$ .

**Type 2** - The second kind of constraint is characterized by only one part of a strain component being null, either the membrane part or the bending one. This is the case for  $\lambda_{ss}$  and  $\chi_{zn}$ .

**Type 3** - In this case, no part of the strain component is null, but its representation over the generic wall is poor. This is the case for  $\lambda_{zs}$  which can only be constant over  $s$  when using FFS modes only.

Considering the aforementioned constraints, the most general form of the plate-like deformations  $\boldsymbol{\lambda}$  and  $\boldsymbol{\chi}$  is

$$\boldsymbol{\lambda} = \begin{bmatrix} \lambda_{zz} \\ 0 \\ \lambda_{zs} \\ \lambda_{zn} \end{bmatrix}, \quad \boldsymbol{\chi} = \begin{bmatrix} \chi_{zz} \\ \chi_{ss} \\ \chi_{zs} \\ 0 \end{bmatrix}. \quad (3.9)$$

It should be noticed that, in order to enrich the beam kinematic and allow non-null  $\lambda_{ss}$ , modes accounting for wall extension could

be introduced [44]. Nevertheless, such family of modes is only seldom adopted in the GBT literature and technical use, so that it is not considered in the following developments for simplicity.

### 3.3 A new approach for constitutive relations

The internal constraints described in the previous section render the GBT model over-stiff as usual in kinematically-based models. The usual solution to avoid such effect, at least for constraints of Type 1 and 2, is to adjust constitutive relations.

In this section, the approaches currently used to define constitutive relations for GBT-based models for isotropic and orthotropic cases are recalled and a new approach presented.

#### 3.3.1 Classical approaches

As anticipated in the previous chapter, in the isotropic case, it is common practice in the GBT literature using two different constitutive relations for membrane and bending strains. In particular, a mono-axial constitutive relation is used for the membrane part while a plane-stress constitutive relation is used for the bending part, see Eq. (2.48).

In the orthotropic case, such an approach is usually not followed. In fact, in such case, constitutive relations are obtained by assuming for both, membrane and bending parts, the same plane-stress constitutive relationship [48]. In particular, firstly the plane-stress

constitutive relation is transformed from the material reference system to the wall one (see Fig. 3.1), leading to constitutive matrices whose topology is

$$\mathbb{C}^\lambda = \mathbb{C}^\chi = \begin{bmatrix} C_{11} & C_{12} & C_{13} & 0 \\ C_{12} & C_{22} & C_{23} & 0 \\ C_{13} & C_{23} & C_{33} & 0 \\ 0 & 0 & 0 & C_{44} \end{bmatrix}, \quad (3.10)$$

where, due to the presence of the non-null terms  $C_{12}$ ,  $C_{13}$  and  $C_{23}$  stress components  $\sigma_{zz}$ ,  $\sigma_{ss}$  and  $\tau_{zs}$  are fully coupled. Then, two approaches can be found in the GBT literature in order to correct such constitutive relation aiming at accounting for restraints of Type 1 and Type 2. In particular, Silva et al. in [48] introduced the following distinction:

**Model A** - It consists in neglecting the product between the Poisson constants in the derivation of the plane stress constitutive matrix. Although used in the GBT literature, it has been found to lead to non-satisfactory results in the case of non-aligned orthotropic materials (overestimation of buckling loads up to 300% [48]).

**Model B** - It has been also applied to Vlasov-like beam models (see [98–100]) and assumes that the membrane transversal extensions  $\lambda_{ss}$  are free, which corresponds to adopting plate constitutive relations associated [35] with a null normal stress resultant in the transverse direction.

Independently of the material behaviour, that is in both the isotropic and orthotropic cases, once constitutive relations for the stress components  $\boldsymbol{\sigma}$  have been introduced, the cross-section stiffness matrix  $\mathbf{C}$  is derived as described in Section 3.1.

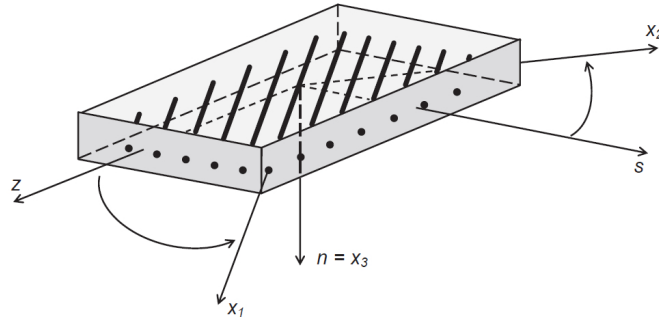


Figure 3.1: Orthotropic case: material  $(x_1, x_2, x_3)$  and wall  $(z, s, n)$  reference systems.

### 3.3.2 An alternative unified approach

As already stated, the adoption of two different constitutive relations for the membrane and the bending parts is not desirable. In the following, an approach, able to automatically identify constitutive relations consistent with the adopted kinematic hypotheses, is presented.

Using the same format presented in Eq. (3.1), it is possible to assume a stress field representation which mirrors the strain components induced by the kinematic constraints. It is then possible to write

$$\boldsymbol{\sigma} = \frac{\mathbf{n}}{t} + n \frac{\mathbf{m}}{j}, \quad (3.11)$$

where  $t$  is the wall thickness,  $j = t^3/12$  is its inertia with respect

to the wall midline, and zero and non-zero terms in  $\mathbf{n}$  and  $\mathbf{m}$  are selected according to Eq. (3.9), that is

$$\mathbf{n} = \begin{bmatrix} n_{zz} \\ 0 \\ n_{zs} \\ n_{zn} \end{bmatrix}, \quad \mathbf{m} = \begin{bmatrix} m_{zz} \\ m_{ss} \\ m_{zs} \\ 0 \end{bmatrix}. \quad (3.12)$$

In this way, a perfect duality between stress and strain field is established. It is then possible to calculate the complementary energy per unit area of the wall mid-surface associated to such stress field:

$$\Psi(z, s) = \frac{1}{2} \int_n \boldsymbol{\sigma}^T(z, s, n) \mathbb{H} \boldsymbol{\sigma}(z, s, n) \, dn, \quad (3.13)$$

where  $\mathbb{H}$  is the compliance matrix of the material (isotropic or orthotropic). By introducing Eq. (3.11) into (3.13) it is possible to write the complementary energy in terms of the plate-like stresses  $\mathbf{n}$  and  $\mathbf{m}$ . The complementary energy can then be differentiated with respect to  $\mathbf{n}$  and  $\mathbf{m}$  to obtain their corresponding membrane strain and curvature terms

$$\lambda_{jk} = \frac{d\Psi}{dn_{jk}}, \quad \chi_{jk} = \frac{d\Psi}{dm_{jk}}, \quad (3.14)$$

and, thus, leading to the identification of the following constitutive relations

$$\boldsymbol{\lambda} = \mathbf{H}^\lambda \mathbf{n}, \quad \boldsymbol{\chi} = \mathbf{H}^\chi \mathbf{m}. \quad (3.15)$$

Then, these relations are inverted in order to calculate  $\mathbf{C}^\lambda$  and  $\mathbf{C}^\chi$ , adopted for the evaluation of the cross-section stiffness matrix

as reported in Eq. (2.49). It can be easily verified that such an approach leads to the assumption given by Eq. (2.48) for isotropic materials while, for orthotropic materials, leads to the Model B presented in Section 3.3.1.

### 3.4 Consistency

The over-stiffening of the GBT beam model due to the internal constraints of Type 1 and Type 2 can be cured by constructing the constitutive relations following the approach described in the previous section. Also constraints of Type 3 produce an over-stiffening of the model, so leading to a decrease in the model accuracy, but its treatment is different from the one used for Type 1 and 2.

For the case of isotropic materials this problem is traditionally dealt with by considering correction factors which take into account the effect of the constraints by reducing the system stiffness. These are successfully applied to classical beam models but their extension to non-classical ones is not always straightforward.

Furthermore, when orthotropic materials are considered, resorting to the correction factors can be very complex and not always effective since the constitutive relations are strongly coupled and it is necessary to ensure the coherence, or rather consistency, between the representations of the stress and strain components which, through energetic equivalence, contribute to the definition of the cross-section stiffness matrix.

On this regard, consider Eq. (3.6), which defines the cross-

section stiffness matrix  $\mathbf{C}$ . Notice that the integral on the r.h.s. expresses the work done by the stresses  $\mathbf{C}^\lambda \boldsymbol{\lambda}$  and  $\mathbf{C}^\chi \boldsymbol{\chi}$ , coming from the assumed deformation modes via the constitutive relationships, on the corresponding strain components,  $\boldsymbol{\lambda}$  and  $\boldsymbol{\chi}$ , related to the assumed deformation modes. Then, only those stress terms which actually do work participate in determining the cross-section stiffness matrix and, hence, the response of the GBT model. On the other hand, those stress terms which do not work, if any, are not sensed by the resulting cross-section stiffness matrix. On this basis, those stress terms which actually do work are defined as consistent, and the condition which ensures that the whole stress actually does work is the consistency condition. These energy arguments can be formulated following a way similar to that proposed in [55–58]. The contributions to the work due to each stress and strain component are considered separately and the consistency condition is established as: each stress component should belong to the space that the assumed deformation mode involves for the corresponding strain component.

Of course, the lack of consistency diminishes the accuracy of the GBT model predictions, since the solution reflects only the consistent part of the stress field. Moreover, it can be easily argued that the more the representation bases of the stress/strain components are poor, the more evident are the effects of the lack of consistency.

Let's now examine the representations of the various strain components engendered by the different families of the deformation

modes and of the corresponding stress components obtained via the constitutive relations. For the sake of generality, reference is made to coupled constitutive matrices like that of the orthotropic case (see Eq. (3.10)).

Table 3.1 collects the degree of the  $s$  variable in the polynomial representation base of the various strain and stress components if only FFS modes are used. On this regard, it should be observed that, as already stated, only if the number of natural nodes,  $nn$ , is higher than 4, then the FFS modes account for section distortion and, hence, engender non-null  $\chi_{ss}$  on all the walls.

Comparing the first two columns in Tab. 3.1 clearly shows that the consistency condition is violated three times, as highlighted in the third column of the same table, so leading to a lack of consistency. In particular, the lack of consistency originates from the mismatch between the representation bases of the stress components of  $n_{zs}$ ,  $m_{ss}$  and  $m_{zs}$  and those of the corresponding strain components,  $\lambda_{zs}$ ,  $\chi_{ss}$  and  $\chi_{zs}$ , respectively.

The above inconsistencies are expected to yield low accuracy in all those problems where the inconsistent stress-strain components play an important role. In particular, the inconsistency related to the membrane term  $\lambda_{zs}$  is expected to have highest impact in problems dominated by the membrane part and, thus, in shear-dominated problems. In the following, this inconsistency is denoted as membrane inconsistency. On the other hand, the inconsistency related to  $\chi_{ss}$  affects the bending part and is denoted

FFS				
Strain		Stress		Inc.
$\lambda_{zz}$	linear	$n_{zz}$	linear	
$\lambda_{ss}$	null	$n_{ss}$	null	
$\lambda_{zs}$	constant	$n_{zs}$	linear	×
$\lambda_{zn}$	cubic	$n_{zn}$	cubic	
$\chi_{zz}$	cubic	$m_{zz}$	cubic	
$\chi_{ss}$	$\left\{ \begin{array}{l} \text{linear if } nn > 4 \\ \text{null otherwise} \end{array} \right.$	$m_{ss}$	cubic	×
$\chi_{zs}$	quadratic	$m_{zs}$	cubic	×
$\chi_{zn}$	null	$m_{zn}$	null	

Table 3.1: FFS modes - Degree of the  $s$  variable in the polynomial representation of strain and stress components.

LFS		NLW	
$\lambda_{zz}$	null	$\lambda_{zz}$	pw linear
$\lambda_{ss}$	null	$\lambda_{ss}$	null
$\lambda_{zs}$	null	$\lambda_{zs}$	pw constant
$\lambda_{zn}$	null	$\lambda_{zn}$	null
$\chi_{zz}$	pw cubic	$\chi_{zz}$	null
$\chi_{ss}$	pw linear	$\chi_{ss}$	null
$\chi_{zs}$	pw quadratic	$\chi_{zs}$	null
$\chi_{zn}$	null	$\chi_{zn}$	null

Table 3.2: LFS and NLW modes - Degree of the  $s$  variable in the polynomial representation of strain components. The symbol 'pw' indicates piecewise polynomial representations.

in the following as bending inconsistency. Such last inconsistency is expected to mainly impact problems characterized by significant section distortion. In particular, this inconsistency is expected to cause the worst effects when  $nn = 4$  since, in that case, there is the maximum mismatch between the representation bases of the stress component  $m_{ss}$  (cubic) and that of the strain component

$\chi_{ss}$  (null). The third inconsistency is related to the mismatch between  $\chi_{zs}$  and  $m_{zs}$ . Hence, it is expected to mainly affect problems which involve significant twisting of the beam walls. Nevertheless, it should be noticed that, in this case, the inconsistency involves stresses and strains whose polynomial representation base involves relatively high order terms (cubic stress and quadratic strain) and, therefore, such inconsistency is not expected to yield significant detriment of the model accuracy.

The modular nature of the GBT offers *per sé* the possibility to cure such inconsistencies by resorting to the appropriate families of deformation modes. On this regard, Tab. 3.2 reports the polynomial representation degree for the strain components for both LFS and NLW modes. By comparing Tabs. 3.1 and 3.2, it clearly appears that the adoption of LFS modes alleviates the bending inconsistency of FFS while the adoption of NLW alleviates the membrane inconsistency of FFS. Indeed, it is observed that the inconsistency is still present within the LFS and NLW mode families since, via constitutive relations, their introduction further enrich the stress field description too. Examining LFS, for example, the adoption of LFS engenders piecewise cubic  $m_{ss}$  and  $m_{zs}$  (see Tab. 3.2) while  $\chi_{ss}$  is only piecewise linear and  $\chi_{zs}$  piecewise quadratic. Nevertheless, the energy associated to such inconsistent part of the stress field is expected to be small and can be reduced by the refinement of internal nodes.

In the following, the exposed arguments are illustrated through

some numerical examples.

### 3.5 Numerical examples

In order to highlight the the role played by the inconsistencies described in Section 3.4 and shed some light on the role played by the different cross-section deformation modes, in this section, numerical results obtained with the present GBT formulation are presented and compared to those of finite elements shell models solved with the finite element solver Code\_Aster [101].

GBT Numerical results are obtained by a finite element code, named CAPS, developed at the Laboratory of Computational Mechanics, DICAM, University of Bologna ([www.unibo.it/LAMC](http://www.unibo.it/LAMC)). Over the generic finite element,  $\mathbf{v}$ -parameters are approximated by cubic polynomials, while  $\mathbf{w}$ -parameters are approximated by quadratic polynomials.

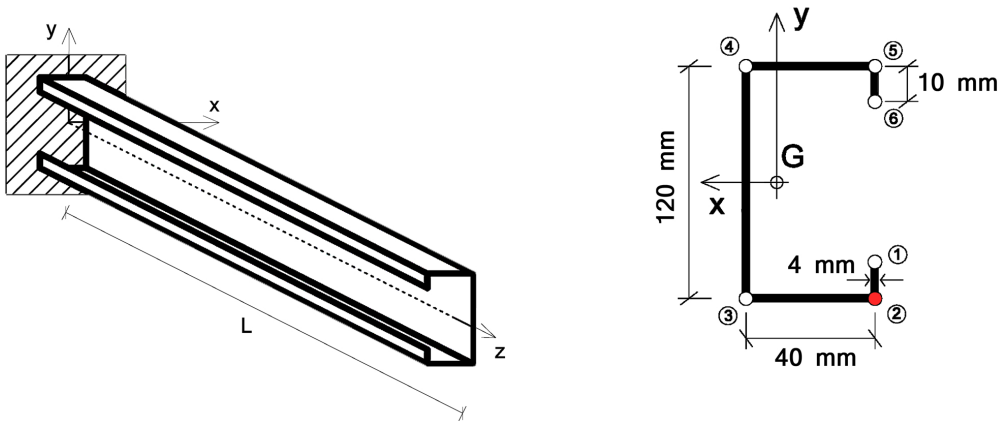


Figure 3.2: C-section cantilever beam.

In the numerical examples, a cantilever beam of length  $L = 600\text{ mm}$  characterized by a C cross-section with lips is considered.

The details of the cross-sections geometry are reported in Fig. 3.2. The considered linear elastic orthotropic material is characterized by the mechanical properties reported in Tab. 3.3. Various values of the angle  $\theta$  between the beam and the material reference systems are considered.

$E_1$	$E_2$	$E_3$	$\nu_{12}$	$\nu_{23}$	$\nu_{13}$	$G_{12}$	$G_{23}$	$G_{13}$
$1.7E5$	$3.3E4$	$5.2E3$	0.036	0.171	0.25	$9.4E3$	$3.3E3$	$8.3E3$

Table 3.3: Mechanical properties of the adopted orthotropic material. Young and shear moduli are expressed in  $MPa$ .

The numerical examples are run with four different settings:

**S1** - Only FFS modes are considered

**S2** - FFS modes combined with LFS modes

**S3** - FFS modes combined with NLW modes

**S4** - All modes

Moreover, two sets of numerical simulations have been performed in order to check the solution sensitivity to the number of internal nodes for both LFS modes and NLW modes. Internal nodes have been equally spaced and distributed on the beam cross-section with two refinement levels: a coarse one named  $C$  and a fine one named  $F$ . In particular, for each wall of the cross section, they correspond to 0-1-3-1-0 and 3-7-23-7-3 internal nodes, respectively.

Results are presented in terms of total deformation energy, denoted as  $\mathcal{E}$ , and  $y$  displacement at the free end, denoted as  $dy$ , in

correspondence to the natural node ② as reported in Fig. 3.2. For the sake of clarity the percentage difference between the shell model and the GBT results is also reported.

In order to highlight the effects of the lack of consistency discussed in Sec. 3.4, two loading conditions are considered as reported in Fig. 3.3.

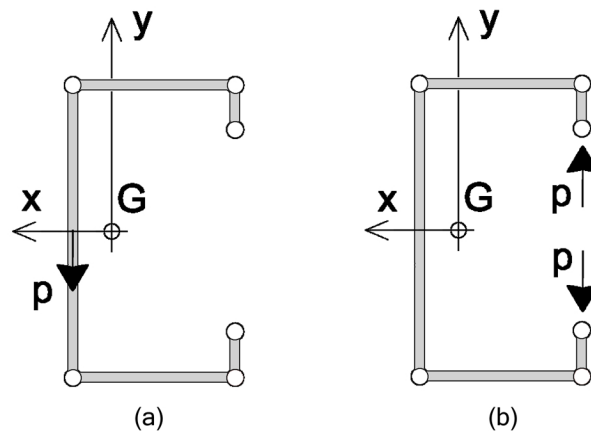


Figure 3.3: Loading conditions: (a) shearing load, (b) distortional load.

### 3.5.1 Example 1: Shearing load

The cantilever beam is subjected to a shearing load given by a concentrated force at the free edge equal to  $p = 100 \text{ N}$  in the middle point of the vertical wall (see Fig. 3.3 (a)). In this case, the beam behaviour is expected to be dominated by the membrane contributions so that the example is used to highlight the effect of the membrane type inconsistency reported in Section 3.4.

As it can be easily deduced by analysing Tab. 3.4, a strong underestimation of the deformation energy and displacements is observed when the material principal axes are rotated of about  $30^\circ$

Deformation Energy [ $N \cdot mm$ ]									
$\theta$	Code_Aster	S1		S2		S3		S4	
	$\mathcal{E}$	$\mathcal{E}$	%	$\mathcal{E}$	%	$\mathcal{E}$	%	$\mathcal{E}$	%
0° C	2.9657	2.7186	8.69	2.7599	7.19	2.7550	7.37	2.7962	5.88
0° F	2.9657	-	-	2.7981	5.82	2.7709	6.79	2.8503	3.97
30° C	7.2052	4.9386	37.33	5.0461	35.25	6.5572	9.42	6.7464	6.58
30° F	7.2052	-	-	5.0846	24.65	6.7943	5.87	7.0644	1.97
60° C	11.1878	11.1027	0.76	11.1260	0.55	11.1669	0.19	11.1904	0.02
60° F	11.1878	-	-	11.1741	0.18	11.1778	0.09	11.2500	0.55
90° C	10.7517	10.6207	1.23	10.6365	1.08	10.6611	0.91	10.6699	0.76
90° F	10.7517	-	-	10.6611	0.90	10.6682	0.78	10.7086	0.40

Vertical displacement at $nn\ 2$ [ $mm$ ]									
$\theta$	Code_Aster	S1		S2		S3		S4	
	$dy$	$dy$	%	$dy$	%	$dy$	%	$dy$	%
0° C	-0.1022	-0.0977	4.47	-0.0988	3.45	-0.0990	3.15	-0.1001	2.14
0° F	-0.1022	-	-	-0.0999	2.34	-0.0997	2.53	-0.1018	0.45
30° C	-0.2205	-0.1517	37.02	-0.1531	36.08	-0.2057	6.97	-0.2092	5.30
30° F	-0.2205	-	-	-0.1541	35.46	-0.2145	2.76	-0.2203	0.09
60° C	-0.3661	-0.3658	0.09	-0.3665	0.09	-0.3680	0.52	-0.3687	0.71
60° F	-0.3661	-	-	-0.3689	0.75	-0.3684	0.63	-0.3716	1.48
90° C	-0.4125	-0.4099	0.63	-0.4106	0.47	-0.4110	0.36	-0.4117	0.20
90° F	-0.4125	-	-	-0.4116	0.22	-0.4115	0.24	-0.4132	0.18

Table 3.4: Numerical results for Example 1.

with respect to the beam axes and only FFS modes (setting  $S1$ ) are adopted (differences of about 30% are observed). Adding LFS modes (setting  $S2$ ) does not yield substantial improvements. Moreover, no convergence toward the reference solution is observed by increasing the number of internal nodes (i.e. passing from case  $30^\circ C$  to  $30^\circ F$ ). On the contrary, when NLW modes are introduced, already in the coarse configuration ( $C$ ) a substantial improvement of the solution accuracy is observed. This confirms that the unreliable

response of the  $S1$  setting is due to the membrane inconsistency described in Section 3.4, alleviated by the introduction of the NLW modes. Moreover, by increasing the number of internal nodes, accuracy is further increased. Finally, when the two mode families and the fine grid of internal nodes are considered simultaneously (cases  $F$  with  $S4$  settings), the solution is extremely close to the reference obtained with the shell model.

The deformed shapes obtained with the GBT by using settings  $S4$  with the  $C$  refinement are reported in Fig. 3.4 for various material orientations.

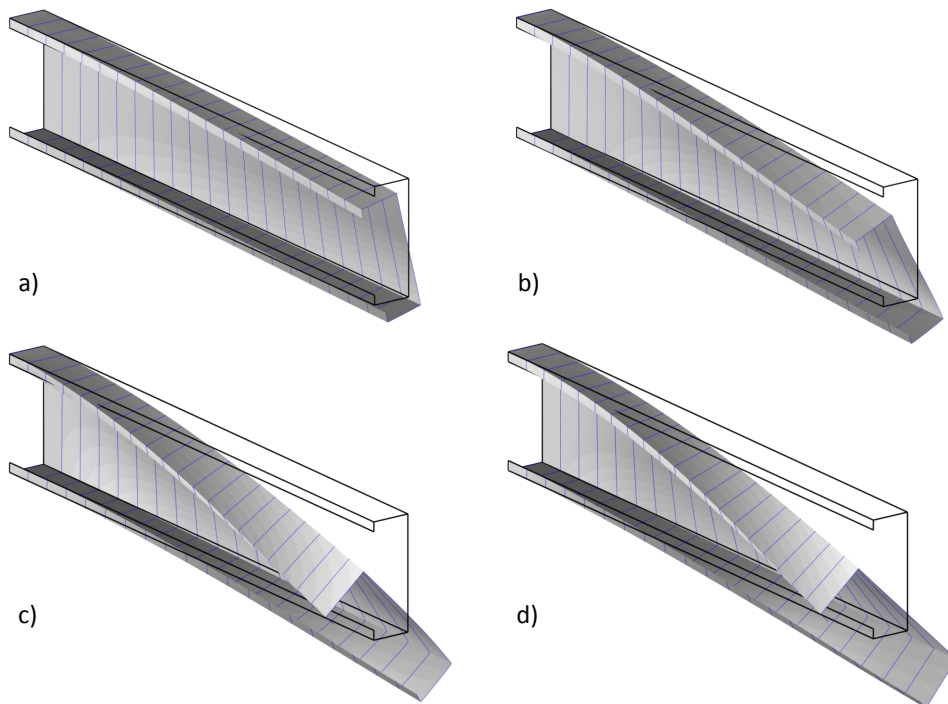


Figure 3.4: Example 1 - Deformed configurations obtained with the GBT by using settings  $S4$  with refinement  $C$  for various material orientations: (a)  $0^\circ$ , (b)  $30^\circ$ , (c)  $60^\circ$ , (d)  $90^\circ$ .

### 3.5.2 Example 2: Distortional load

This example aims at highlighting the effects of the bending inconsistency, which is typically triggered by the section distortion. Hence, in this case, the loading is composed of two distortional forces applied at the extreme natural nodes (see Fig. 3.3 (b)). Table 3.5 collects the values of the deformation energy and of the displacement for the various cases analyzed. As it can be noted, also in this example, using only FFS modes (setting S1) leads to considerable underestimation of the deformation energy and, consequently, of the displacement. On the other hand, contrarily to what has been observed in the previous example, now the introduction of NLW modes does not lead to a major improvement of the solution while the adoption of LFS modes leads to accurate results. This confirms that the unreliable response of the S1 settings is due to the bending inconsistency described in Section 3.4, alleviated by the introduction of the LFS modes. Finally, also in this case, the deformed shapes obtained with the GBT by using settings S4 with the  $C$  refinement are reported for various material orientations (see Fig. 3.5).

Deformation energy [ $N \cdot mm$ ]									
$\theta$	Code_Aster	S1		S2		S3		S4	
	$\mathcal{E}$	$\mathcal{E}$	%	$\mathcal{E}$	%	$\mathcal{E}$	%	$\mathcal{E}$	%
0° C	69.1815	67.7087	2.15	68.7139	0.68	67.9256	1.83	68.9735	0.30
0° F	69.1815	-	-	68.9597	0.32	68.0468	1.65	69.3676	0.27
30° C	48.9641	45.0218	8.39	47.7447	2.52	45.1214	8.17	47.8962	2.20
30° F	48.9641	-	-	48.6315	0.67	45.4765	7.39	49.3561	0.80
60° C	38.5751	36.4477	5.67	38.2079	0.96	36.4787	5.59	38.2407	0.87
60° F	38.5751	-	-	39.2144	1.64	36.5031	5.52	39.2798	1.81
90° C	30.5252	29.9076	2.04	30.4121	0.37	30.0016	1.73	30.5257	0.00
90° F	30.5252	-	-	30.5208	0.01	30.0543	1.55	30.7005	0.57

Vertical displacement at $nn\ 2$ [ $mm$ ]									
$\theta$	Code_Aster	S1		S2		S3		S4	
	$dy$	$dy$	%	$dy$	%	$dy$	%	$dy$	%
0° C	-0.6906	-0.6771	1.98	-0.6871	0.50	-0.6793	1.66	-0.6897	0.13
0° F	-0.6906	-	-	-0.6896	0.15	-0.6805	1.48	-0.6937	0.44
30° C	-0.3650	-0.3451	5.63	-0.3686	0.97	-0.3373	7.89	-0.3595	1.53
30° F	-0.3650	-	-	-0.3763	3.02	-0.3376	7.81	-0.3680	0.79
60° C	-0.1104	-0.0920	18.16	-0.1055	4.57	-0.0918	18.34	-0.1053	4.70
60° F	-0.1104	-	-	-0.1070	3.15	-0.0920	18.21	-0.1070	3.16
90° C	-0.3042	-0.2990	1.72	-0.3041	0.06	-0.3000	1.41	-0.3005	0.31
90° F	-0.3042	-	-	-0.3051	0.29	-0.3005	1.23	-0.3069	0.88

Table 3.5: Numerical results for Example 2.

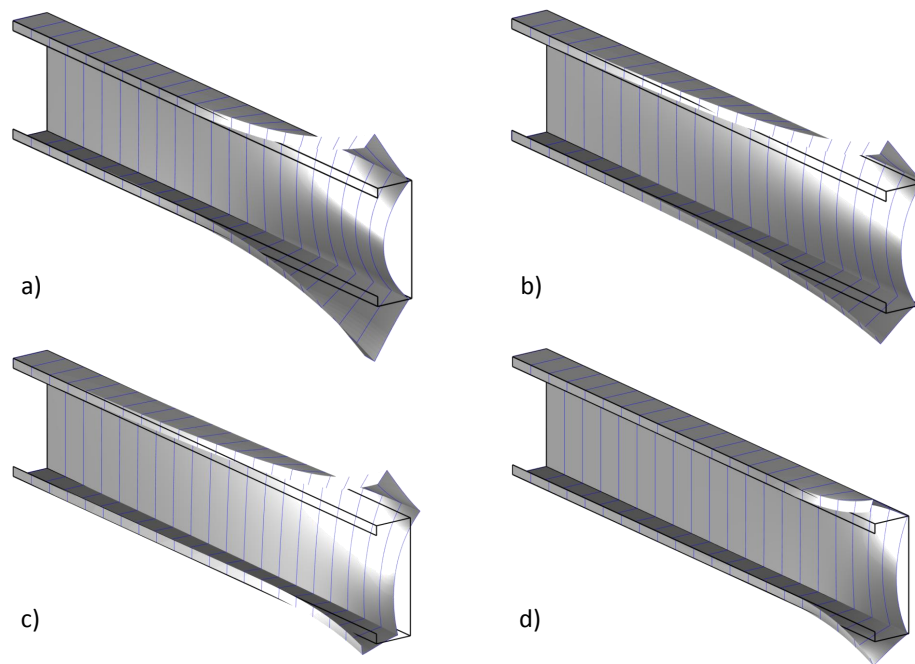


Figure 3.5: Example 2 - Deformed configurations obtained with the GBT by using settings  $S4$  with refinement  $C$  for various material orientations: (a)  $0^\circ$ , (b)  $30^\circ$ , (c)  $60^\circ$ , (d)  $90^\circ$ .



# Chapter 4

## Flexibility-based GBT finite element

### Abstract

In this chapter, following the ideas presented in [63], a new 2-node finite element for the Generalized Beam Theory based on the hybrid complementary energy functional is presented. It involves nodal displacements and equilibrating stresses within the element as independent variables. Assumed stresses are rationally derived basing on the stresses associated to analytical solutions of some particular cases. Displacements within the element are a posteriori recovered by shape functions based on the same solutions. Numerical results show the high performance of the finite element: generalized displacements and stresses are accurately predicted with very rough meshes, often using only one or two finite elements.

This chapter is organized as follows. Section 4.1 summarizes the fundamentals equations of the GBT. In Section 4.2, the analytical solution functions are presented. Section 4.3 is devoted to the de-

scription of the variational framework, the representation assumed for generalized stresses, the finite element equations and the a posteriori recovery of the generalized displacements. Finally, numerical tests are presented in Section 4.4.

In this chapter, all the quantities are to be intended as expressed in the modal base and the first four modes are denoted as *classic modes* and the other  $m_h = m - 4$  modes (being  $m$  the total number of modes) as *higher-order modes*.

## 4.1 Summary of the beam governing equations

Denote by  $L$  the length of the beam and decompose the domain of the  $z$ -variable into an internal part,  $\Omega = ]0, L[$ , and a boundary part, identified by  $\partial\Omega = \partial\Omega_N \cup \partial\Omega_D = \{0, L\}$ , being  $\partial\Omega_N$  and  $\partial\Omega_D$  the Neumann and Dirichlet boundaries, respectively ( $\partial\Omega_N \cap \partial\Omega_D = \emptyset$ ).

The compatibility and the equilibrium differential equations are given in  $\Omega$  respectively by Eq. (2.21) and by Eq. (2.42) that are here reported for reader's convenience (reference is made to the static case):

$$\mathbf{e} = \mathbf{D}\mathbf{u}, \quad (4.1)$$

$$\mathbf{u} = \begin{bmatrix} \mathbf{v} \\ \mathbf{w} \end{bmatrix}, \quad \mathbf{D} = \mathbf{I}_m \otimes \mathcal{L}, \quad \mathcal{L} = \begin{bmatrix} 1 & 0 \\ 0 & \partial z \\ \frac{1}{2}\partial z & \frac{1}{2} \\ \partial z & -1 \end{bmatrix},$$

or equivalently

$$\boldsymbol{\alpha} = \mathbf{v}, \quad \boldsymbol{\chi} = \partial_z \mathbf{w}, \quad \boldsymbol{\beta} = \frac{1}{2}(\partial_z \mathbf{v} + \mathbf{w}), \quad \boldsymbol{\gamma} = \partial_z \mathbf{v} - \mathbf{w}, \quad (4.2)$$

$$\mathbf{D}^* \mathbf{s} = \mathbf{q} \quad (4.3)$$

or equivalently

$$\mathbf{S} - \frac{1}{2} \partial_z \mathbf{T} - \partial_z \mathbf{V} = \mathbf{q}_v, \quad (4.4)$$

$$-\partial_z \mathbf{M} + \frac{1}{2} \mathbf{T} - \mathbf{V} = \mathbf{q}_w. \quad (4.5)$$

Moreover, the cross-section stiffness matrix accounts for the linear relationship between  $\mathbf{s}$  and  $\mathbf{e}$  in  $\Omega$ , that is the constitutive law of the beam model:

$$\mathbf{s} = \mathbf{C} \mathbf{e}. \quad (4.6)$$

The above field equations are completed by boundary conditions that can be of Dirichlet or of Neumann type and read as [47]:

$$\mathbf{u} = \bar{\mathbf{u}} \quad \text{on } \partial\Omega_D, \quad (4.7)$$

$$\mathbf{N}^T \mathbf{s} = \bar{\mathbf{t}} \quad \text{on } \partial\Omega_N, \quad (4.8)$$

where

$$\mathbf{N} = \mathbf{I}_m \otimes \mathbf{n}, \quad \mathbf{n} = \begin{bmatrix} 0 & 0 \\ 0 & n_z \\ \frac{1}{2}n_z & 0 \\ n_z & 0 \end{bmatrix}, \quad (4.9)$$

$n_z$  is the unit outward normal on the extreme bases and a superposed bar denotes a quantity assigned on the extreme bases. Expressing  $\mathbf{u}$  and  $\mathbf{s}$  in terms of their components, the boundary conditions (4.7) and (4.8) take the form:

$$\mathbf{v} = \bar{\mathbf{v}}, \quad \mathbf{w} = \bar{\mathbf{w}} \quad \text{on } \partial\Omega_D, \quad (4.10)$$

$$\frac{\mathbf{T}}{2} + \mathbf{V} = \pm \bar{\mathbf{Q}}, \quad \mathbf{M} = \pm \bar{\mathbf{W}} \quad \text{on } \partial\Omega_N. \quad (4.11)$$

## 4.2 Analytical solutions

Here, the analytical elastic solutions of some particular cases of the GBT problem described in Section 4.1 are presented. Firstly, the case of a cross-section with only the four classic modes is considered and, then, the attention is focused on higher-order modes. In the next section, the stresses associated to these analytical solutions are used as a base to construct the divergence-free stress assumption. Accordingly, no distributed loads are considered.

### 4.2.1 Classic modes

Consider the case of a cross-section with only four natural nodes and, hence, with only classic deformation modes. As anticipated in Section 2.3.5, in this case, in the modal space the present GBT formulation coincides with the classic Vlasov beam theory enriched with shear deformation. In particular, as shown in [47], generalized

displacements can be written as:

$$\mathbf{u}^c = \begin{bmatrix} \mathbf{v}^c \\ \mathbf{w}^c \end{bmatrix}, \quad \text{with} \quad \mathbf{v}^c = \begin{bmatrix} v_x \\ v_y \\ \vartheta_z \end{bmatrix}, \quad \mathbf{w}^c = \begin{bmatrix} v_z \\ \vartheta_y \\ -\vartheta_x \\ \omega_\phi \end{bmatrix}, \quad (4.12)$$

where superscript  $c$  serves to emphasize that generalized displacements and stresses are those of the classic beam theories. In the above expressions,  $v_x$ ,  $v_y$  and  $v_z$  are the displacements of the shear centre of the cross-section in the directions of the the principal inertia axes of the cross-section and of the  $z$ -axis, respectively,  $\vartheta_x$  and  $\vartheta_y$  are the cross-section rotations about the principal inertia axes,  $\vartheta_z$  is the in-plane cross-section rotation about the shear centre. Moreover,  $\omega_\phi$  is the sum of the rate of twist about the shear centre and of the torsional shear strain. Note that, as could be expected in a shear deformable beam, the cross-section rigid rotations about the principal inertia axes,  $\vartheta_x$  and  $\vartheta_y$ , are kinematic parameters independent from the transverse displacements of the shear centre along the principal inertia axes,  $v_x$  and  $v_y$ .

Combining Eqs. (2.21), (4.3), (4.6) and (4.12) is possible to write the beam equilibrium equations in terms of generalized displacements as:

$$-C_{M(1,1)} \partial_z^2 v_z(z) = 0, \quad (4.13)$$

$$-C_{V(2,2)} \partial_z^2 v_x(z) - C_{V(2,4)} \partial_z^2 \vartheta_z(z) + C_{V(2,2)} \partial_z \vartheta_y(z) + C_{V(2,4)} \partial_z \omega_\phi(z) = 0, \quad (4.14)$$

$$-C_{V(3,3)} \partial_z^2 v_y(z) - C_{V(3,4)} \partial_z^2 \vartheta_z(z) + C_{V(3,4)} \partial_z \omega_\phi(z) + C_{V(3,3)} \partial_z \vartheta_x(z) = 0, \quad (4.15)$$

$$\begin{aligned} -C_{V(2,4)} \partial_z^2 v_x(z) - C_{V(3,4)} \partial_z^2 v_y(z) + (-1/4 C_{T(4,4)} - C_{V(4,4)}) \partial_z^2 \vartheta_z(z) + \\ + (-1/4 C_{T(4,4)} + C_{V(4,4)}) \partial_z \omega_\phi(z) + \\ + C_{V(2,4)} \partial_z \vartheta_y(z) + C_{V(3,4)} \partial_z \vartheta_x(z) = 0, \end{aligned} \quad (4.16)$$

$$\begin{aligned} -C_{M(2,2)} \partial_z^2 \vartheta_y(z) - C_{V(2,2)} \partial_z v_x(z) - C_{V(2,4)} \partial_z \vartheta_z(z) + \\ + C_{V(2,2)} \vartheta_y(z) + C_{V(2,4)} \omega_\phi(z) = 0, \end{aligned} \quad (4.17)$$

$$\begin{aligned} -C_{M(3,3)} \partial_z^2 \vartheta_x(z) - C_{V(3,3)} \partial_z v_y(z) - C_{V(3,4)} \partial_z \vartheta_z(z) + \\ + C_{V(3,4)} \omega_\phi(z) + C_{V(3,3)} \vartheta_x(z) = 0, \end{aligned} \quad (4.18)$$

$$\begin{aligned} -C_{M(4,4)} \partial_z^2 \omega_\phi(z) - C_{V(2,4)} \partial_z v_x(z) - C_{V(3,4)} \partial_z v_y(z) + \\ + (1/4 C_{T(4,4)} - C_{V(4,4)}) \partial_z \vartheta_z(z) + \\ + C_{V(4,4)} \omega_\phi(z) + C_{V(3,4)} \vartheta_x(z) + 1/4 C_{T(4,4)} \omega_\phi(z) + C_{V(2,4)} \vartheta_y(z) = 0, \end{aligned} \quad (4.19)$$

where  $C_{\bullet(i,j)}$  denotes the component  $(i, j)$  of the submatrix  $\mathbf{C}_\bullet$  of the cross-section stiffness matrix. The solution of such system of differential equations can be written as:

$$\begin{aligned} v_x(z) = 1/6 c_3 z^3 + 1/2 c_4 z^2 + (c_7 a_1 + c_{13} a_2 + c_3 a_3 + c_5) z + c_6 + \\ + c_{11} a_4 e^{-fz} - c_{12} a_4 e^{fz}, \end{aligned} \quad (4.20)$$

$$\begin{aligned} v_y(z) = 1/6 c_7 z^3 + 1/2 c_8 z^2 - (c_7 a_5 - c_{13} a_6 - c_3 a_7 - c_9) z + c_{10} + \\ - c_{11} a_8 e^{-fz} + c_{12} a_8 e^{fz}, \end{aligned} \quad (4.21)$$

$$\begin{aligned} \vartheta_z(z) = c_{11} a_9 e^{-fz} - c_{12} a_9 e^{fz} - (c_7 a_{10} + c_{13} a_{11} + c_3 a_{12}) z + c_{14} \end{aligned} \quad (4.22)$$

$$v_z(z) = c_1 z + c_2, \quad (4.23)$$

$$\vartheta_y(z) = 1/2 c_3 z^2 + c_4 z + c_5, \quad (4.24)$$

$$\vartheta_x(z) = 1/2 c_7 z^2 + c_8 z + c_9, \quad (4.25)$$

$$\omega_\phi(z) = c_{11} e^{-fz} + c_{12} e^{fz} + c_{13}, \quad (4.26)$$

where  $f$  and  $a_i$ ,  $i = 1, \dots, 12$ , are constants depending on the coefficients of the cross-section stiffness matrix, while  $c_i$ ,  $i = 1, \dots, 14$ , are constants determined by the boundary conditions.

The expressions of coefficients of Eqs. (4.20)-(4.26) are:

$$f = 2 \sqrt{\frac{C_{T(4,4)} b_3}{C_{M(4,4)} b_2}} \quad (4.27)$$

$$a_1 = 4 \frac{C_{M(3,3)} C_{V(2,4)} C_{V(3,4)}}{C_{V(2,2)} b_1} \quad (4.28)$$

$$a_2 = 2 \frac{C_{T(4,4)} C_{V(2,4)}}{b_1} \quad (4.29)$$

$$a_3 = - \frac{C_{M(2,2)} \left( -4 C_{V(2,4)}^2 + b_1 \right)}{C_{V(2,2)} b_1} \quad (4.30)$$

$$a_4 = - C_{V(2,4)} \sqrt{\frac{C_{T(4,4)} C_{M(4,4)}}{b_2 b_3}} \quad (4.31)$$

$$a_5 = \frac{C_{M(3,3)} \left( -4 C_{V(3,4)}^2 + b_1 \right)}{C_{V(2,2)} b_1} \quad (4.32)$$

$$a_6 = 2 \frac{C_{T(4,4)} C_{V(3,4)}}{b_1} \quad (4.33)$$

$$a_7 = 4 \frac{C_{M(2,2)} C_{V(2,4)} C_{V(3,4)}}{C_{V(2,2)} b_1} \quad (4.34)$$

$$a_8 = C_{V(3,4)} \sqrt{\frac{C_{T(4,4)} C_{M(4,4)}}{b_2 b_3}} \quad (4.35)$$

$$a_9 = 1/2 \sqrt{\frac{C_{M(4,4)}}{C_{T(4,4)} b_2 b_3}} \left( -8 b_3 + b_2 \right) \quad (4.36)$$

$$a_{10} = 4 \frac{C_{M(3,3)} C_{V(3,4)}}{b_1} \quad (4.37)$$

$$a_{11} = \frac{8b_3 + b_1}{b_1} \quad (4.38)$$

$$a_{12} = 4 \frac{C_{M(2,2)} C_{V(2,4)}}{b_1}, \quad (4.39)$$

with

$$b_1 = C_{V(2,2)} C_{T(4,4)} - 4 C_{V(2,2)} C_{V(4,4)} + 4 C_{V(2,4)}^2 + 4 C_{V(3,4)}^2, \quad (4.40)$$

$$b_2 = C_{V(2,2)} C_{T(4,4)} + 4 C_{V(2,2)} C_{V(4,4)} - 4 C_{V(2,4)}^2 - 4 C_{V(3,4)}^2, \quad (4.41)$$

$$b_3 = C_{V(2,2)} C_{V(4,4)} - C_{V(2,4)}^2 - C_{V(3,4)}^2. \quad (4.42)$$

For later convenience, the above solution is rewritten as

$$\mathbf{u}^{cT} = \mathbf{P}_{pol_3}(z) \mathbf{c}_p + \mathbf{P}_{exp}(z) \mathbf{c}_e, \quad (4.43)$$

where

$$\mathbf{P}_{pol_3}(z) = \begin{bmatrix} z^3 & z^2 & z & 1 \end{bmatrix}, \quad \mathbf{P}_{exp}(z) = \begin{bmatrix} e^{-fz} & e^{fz} \end{bmatrix}, \quad (4.44)$$

and

$$\mathbf{c}_p = \begin{bmatrix} & -1/6 c_3 & & & -1/6 c_7 & & \dots \\ & -1/2 c_4 & & & -1/2 c_8 & & \dots \\ (-c_7 a_1 - c_{13} a_2 - c_3 a_3 - c_5) & & (c_7 a_5 - c_{13} a_6 - c_3 a_7 - c_9) & & & & \dots \\ & -c_6 & & & -c_{10} & & \dots \\ \dots & 0 & 0 & 0 & 0 & 0 & \dots \\ \dots & 0 & 0 & -1/2 c_3 & -1/2 c_7 & 0 & \dots \\ \dots & (c_7 a_{10} + c_{13} a_{11} + c_3 a_{12}) & -c_1 & -c_4 & -c_8 & 0 & \dots \\ \dots & -c_{14} & -c_2 & -c_5 & -c_9 & -c_{13} & \dots \end{bmatrix}, \quad (4.45)$$

$$\mathbf{c}_e = \begin{bmatrix} c_{11} a_4 & -c_{11} a_8 & c_{11} a_9 & 0 & 0 & 0 & c_{11} \\ -c_{12} a_4 & c_{12} a_8 & -c_{12} a_9 & 0 & 0 & 0 & c_{12} \end{bmatrix}. \quad (4.46)$$

Combining Eqs. (2.21), (4.6) and (4.43), the generalized stresses associated to the above displacement analytical solution can be easily derived.

### 4.2.2 Higher-order modes

Consider a cross-section with more than four natural nodes. In this case, higher-order deformation modes, involving section distortion, are present. Focus the attention on the generic higher-order mode  $k$  and denote by  $\mathbf{u}_k^h$  the vector collecting the generalized displacements associated to this mode:

$$\mathbf{u}_k^h = \begin{bmatrix} v_k \\ w_k \end{bmatrix}. \quad (4.47)$$

Following the same path outlined for classic modes, it can be easily verified that if the cross-section is doubly symmetric and if a mono-axial constitutive law is used for both the membrane and bending parts (i.e.  $\mathbb{C}^{(B)} = \mathbb{C}^{(M)}$ ), then the governing equations of the generic higher-order mode  $k$  are uncoupled from those of the other modes and read as:

$$\begin{aligned} & \left( -\frac{1}{4} C_{T(k,k)} - C_{V(k,k)} \right) \partial_z^2 v_k(z) + \\ & + \left( -\frac{1}{4} C_{T(k,k)} + C_{V(k,k)} \right) \partial_z w_k(z) + C_{S(k,k)} v_k(z) = 0, \end{aligned} \quad (4.48)$$

$$\begin{aligned} & -C_{M(k,k)} \partial_z^2 w_k(z) + \left( \frac{1}{4} C_{T(k,k)} - C_{V(k,k)} \right) \partial_z v_k(z) + \\ & + \left( \frac{1}{4} C_{T(k,k)} + C_{V(k,k)} \right) w_k(z) = 0. \end{aligned} \quad (4.49)$$

The solution of such system can be written as:

$$\begin{aligned} v_k(z) = & c_{k1}^h e^{-\alpha_{k1}^h z} \cos(\alpha_{k2}^h z) + c_{k2}^h e^{-\alpha_{k1}^h z} \sin(\alpha_{k2}^h z) + \\ & + c_{k3}^h e^{\alpha_{k1}^h z} \cos(\alpha_{k2}^h z) + c_{k4}^h e^{\alpha_{k1}^h z} \sin(\alpha_{k2}^h z), \end{aligned} \quad (4.50)$$

$$\begin{aligned} w_k(z) = & e^{-\alpha_{k1}^h z} \cos(\alpha_{k2}^h z) (-\alpha_{k1}^h c_{k1}^h + \alpha_{k2}^h c_{k2}^h) + \\ & + e^{-\alpha_{k1}^h z} \sin(\alpha_{k2}^h z) (-\alpha_{k1}^h c_{k2}^h - \alpha_{k2}^h c_{k1}^h) + \\ & + e^{\alpha_{k1}^h z} \cos(\alpha_{k2}^h z) (\alpha_{k1}^h c_{k3}^h + \alpha_{k2}^h c_{k4}^h) + \\ & + e^{\alpha_{k1}^h z} \sin(\alpha_{k2}^h z) (\alpha_{k1}^h c_{k4}^h - \alpha_{k2}^h c_{k3}^h), \end{aligned} \quad (4.51)$$

where  $\alpha_{k1}^h$  and  $\alpha_{k2}^h$  are constants depending on the coefficients of the cross-section stiffness matrix, while  $c_{ki}^h$ ,  $i = 1, \dots, 4$ , are constants determined by the boundary conditions.

The expressions of coefficients of Eqs. (4.50)-(4.51) are:

$$\alpha_{k1}^h = \operatorname{Re}(f^h), \quad \alpha_{k2}^h = \operatorname{Im}(f^h), \quad (4.52)$$

$$f^h = 1/2 \frac{\sqrt{-2 b_{k1}^h \left( b_{k2}^h + \sqrt{(b_{k2}^h)^2 - 4 b_{k1}^h b_{k3}^h} \right)}}{b_{k1}^h}, \quad (4.53)$$

with

$$b_{k1}^h = -1/4 C_{T(k,k)} - C_{V(k,k)}, \quad (4.54)$$

$$b_{k2}^h = \frac{C_{S(k,k)} C_{M(k,k)} + C_{T(k,k)} C_{V(k,k)}}{\hat{C}_{M(k,k)}}, \quad (4.55)$$

$$b_{k3}^h = -1/4 \frac{C_{S(k,k)} (C_{T(k,k)} + 4 C_{V(k,k)})}{C_{M(k,k)}}. \quad (4.56)$$

For later convenience, the above solution is rewritten as

$$\mathbf{u}_k^{h\text{T}}(z) = \mathbf{Q}_k(z) \mathbf{c}_k^h, \quad (4.57)$$

where

$$\mathbf{Q}_k(z) = \begin{bmatrix} e^{-\alpha_{k1}^h z} \cos(\alpha_{k2}^h z) & e^{-\alpha_{k1}^h z} \sin(\alpha_{k2}^h z) & e^{\alpha_{k1}^h z} \cos(\alpha_{k2}^h z) & e^{\alpha_{k1}^h z} \sin(\alpha_{k2}^h z) \end{bmatrix},$$

and

$$\mathbf{c}_k^h = \begin{bmatrix} c_{k1}^h & (-c_{k1}^h \alpha_{k1}^h + c_{k2}^h \alpha_{k2}^h) \\ c_{k2}^h & (-c_{k2}^h \alpha_{k1}^h - c_{k1}^h \alpha_{k2}^h) \\ c_{k3}^h & (c_{k3}^h \alpha_{k1}^h + c_{k4}^h \alpha_{k2}^h) \\ c_{k4}^h & (c_{k4}^h \alpha_{k1}^h + c_{k3}^h \alpha_{k2}^h) \end{bmatrix}. \quad (4.58)$$

Analogously to the case of the classic modes, the generalized stresses associated to this analytical solution can be easily derived by combining Eqs. (2.21), (4.6) and (4.57).

### 4.3 Flexibility-based GBT finite element

In this section, the attention is focused on constructing the 2-node flexibility-based GBT finite element. In particular, the variational

framework, the representation assumed for generalized stresses, the finite element equations and the a posteriori recovery of the generalized displacements along the beam axis are presented.

### 4.3.1 Variational framework

The domain  $\Omega$  is partitioned in  $n_e$  subdomains  $\Omega_e \subset \Omega$ , such that  $\cup_{e=1}^{n_e} \Omega_e = \Omega$ . The flexibility-based finite element can be constructed on the basis of the total complementary energy functional

$$\Pi_C = \sum_{e=1}^{n_e} \Pi_{C,e}, \quad (4.59)$$

$$\Pi_{C,e} = -\frac{1}{2} \int_{\Omega_e} \mathbf{s}^T \mathbf{C}^{-1} \mathbf{s} \, d\Omega + \bar{\mathbf{u}}^T (\mathbf{N}^T \mathbf{s})|_{(\partial\Omega_D)_e}, \quad (4.60)$$

defined over the set of generalized stresses fulfilling a priori equilibrium equations (4.4), (4.5), (4.11) and inter-element equilibrium conditions. It can be easily verified that the stationary conditions of  $\Pi_C$  are the compatibility equations, Eqs. (2.21) and (4.10). If the inter-element equilibrium conditions and Neumann boundary conditions are relaxed, then  $\Pi_C$  transforms in the following hybrid complementary energy functional:

$$\Pi_{HY} = \sum_{e=1}^{n_e} \Pi_{C,e} + \sum_{i=1}^{\rho_{int}} \mathbf{u}|_{\partial\Omega_i}^T \llbracket \mathbf{N}^T \mathbf{s} \rrbracket_{\partial\Omega_i}, \quad (4.61)$$

where  $\rho_{int}$  is the number of inter-element and Neumann boundaries,  $\partial\Omega_i$  is the  $i$ -th inter-element boundary and  $\llbracket \bullet \rrbracket$  denotes the jump of  $\bullet$  on  $\partial\Omega_i$ . The stationary conditions of the hybrid complementary energy functional are Eqs. (2.21), (4.10), (4.11) and, in addition, the inter-element equilibrium conditions on  $\partial\Omega_i$ . Note

that in functional  $\Pi_{HY}$  displacement is defined only on the elements boundary (at the nodes) where it acts as a Lagrangian multiplier to enforce the Neumann boundary conditions and the inter-element equilibrium conditions.

### 4.3.2 Assumed stresses

In this section, a strategy to select the generalized stresses approximation in a rational way is presented. Stresses are approximated independently on each element and should satisfy the equilibrium equations pointwise within each element.

Consider a generic cross-section and write the generalized stresses vector as:

$$\mathbf{s} = \begin{bmatrix} \mathbf{s}^c \\ \mathbf{s}^h \end{bmatrix}, \quad (4.62)$$

where  $\mathbf{s}^c$  collects the generalized stresses associated to the first four modes (classic modes) and  $\mathbf{s}^h$  those associated to the  $m_h$  higher-order modes. In particular, as shown in [47],  $\mathbf{s}^c$  collects the generalized stresses of the classic Vlasov beam theory enriched with shear deformation and can be written as:

$$\mathbf{s}^c = \begin{bmatrix} \mathbf{s}^{cb} \\ \mathbf{s}^{ct} \end{bmatrix}, \quad \text{with} \quad \mathbf{s}^{cb} = \begin{bmatrix} N \\ M_y \\ M_x \\ V_x \\ V_y \end{bmatrix}, \quad \mathbf{s}^{ct} = \begin{bmatrix} B \\ T \\ V_\phi \end{bmatrix}, \quad (4.63)$$

being  $N$  the axial force,  $M_x$  and  $M_y$  the bending moments about

the principal inertia axes of the cross-section,  $V_x$  and  $V_y$  the shearing forces in the directions of the principal inertia axes,  $B$  the bi-moment *à la* Vlasov,  $T$  the St. Venant torsion and  $V_\phi$  the warping torsion. Moreover,  $\mathbf{s}^h$  can be written as

$$\mathbf{s}^h = \begin{bmatrix} \mathbf{s}_1^h \\ \vdots \\ \mathbf{s}_k^h \\ \vdots \\ \mathbf{s}_{m_h}^h \end{bmatrix} \quad \text{with} \quad \mathbf{s}_k^h = \begin{bmatrix} S_k \\ M_k \\ T_k \\ V_k \end{bmatrix}, \quad (4.64)$$

i.e.  $\mathbf{s}_k^h$  is the vector collecting the generalized stresses associated to the higher-order mode  $k$ .

As usually done in developing hybrid-stress models [102, 103], the element stresses approximation is initially assumed as an appropriate uncoupled expansion and, then, is constrained to satisfy equilibrium equations. Therefore, the generalized stresses are initially assumed as the following uncoupled expansion based on the stresses associated to the analytical solutions developed in the pre-

vious section:

$$\begin{bmatrix} \mathbf{s}^{cb} \\ \mathbf{s}^{ct} \\ \mathbf{s}_1^h \\ \vdots \\ \mathbf{s}_k^h \\ \vdots \\ \mathbf{s}_{m_h}^h \end{bmatrix} = \begin{bmatrix} \mathbf{P}^{cb} & \mathbf{0} & \mathbf{0} & \cdots & \mathbf{0} & \cdots & \mathbf{0} \\ \mathbf{0} & \mathbf{P}^{ct} & \mathbf{0} & \cdots & \mathbf{0} & \cdots & \mathbf{0} \\ \mathbf{0} & \mathbf{0} & \mathbf{P}_1^h & \cdots & \mathbf{0} & \cdots & \mathbf{0} \\ \vdots & \vdots & \vdots & \ddots & \vdots & \ddots & \vdots \\ \mathbf{0} & \mathbf{0} & \mathbf{0} & \cdots & \mathbf{P}_k^h & \cdots & \mathbf{0} \\ \vdots & \vdots & \vdots & \ddots & \vdots & \ddots & \vdots \\ \mathbf{0} & \mathbf{0} & \mathbf{0} & \cdots & \mathbf{0} & \cdots & \mathbf{P}_{m_h}^h \end{bmatrix} \begin{bmatrix} \beta^{cb} \\ \beta^{ct} \\ \beta_1^h \\ \vdots \\ \beta_k^h \\ \vdots \\ \beta_{m_h}^h \end{bmatrix}, \quad (4.65)$$

where

$$\mathbf{P}^{cb} = \mathbf{I}_5 \otimes \mathbf{P}_{pol_2}, \quad (4.66)$$

$$\mathbf{P}^{ct} = \mathbf{I}_3 \otimes \left[ \mathbf{P}_{pol_2} \quad \mathbf{P}_{exp} \mid \mathbf{Q}_1 \quad \cdots \quad \mathbf{Q}_k \quad \cdots \quad \mathbf{Q}_{m_h} \right], \quad (4.67)$$

$$\mathbf{P}_k^h = \mathbf{I}_4 \otimes \left[ \mathbf{P}_{pol_2} \quad \mathbf{P}_{exp} \mid \mathbf{Q}_1 \quad \cdots \quad \mathbf{Q}_k \quad \cdots \quad \mathbf{Q}_{m_h} \right], \quad (4.68)$$

with

$$\mathbf{P}_{pol_2} = \begin{bmatrix} z^2 & z & 1 \end{bmatrix}, \quad (4.69)$$

and  $\beta^{cb}$ ,  $\beta^{ct}$  and  $\beta_k^h$  are the parameters, local to each element, governing axial-bending, torsional and higher-order modes, respectively. The next step is to constrain the initially assumed stresses, Eq. (4.65), in order to satisfy the equilibrium equations pointwise. Enforcing equilibrium (it is done in the absence of body forces) partially couples the stress approximation (4.65), so reducing the stress parameters. The resulting expressions for  $\mathbf{P}^{cb}$ ,  $\mathbf{P}^{ct}$  and  $\mathbf{P}_k^h$  are:

- Classic generalized stresses:

$$\mathbf{P}^{cb} = \begin{bmatrix} 1 & 0 & 0 & 0 & 0 \\ 0 & 1 & -z & 0 & 0 \\ 0 & 0 & 0 & 1 & -z \\ 0 & 0 & 1 & 0 & 0 \\ 0 & 0 & 0 & 0 & 1 \end{bmatrix}, \quad (4.70)$$

$$\mathbf{P}^{ct} = \left[ \mathbf{P}_{pol}^{ct} \quad \mathbf{P}_{exp}^{ct} \mid \mathbf{Q}_1^{ct} \quad \dots \quad \mathbf{Q}_k^{ct} \quad \dots \quad \mathbf{Q}_{n_h}^{ct} \right], \quad (4.71)$$

with

$$\mathbf{P}_{pol}^{ct} = \begin{bmatrix} 1 & 1/2 z & -z & -z^2 \\ 0 & 1 & 0 & -2z \\ 0 & 0 & 1 & z \end{bmatrix}, \quad \mathbf{P}_{exp}^{ct} = \begin{bmatrix} -2 \frac{e^{fz}}{f} & 2 \frac{e^{-fz}}{f} \\ -2 \frac{e^{fz}}{f} & -2 \frac{e^{-fz}}{f} \\ e^{fz} & e^{-fz} \end{bmatrix}. \quad (4.72)$$

$$\mathbf{Q}_k^{ct} = \begin{bmatrix} m_{k1}^h & m_{k2}^h & \dots \\ -\alpha_{k1}^h m_{k1}^h - \alpha_{k2}^h m_{k2}^h & -\alpha_{k1}^h m_{k2}^h + \alpha_{k2}^h m_{k1}^h & \dots \\ 1/2 \alpha_{k1}^h m_{k1}^h + 1/2 \alpha_{k2}^h m_{k2}^h & 1/2 \alpha_{k1}^h m_{k2}^h - 1/2 \alpha_{k2}^h m_{k1}^h & \dots \\ \dots & m_{k3}^h & m_{k4}^h \\ \dots & \alpha_{k1}^h m_{k3}^h - \alpha_{k2}^h m_{k4}^h & \alpha_{k1}^h m_{k4}^h + \alpha_{k2}^h m_{k3}^h \\ \dots & 1/2 \alpha_{k2}^h m_{k4}^h - 1/2 \alpha_{k1}^h m_{k3}^h & -1/2 \alpha_{k2}^h m_{k3}^h - 1/2 \alpha_{k1}^h m_{k4}^h \end{bmatrix}. \quad (4.73)$$

- Higher-order generalized stresses associated to mode  $k$ :

$$\mathbf{P}_k^h = \left[ \mathbf{P}_{pol}^h \quad \mathbf{P}_{exp}^h \mid \mathbf{Q}_1^h \quad \dots \quad \mathbf{Q}_k^h \quad \dots \quad \mathbf{Q}_{n_h}^h \right], \quad (4.74)$$

with

$$\mathbf{P}_{pol}^h = \begin{bmatrix} 0 & 0 & 1/2 & 0 & 1 \\ 1 & 1/2 z & 1/4 z^2 & -z & -1/2 z^2 \\ 0 & 1 & z & 0 & 0 \\ 0 & 0 & 0 & 1 & z \end{bmatrix}, \quad (4.75)$$

$$\mathbf{P}_{exp}^h = \begin{bmatrix} 1/2 f e^{fz} & -1/2 f e^{-fz} & f e^{fz} & -f e^{-fz} \\ 1/2 \frac{e^{fz}}{f} & -1/2 \frac{e^{-fz}}{f} & -\frac{e^{fz}}{f} & \frac{e^{-fz}}{f} \\ e^{fz} & e^{-fz} & 0 & 0 \\ 0 & 0 & e^{fz} & e^{-fz} \end{bmatrix}, \quad (4.76)$$

$$\mathbf{Q}_k^h = \begin{bmatrix} -1/2 \alpha_{k1}^h m_{k1}^h - 1/2 \alpha_{k2}^h m_{k2}^h & -1/2 \alpha_{k1}^h m_{k2}^h + 1/2 \alpha_{k2}^h m_{k1}^h & \dots \\ -1/2 \frac{\alpha_{k1}^h m_{k1}^h - \alpha_{k2}^h m_{k2}^h}{\alpha_{k1}^h + \alpha_{k2}^h} & -1/2 \frac{\alpha_{k1}^h m_{k2}^h + \alpha_{k2}^h m_{k1}^h}{\alpha_{k1}^h + \alpha_{k2}^h} & \dots \\ m_{k1}^h & m_{k2}^h & \dots \\ 0 & 0 & \dots \\ \dots & 1/2 \alpha_{k1}^h m_{k3}^h - 1/2 \alpha_{k2}^h m_{k4}^h & 1/2 \alpha_{k1}^h m_{k4}^h + 1/2 \alpha_{k2}^h m_{k3}^h & \dots \\ \dots & 1/2 \frac{\alpha_{k1}^h m_{k3}^h + \alpha_{k2}^h m_{k4}^h}{\alpha_{k1}^h + \alpha_{k2}^h} & 1/2 \frac{\alpha_{k1}^h m_{k4}^h - \alpha_{k2}^h m_{k3}^h}{\alpha_{k1}^h + \alpha_{k2}^h} & \dots \\ \dots & m_{k3}^h & m_{k4}^h & \dots \\ \dots & 0 & 0 & \dots \\ \dots & -\alpha_{k1}^h m_{k1}^h - \alpha_{k2}^h m_{k2}^h & -\alpha_{k1}^h m_{k2}^h + \alpha_{k2}^h m_{k1}^h & \dots \\ \dots & \frac{\alpha_{k1}^h m_{k1}^h - \alpha_{k2}^h m_{k2}^h}{\alpha_{k1}^h + \alpha_{k2}^h} & \frac{\alpha_{k1}^h m_{k2}^h + \alpha_{k2}^h m_{k1}^h}{\alpha_{k1}^h + \alpha_{k2}^h} & \dots \\ \dots & 0 & 0 & \dots \\ \dots & m_{k1}^h & m_{k2}^h & \dots \\ \dots & \alpha_{k1}^h m_{k3}^h - \alpha_{k2}^h m_{k4}^h & \alpha_{k1}^h m_{k4}^h + \alpha_{k2}^h m_{k3}^h & \dots \\ \dots & -\frac{\alpha_{k1}^h m_{k3}^h + \alpha_{k2}^h m_{k4}^h}{\alpha_{k1}^h + \alpha_{k2}^h} & -\frac{\alpha_{k1}^h m_{k4}^h - \alpha_{k2}^h m_{k3}^h}{\alpha_{k1}^h + \alpha_{k2}^h} & \dots \\ \dots & 0 & 0 & \dots \\ \dots & m_{k3}^h & m_{k4}^h & \dots \end{bmatrix}, \quad (4.77)$$

$$\begin{aligned} m_{k1}^h &= e^{-\alpha_{k1}^h z} \cos(\alpha_{k2}^h z), & m_{k2}^h &= e^{-\alpha_{k1}^h z} \sin(\alpha_{k2}^h z), \\ m_{k3}^h &= e^{\alpha_{k1}^h z} \cos(\alpha_{k2}^h z), & m_{k4}^h &= e^{\alpha_{k1}^h z} \sin(\alpha_{k2}^h z). \end{aligned} \quad (4.78)$$

For further convenience, the resultant stress approximation is put in the compact form

$$\mathbf{s} = \mathbf{P}\beta. \quad (4.79)$$

To take into account for the presence of body forces, a particular solution of the equilibrium equations is added to the final stress approximation, as usually done in hybrid stress models [104]. The resulting expression reads as

$$\mathbf{s} = \mathbf{P}\beta + \mathbf{s}_p. \quad (4.80)$$

### 4.3.3 Finite element equations

Here, basing on the hybrid complementary formulation and the stress assumptions made in the previous section, the finite element equations are derived. Introducing the assumed stresses into the hybrid complementary energy functional (4.61) referred to the single element between nodes  $i$  and  $j$ , and making it stationary yield the following discrete element equations:

$$\begin{bmatrix} -\mathbf{H} & \mathbf{G}^T \\ \mathbf{G} & \mathbf{0} \end{bmatrix} \begin{bmatrix} \beta \\ \mathbf{q} \end{bmatrix} = \begin{bmatrix} \mathbf{g} \\ \mathbf{h} \end{bmatrix}, \quad (4.81)$$

where  $\mathbf{q}^T = \begin{bmatrix} \mathbf{u}_i^T & \mathbf{u}_j^T \end{bmatrix}$ , being  $\mathbf{u}_i$  and  $\mathbf{u}_j$  the vectors of generalized displacements associated respectively with element nodes  $i$  and  $j$ ,  $\beta^T = \begin{bmatrix} \beta^{cbT} & \beta^{ctT} & \beta_k^{hT} \end{bmatrix}$ ,  $\mathbf{h}$  and  $\mathbf{g}$  are the terms due to the prescribed loads and  $\mathbf{H}$  and  $\mathbf{G}$  are, respectively, the element flexibility and the element equilibrium matrices.

Parameters  $\beta$  can be condensed out and the following elemental equations involving only nodal generalized displacements are obtained:

$$\mathbf{K}\mathbf{q} = \mathbf{f}. \quad (4.82)$$

The definitions of matrices and vectors in Eqs. (4.81) and (4.82) for the generic element between nodes  $i$  and  $j$  are:

$$\mathbf{H} = \int_{\Omega_e} \mathbf{P}^T \mathbf{C}^{-1} \mathbf{P} \, d\Omega, \quad \mathbf{G} = \begin{bmatrix} (\mathbf{N}^T \mathbf{P})|_i \\ (\mathbf{N}^T \mathbf{P})|_j \end{bmatrix}, \quad (4.83)$$

$$\mathbf{g} = \int_{\Omega_e} \mathbf{P}^T \mathbf{C}^{-1} \mathbf{s}_p \, d\Omega, \quad \mathbf{h} = \begin{bmatrix} (\mathbf{N}^T \mathbf{s}_p)|_i \\ (\mathbf{N}^T \mathbf{s}_p)|_j \end{bmatrix}, \quad (4.84)$$

$$\mathbf{K} = \mathbf{G}\mathbf{H}^{-1}\mathbf{G}^T, \quad \mathbf{f} = \mathbf{h} + \mathbf{G}\mathbf{H}^{-1}\mathbf{g}. \quad (4.85)$$

As it can be observed, the elemental equations (4.82) are in the standard format of assumed displacement finite elements. Therefore, the present element can be easily implemented into existing finite element codes.

#### 4.3.4 Recovery of the generalized displacements along beam axis

The hybrid complementary formulation does not require any assumption regarding the representation of the generalized displacements, since only their nodal values are involved. However, the accurate evaluation of the displacements in the interior of the element is often of importance. Indeed, the analytical solution functions derived in Section 4.2 can be easily used for this scope. In fact,

starting from Eqs. (4.20)-(4.26) for classic modes and from Eqs. (4.50), (4.51) for higher-order modes and imposing suitable boundary conditions (i.e. the typical boundary conditions associated to shape functions: one generalized displacement equal to 1 and all the others equal to 0), it is possible to derive shape functions by which interpolate the nodal values, so obtaining the displacement recovery along the beam axis.

## 4.4 Numerical tests

In this section, the performance of the described flexibility-based GBT finite element, hereinafter called GF, are numerically verified on some test problems and compared with that of a standard assumed displacement (compatible) GBT finite element, hereinafter called GC. Moreover, for further comparison, the numerical results in terms of displacements and strain energy predicted, on very fine meshes, by shell finite element models solved with the finite element solver Code\_Aster [101] are also included. Both GF and GC elements are implemented in the CAPS finite element code. In element GC,  $\mathbf{v}$ - and  $\mathbf{w}$ -parameters are approximated, respectively, by cubic and quadratic Lagrangian shape functions, and the degrees of freedom related to internal nodes are condensed out at the element level. On the same mesh, the computational cost of GC and GF elements is comparable, with the element GF being slightly more expensive (the difference in CPU time is about 15%). However, the better accuracy of the GF element offsets in general the

computational burden, as it is shown in the numerical tests that follow. In all the tests,  $E = 2.1 \times 10^5$  MPa and  $\nu = 0.3$  are assumed and the reference solutions are obtained using GC elements on very fine meshes. Moreover, as already stated, only fundamental flexural-shear modes based on natural nodes are used.

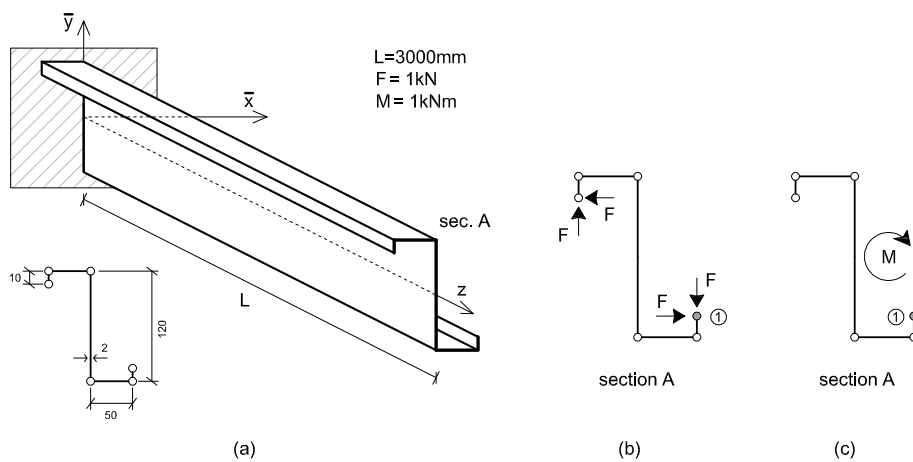


Figure 4.1: Z-section cantilever beam: (a) geometry; (b) self-equilibrated load; (c) torsional load.

#### 4.4.1 Z-section cantilever beam

A lipped Z-section (6 natural nodes) cantilever beam subjected to tip load is considered, see Fig. 4.1a. The cross-section deformation modes are shown in Fig. 4.2. Two load cases are studied: self-equilibrated load (Fig. 4.1b) and torsion (Fig. 4.1c). As regards the self-equilibrated load, Figure 4.3 shows the beam deformed shapes

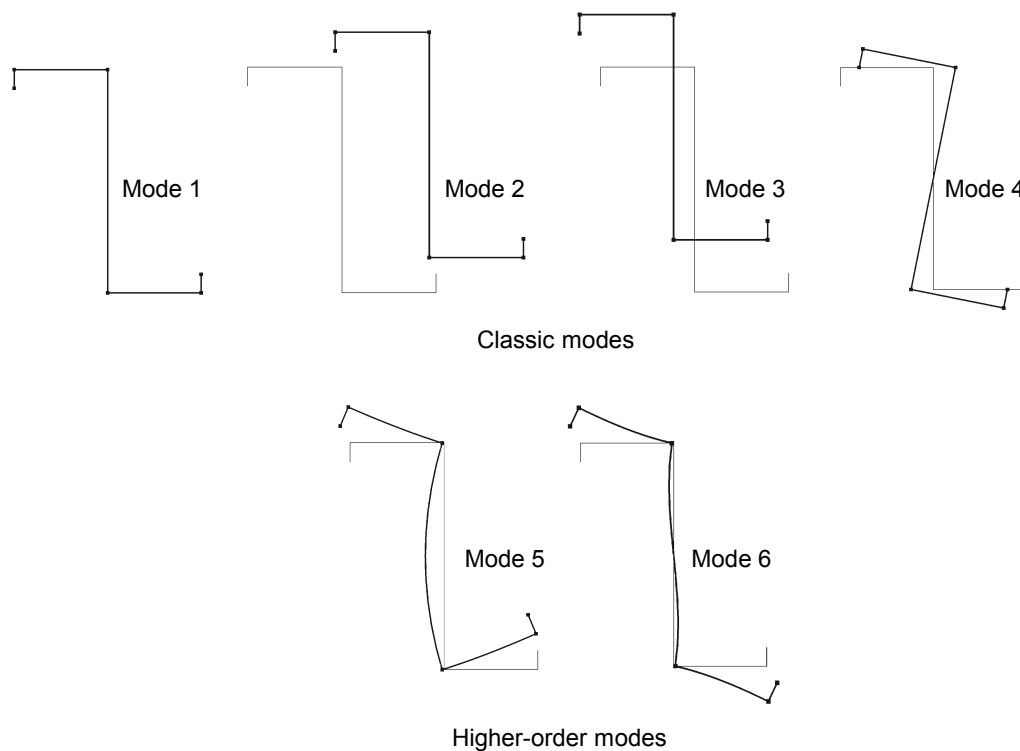


Figure 4.2: Z-section cantilever beam: in-plane configurations of cross-section deformation modes.

obtained using the proposed GF-element and the GC-element on a one-element mesh, together with the reference solution. As it can be noted, the proposed element captures very well the deformed shape even if only one finite element is used. On the contrary, the beam deformation near the loaded section is not accurately predicted by the GC-element. These observations are confirmed by Fig. 4.4, where the  $\bar{y}$ -displacement of natural node 1 of the cross-section (see Fig. 4.1b) along the beam axis is shown: the solution predicted by the proposed element accurately matches the reference solution all over the axis using only one finite element, while this does not happen with the GC-element even if two finite elements are used. The high accuracy of the proposed element is confirmed also

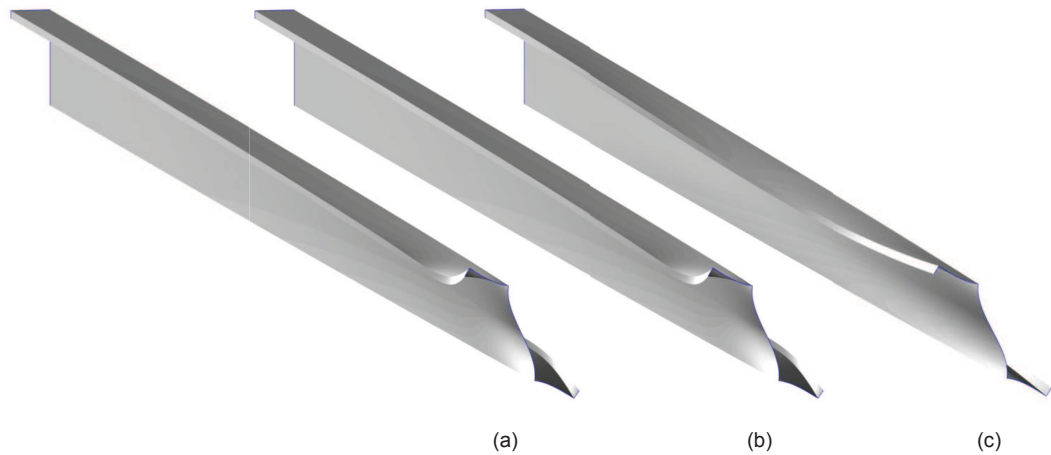


Figure 4.3: Z-section cantilever beam with self-equilibrated load - Deformed shape: (a) reference solution; (b) GF-element (1 finite element); (c) GC-element (1 finite element).

by Table 4.1, collecting the  $\bar{x}$ - and  $\bar{y}$ -displacement of natural node 1 of the end section (section A) and the strain energy of the beam, obtained by the various models. Figures 4.5 and 4.6 show the non-null components of the generalized stresses along the beam axis. In particular, the classic generalized stresses are shown in Fig. 4.5 and the higher-order ones in Fig. 4.6. Moreover, the generalized stresses at section A are collected in Table 4.2. The very good performance of the proposed element also in terms of stresses can be observed: all the stress components are predicted with high accuracy using only one finite element. It is worth to note that, with the GC-element, two finite elements (having a computational cost that is about the double of that of the one GF finite element mesh) do not suffice to obtain a comparable accuracy. As regards the second load case, that is the torsion load, the non-null generalized stresses are shown in Figs. 4.7 and 4.8 and in Table 4.3. The excellent

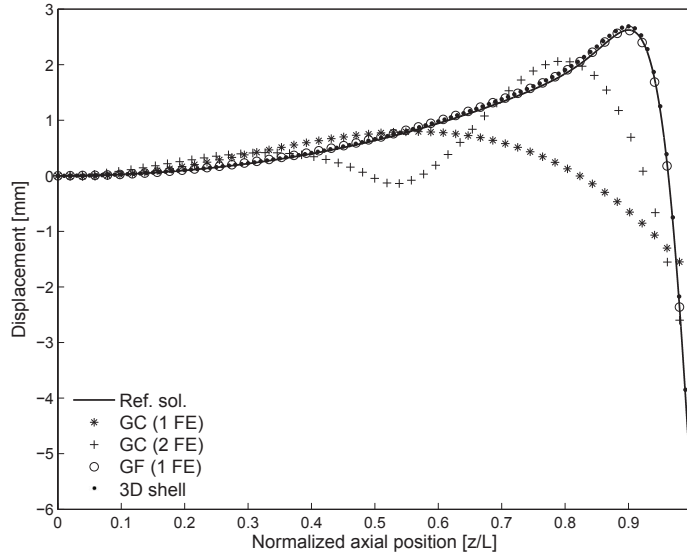


Figure 4.4: Z-section cantilever beam with self-equilibrated load:  $\bar{y}$ -displacement of natural node 1.

Table 4.1: Z-section cantilever beam with self-equilibrated load.  $\bar{x}$ - and  $\bar{y}$ -displacement of natural node 1 at  $z/L = 1$  and strain energy  $\Phi$  of the beam.

	GF (1 FE)	GC (1 FE)	GC (2 FE)	3D shell	Ref. sol.
$\bar{x}$ -displ. [mm]	5.763	1.920	3.799	6.312	5.763
$\bar{y}$ -displ. [mm]	-5.841	-1.817	-3.809	-5.713	-5.841
$\Phi$ [Nmm]	$1.160 \cdot 10^4$	$0.737 \cdot 10^4$	$0.761 \cdot 10^4$	$1.203 \cdot 10^4$	$1.160 \cdot 10^4$

performance of the proposed element can be observed.

#### 4.4.2 Clamped-clamped rack-section beam

Consider the clamped-clamped beam shown in Fig. 4.9a. The cross-section, typical of rack systems, has 15 natural nodes and its deformation modes are shown in Fig. 4.10. The beam is subjected to two point forces applied on the intermediate section A (Fig. 4.9b). Figure 4.11 shows the deformed shape of the beam

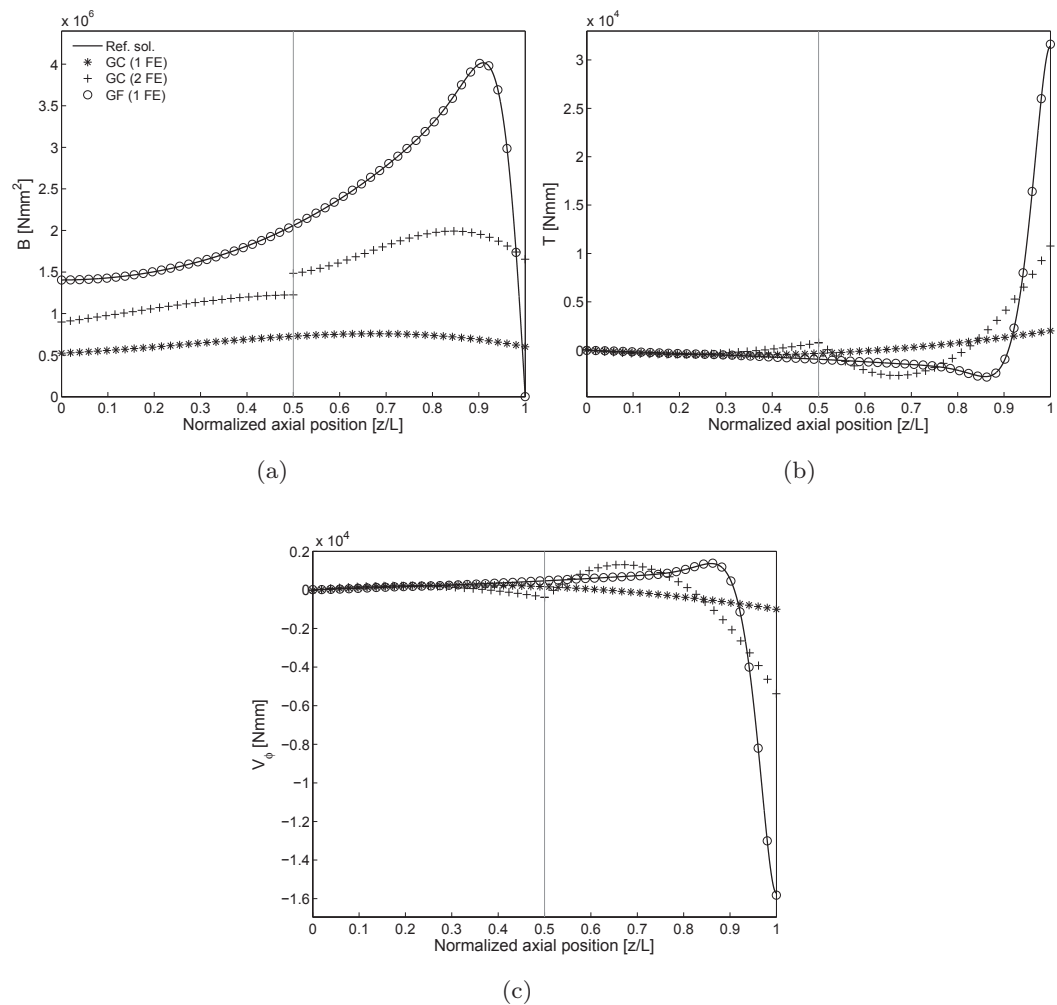


Figure 4.5: Z-section cantilever beam with self-equilibrated load - Classic generalized stresses: (a)  $B$ ; (b)  $T$ ; (c)  $V_\phi$ .

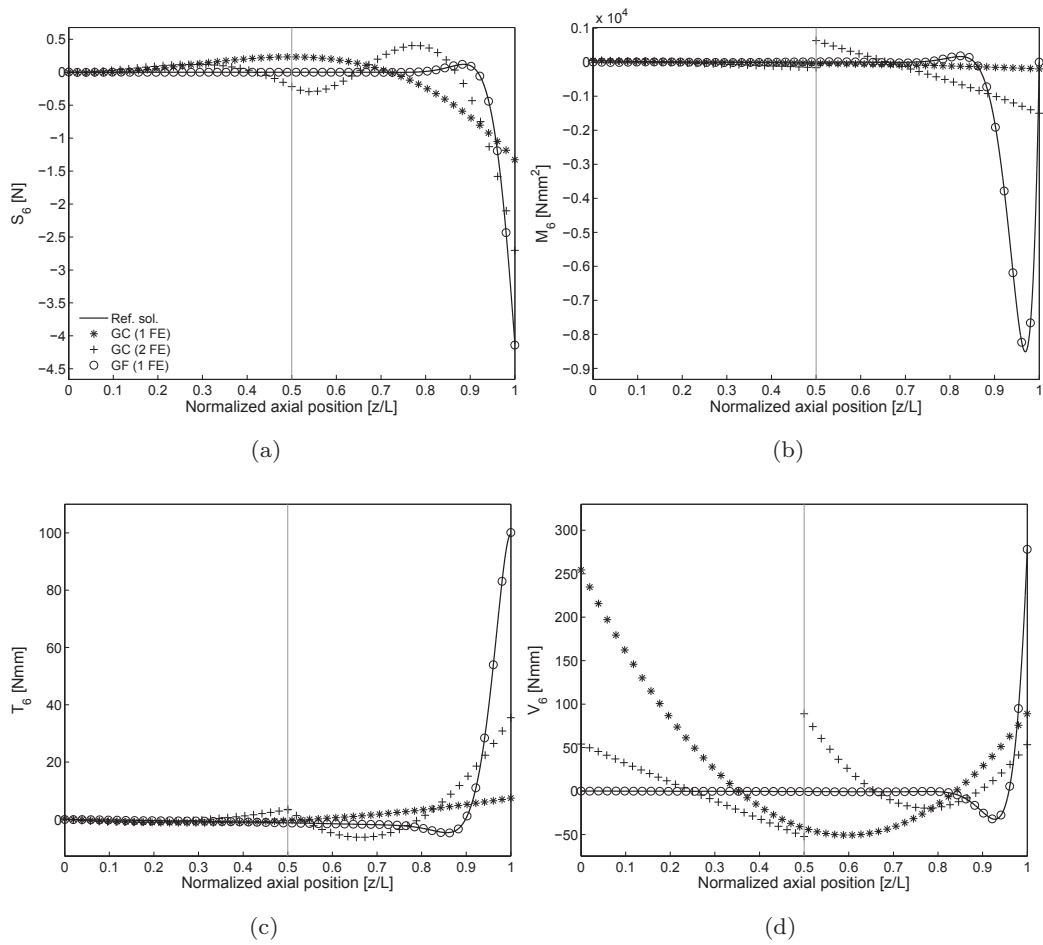


Figure 4.6: Z-section cantilever beam with self-equilibrated load - Higher-order generalized stresses associated to mode 6: (a)  $S_6$ ; (b)  $M_6$ ; (c)  $T_6$ ; (d)  $V_6$ .

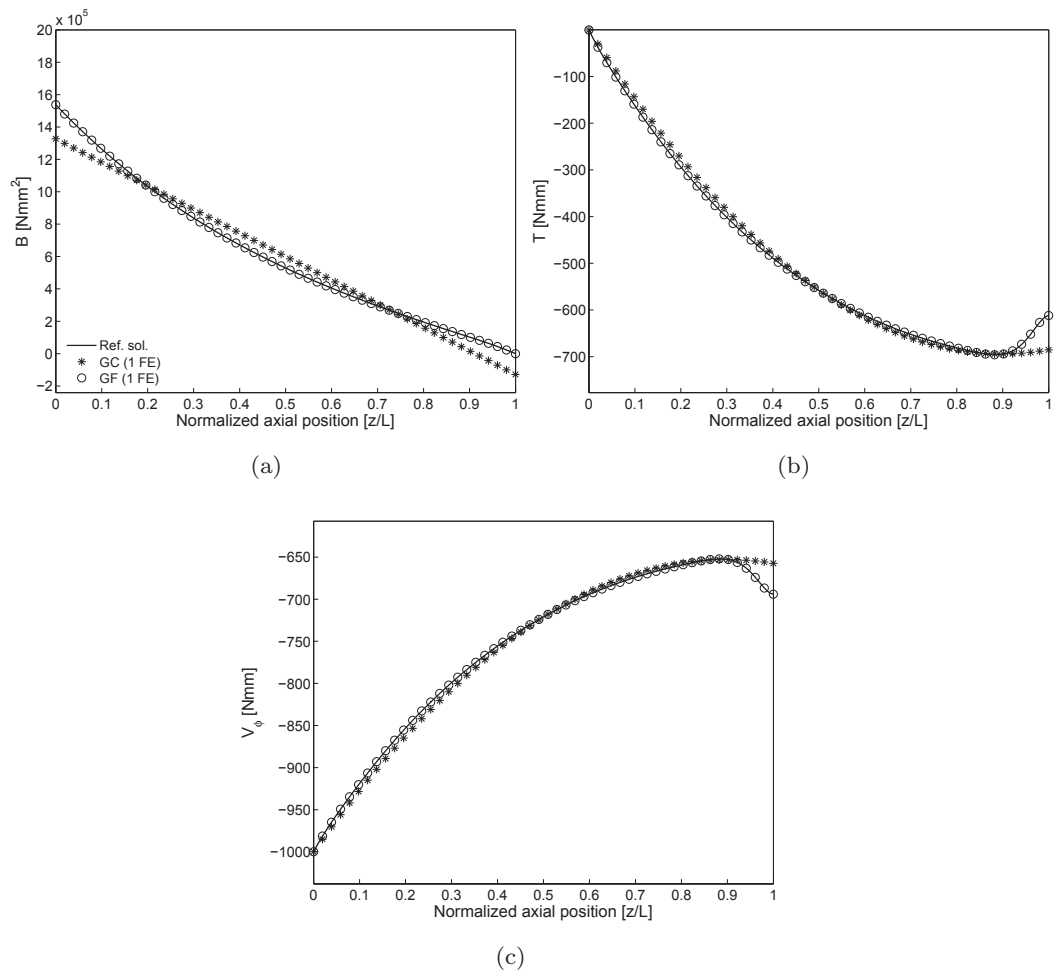


Figure 4.7: Z-section cantilever beam with torsional load - Classic generalized stresses: (a)  $B$ ; (b)  $T$ ; (c)  $V_\phi$ .

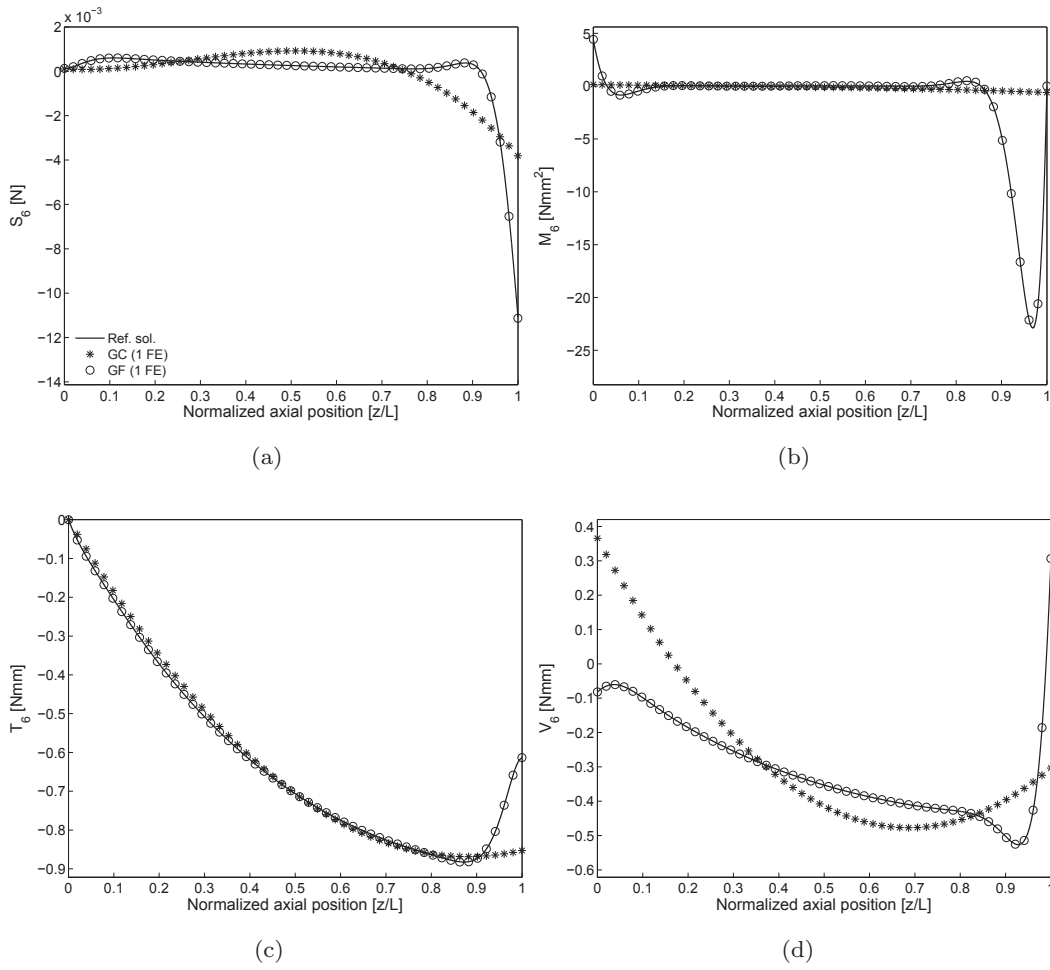


Figure 4.8: Z-section cantilever beam with torsional load - Higher-order generalized stresses associated to mode 6: (a)  $S_6$ ; (b)  $M_6$ ; (c)  $T_6$ ; (d)  $V_6$ .

Table 4.2: Z-section cantilever beam with self-equilibrated load. Generalized stresses at  $z/L = 1$ .

		GF (1 FE)	GC (1 FE)	GC (2 FE)	Ref. sol.
$B$	[Nmm <sup>2</sup> ]	0	$6.006 \cdot 10^5$	$16.535 \cdot 10^5$	0
$T$	[Nmm]	31631.927	2002.711	10767.655	31418.327
$V_\phi$	[Nmm]	-15816.963	-1001.355	-5383.828	-15709.163
$S_6$	[N]	-4.140	-1.327	-2.702	-4.120
$M_6$	[Nmm <sup>2</sup> ]	0	-195.886	-1501.724	0
$T_6$	[Nmm]	100.106	7.444	35.482	99.503
$V_6$	[Nmm]	278.075	88.855	53.414	278.377

obtained by the GF- and the GC-element using a mesh of three finite elements, together with the reference solution. In particular, a zoom of the deformed shape near the loaded section is shown. It can be noted that the proposed element captures very well the localized section distortion caused by the point loads. Inspecting the graphs in Fig. 4.12, showing the  $y$ -displacement of natural node 1 of the cross-section along the beam axis, and Table 4.4, collecting the  $x$ - and  $y$ -displacement of natural node 1 of section A together with the strain energy of the beam, confirms this observation. In particular, the excellent agreement between the solution predicted by the proposed element using only three finite elements and the reference solution can be noted. Figures 4.13-4.16 show the results in terms of the most significant components of the generalized stresses. Moreover, their values near the loaded section (section A) are collected in Tables 4.5 and 4.6. The high performance of the proposed element can be noted.

Table 4.3: Z-section cantilever beam with torsional load. Generalized stresses at  $z/L = 1$ .

		GF (1 FE)	GC (1 FE)	Ref. sol.
$B$	[Nmm <sup>2</sup> ]	0	$-1.288 \cdot 10^5$	0
$T$	[Nmm]	-611.231	-685.281	-612.359
$V_\phi$	[Nmm]	-694.384	-657.360	-693.820
$S_6$	[N]	$-1.113 \cdot 10^{-2}$	$-0.380 \cdot 10^{-2}$	$-1.108 \cdot 10^{-2}$
$M_6$	[Nmm <sup>2</sup> ]	0	-0.605	0
$T_6$	[Nmm]	-0.611	-0.853	-0.615
$V_6$	[Nmm]	0.306	-0.303	0.307

Table 4.4: Clamped-clamped rack-section beam.  $x$ - and  $y$ -displacement of natural node 1 at  $z/L = 2/3$  and strain energy  $\Phi$  of the beam.

	GF (3 FE)	GC (3 FE)	3D shell	Ref. sol.
$x$ -displ. [mm]	-0.729	-0.664	-0.738	-0.728
$y$ -displ. [mm]	-0.332	-0.268	-0.3319	-0.332
$\Phi$ [Nmm]	728.660	644.148	739.4642	728.170

### 4.4.3 Cantilever beam with non-conventional cross-section

The cantilever beam with non-conventional cross-section shown in Fig. 4.17a is considered [105]. The cross-section deformation modes are shown in Fig. 4.18. The end section (section A) and the middle section (section B) of the beam are loaded by pin forces as shown in Fig. 4.17b. Figure 4.19 shows the  $\bar{x}$ -displacement of node 2 of the cross-section along the beam axis using two finite elements, and Table 4.7 collects the  $\bar{x}$ - and  $\bar{y}$ -displacement of natural node 2 of sections A and B together with the strain energy of the beam. Moreover, the results in terms of the most significative generalized



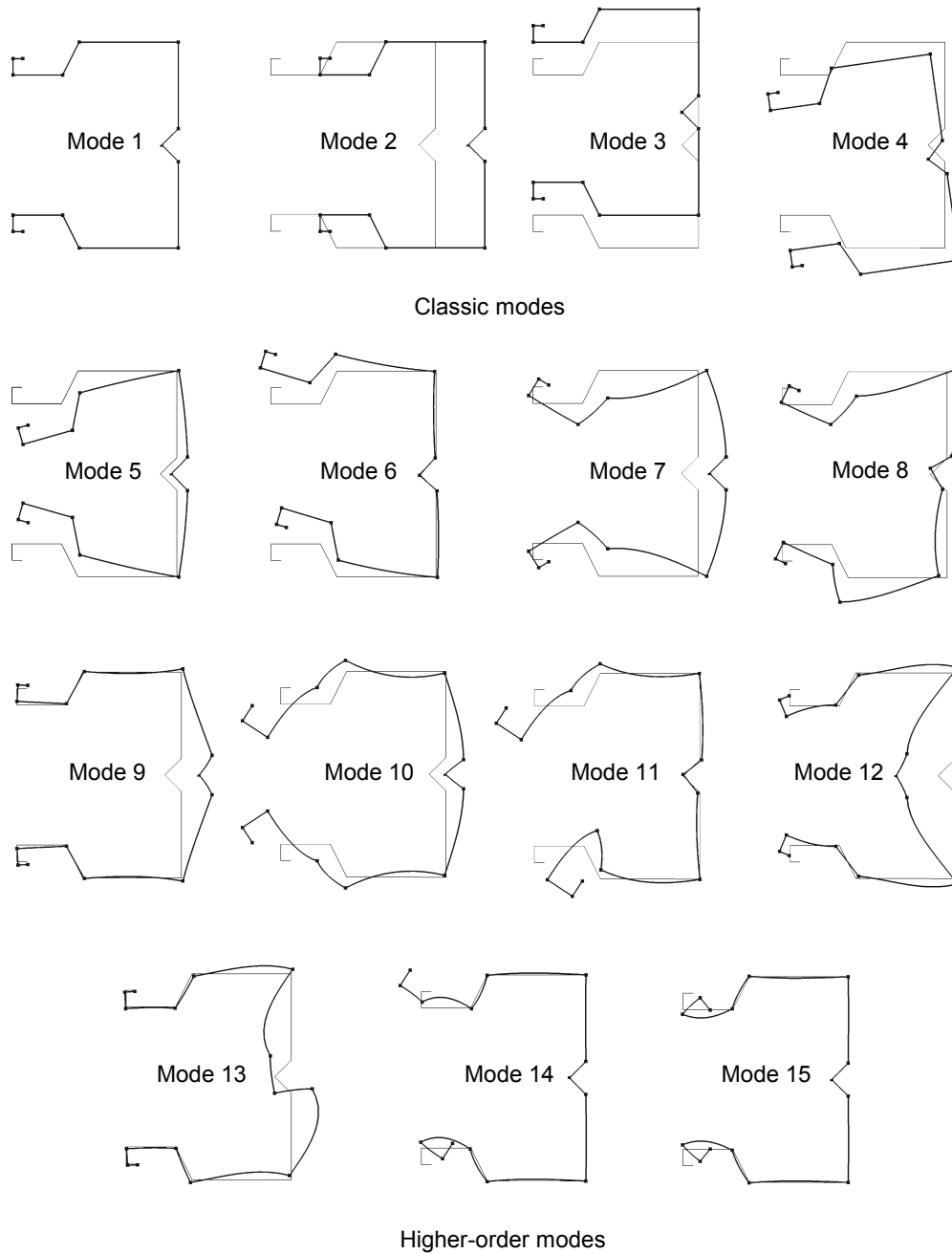


Figure 4.10: Clamped-clamped rack-section beam: in-plane configurations of cross-section deformation modes.

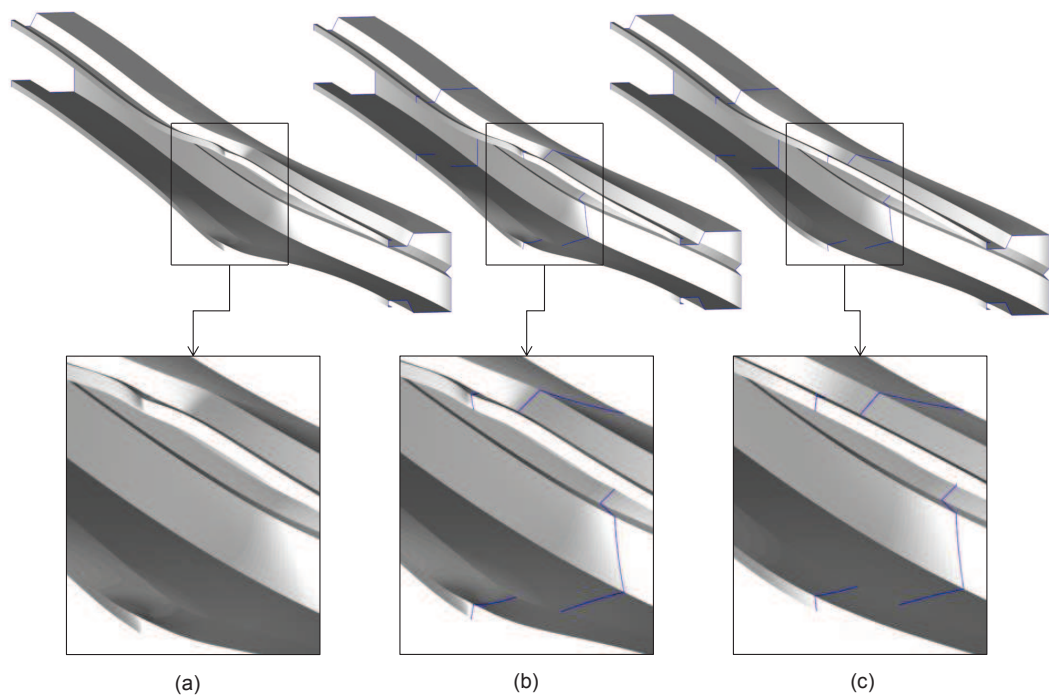


Figure 4.11: Clamped-clamped rack-section beam - Deformed shape: (a) reference solution; (b) GF-element (3 finite elements); (c) GC-element (3 finite elements).

Table 4.6: Clamped-clamped rack-section beam. Higher-order generalized stresses at  $z_1 = 0.65L$  and  $z_2 = 0.68L$ .

			GF (3 FE)	GC (3 FE)	Ref. sol.
$S_5$	[N]	$z = z_1$	$-4.352 \cdot 10^{-2}$	$-3.621 \cdot 10^{-2}$	$-4.3750 \cdot 10^{-2}$
		$z = z_2$	$-4.389 \cdot 10^{-2}$	$-3.606 \cdot 10^{-2}$	$-4.374 \cdot 10^{-2}$
$M_5$	[Nmm <sup>2</sup> ]	$z = z_1$	1464.762	586.129	1458.090
		$z = z_2$	1464.896	469.029	1458.430
$T_5$	[Nmm]	$z = z_1$	-1.118	0.131	-1.172
		$z = z_2$	1.128	-0.110	1.188
$V_5$	[Nmm]	$z = z_1$	13.190	12.948	13.216
		$z = z_2$	-13.176	-13.097	-13.202
$S_9$	[N]	$z = z_1$	$-1.231 \cdot 10^{-2}$	$-0.799 \cdot 10^{-2}$	$-1.221 \cdot 10^{-2}$
		$z = z_2$	$-1.231 \cdot 10^{-2}$	$1.062 \cdot 10^{-2}$	$-1.221 \cdot 10^{-2}$
$M_9$	[Nmm <sup>2</sup> ]	$z = z_1$	89.361	42.066	90.255
		$z = z_2$	89.361	63.108	90.276
$T_9$	[Nmm]	$z = z_1$	0.511	0.064	0.470
		$z = z_2$	-0.543	-0.084	-0.504
$V_9$	[Nmm]	$z = z_1$	1.332	1.390	1.361
		$z = z_2$	-1.351	-1.931	-1.378
$S_{15}$	[N]	$z = z_1$	-0.751	-1.852	-0.695
		$z = z_2$	-0.746	-1.858	-0.695
$M_{15}$	[Nmm <sup>2</sup> ]	$z = z_1$	-108.287	32.513	-86.216
		$z = z_2$	-108.140	32.291	-86.221
$T_{15}$	[Nmm]	$z = z_1$	32.169	2.121	32.894
		$z = z_2$	-32.354	-2.708	-33.283
$V_{15}$	[Nmm]	$z = z_1$	10.788	82.964	11.001
		$z = z_2$	-10.872	-80.878	-11.196

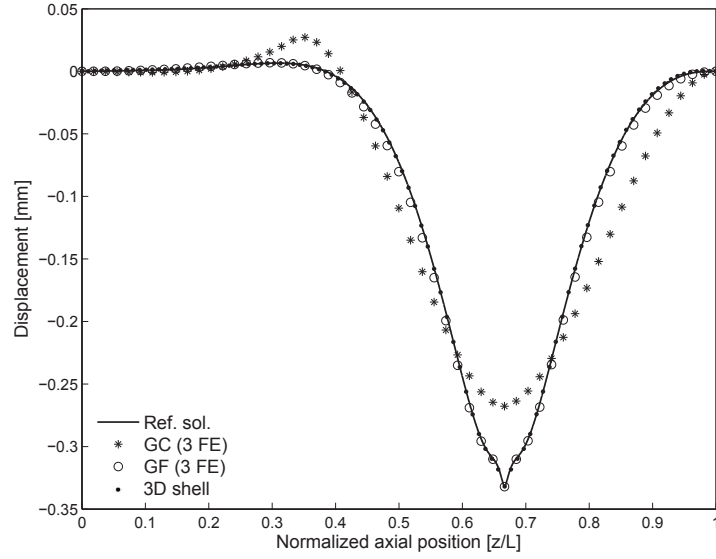


Figure 4.12: Clamped-clamped rack-section beam:  $y$ -displacement of natural node 1.

Table 4.7: Cantilever beam with non-conventional cross-section.  $\bar{x}$ - and  $\bar{y}$ -displacement of natural node 2 and strain energy  $\Phi$  of the beam.

		GF (2 FE)	GC (2 FE)	3D shell	Ref. sol.
$\bar{x}$ -displ. [mm]	Sec. A	0.815	0.988	0.831	0.815
	Sec. B	0.076	-0.225	0.0492	0.076
$\bar{y}$ -displ. [mm]	Sec. A	22.396	22.167	22.384	22.396
	Sec. B	2.801	3.235	2.816	2.801
$\Phi$ [Nmm]		$1.685 \cdot 10^4$	$1.628 \cdot 10^4$	$1.740 \cdot 10^4$	$1.685 \cdot 10^4$

stresses are reported in Figs. 4.20-4.22 and in Table 4.8. In all, these results confirm the high performance of the proposed element, with excellent agreement between its predictions and the reference solution, both in terms of displacements and stresses, despite only two finite elements are used.

Table 4.8: Cantilever beam with non-conventional cross-section. Generalized stresses at  $z/L = 1$ .

		GF (2 FE)	GC (2 FE)	Ref. sol.
$M_y$	[Nmm]	$-7.972 \cdot 10^{-4}$	-802.286	0
$V_x$	[N]	-728.138	-728.138	-728.138
$M_x$	[Nmm]	$-5.699 \cdot 10^{-4}$	-555.699	0
$V_y$	[N]	-1862.825	-1862.825	-1862.825
$B$	[Nmm <sup>2</sup> ]	0.014	$-3320.938 \cdot 10^2$	0
$T$	[Nmm]	-7262.933	-5934.822	-7271.793
$V_\phi$	[Nmm]	10389.927	9725.872	10394.357
$S_5$	[N]	-38.900	-38.814	-38.925
$M_5$	[Nmm <sup>2</sup> ]	$-5.905 \cdot 10^{-3}$	$-1438.670 \cdot 10^2$	0
$T_5$	[Nmm]	1997.967	1768.138	1987.880
$V_5$	[Nmm]	4421.333	4211.552	4426.377
$S_7$	[N]	2.791	2.576	2.788
$M_7$	[Nmm <sup>2</sup> ]	$8.798 \cdot 10^{-4}$	1739.884	0
$T_7$	[Nmm]	-60.935	-51.441	-60.815
$V_7$	[Nmm]	-142.176	-91.185	-142.236

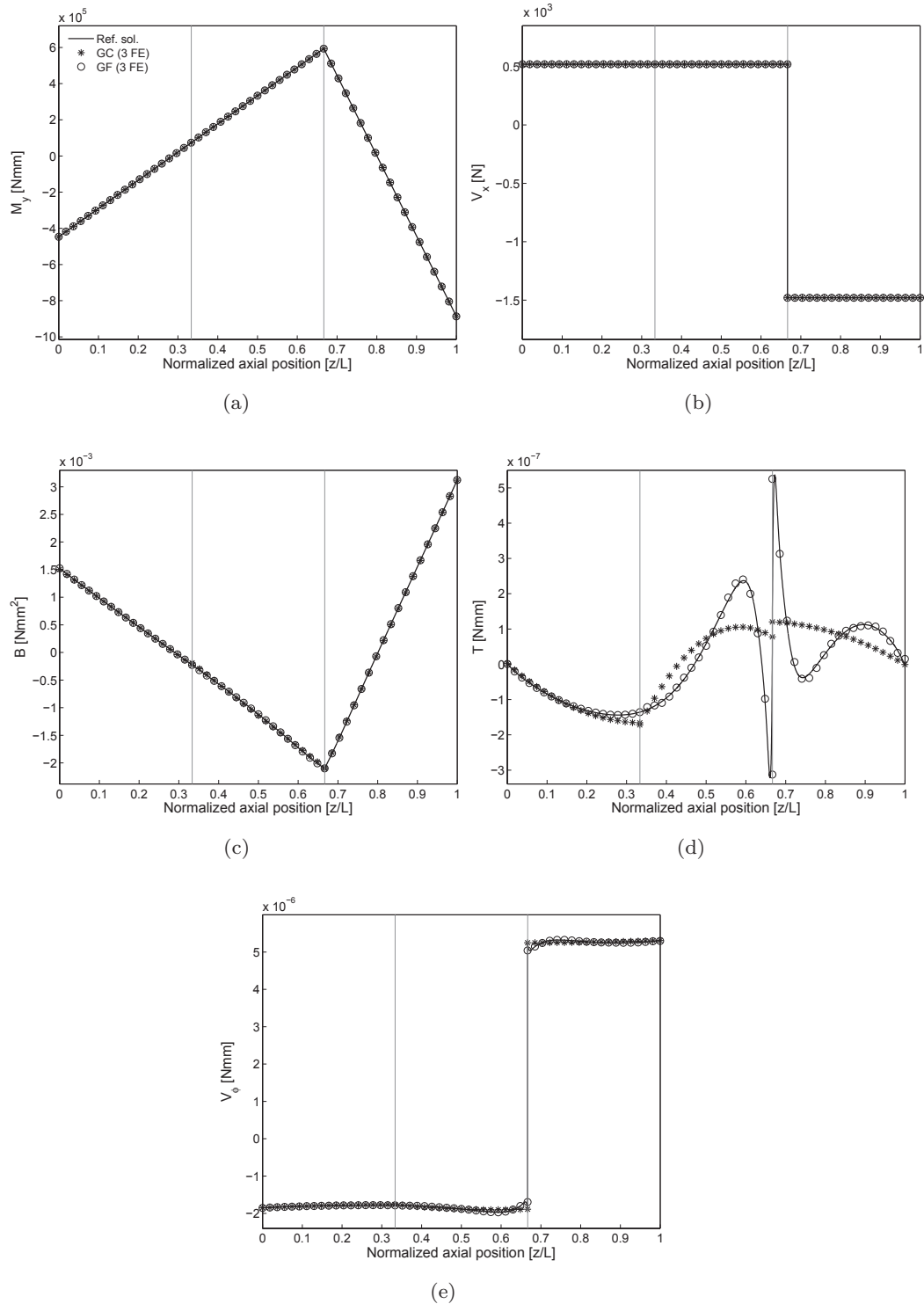


Figure 4.13: Clamped-clamped rack-section beam - Classic generalized stresses: (a)  $M_y$ ; (b)  $V_x$ ; (c)  $B$ ; (d)  $T$ ; (e)  $V_\phi$ .

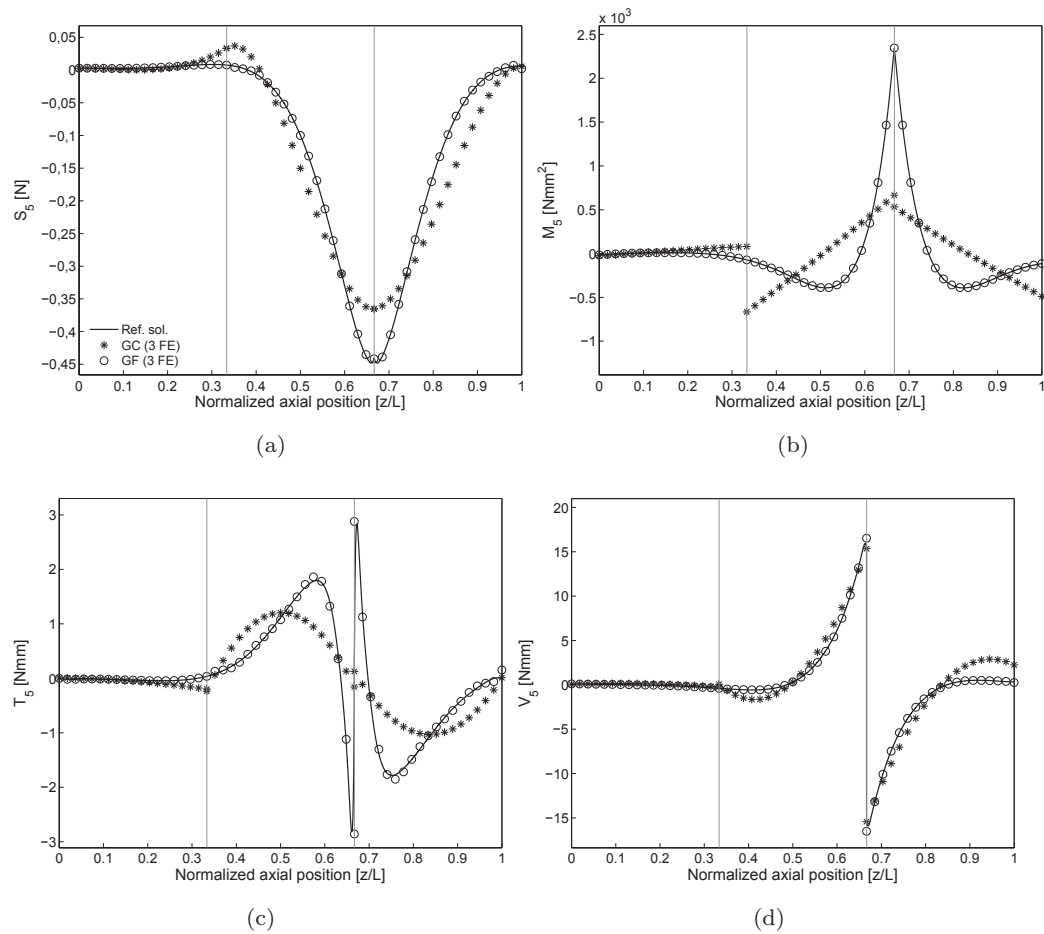


Figure 4.14: Clamped-clamped rack-section beam - Higher-order generalized stresses associated to mode 5: (a)  $S_5$ ; (b)  $M_5$ ; (c)  $T_5$ ; (d)  $V_5$ .

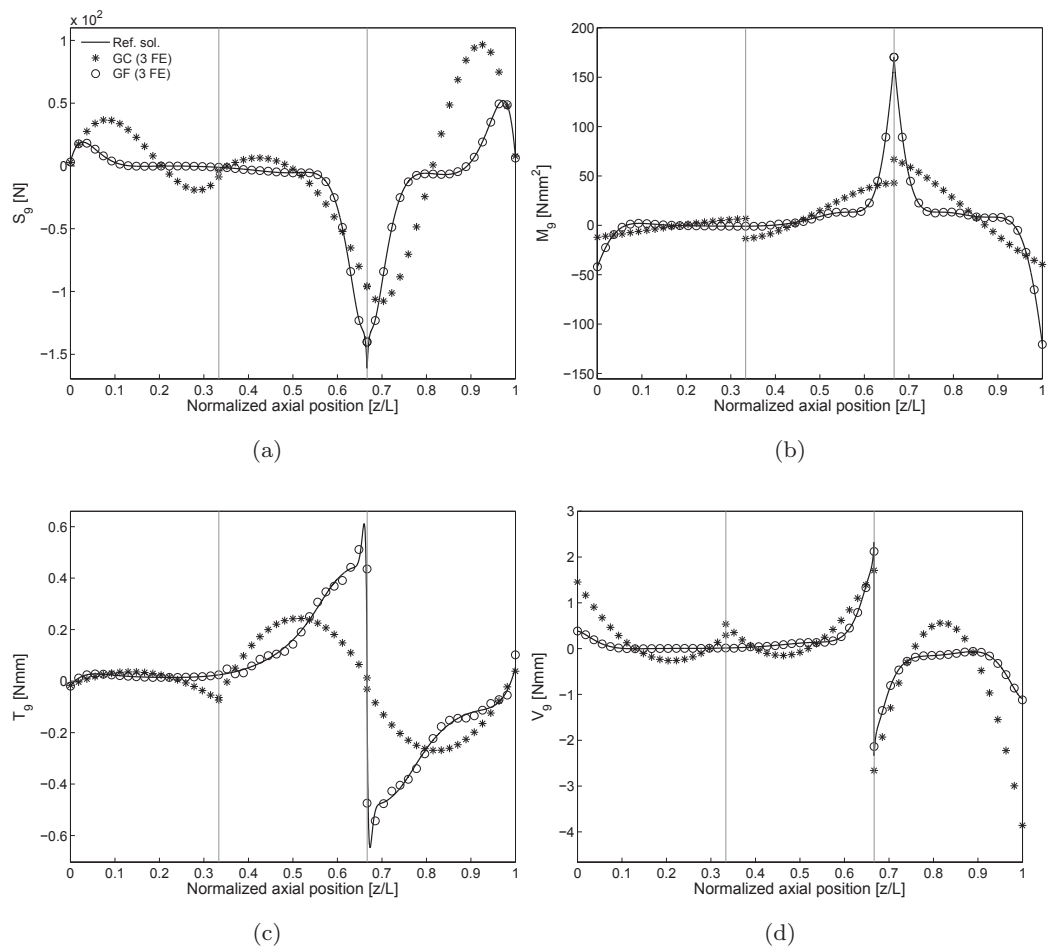


Figure 4.15: Clamped-clamped rack-section beam - Higher-order generalized stresses associated to mode 9: (a)  $S_9$ ; (b)  $M_9$ ; (c)  $T_9$ ; (d)  $V_9$ .

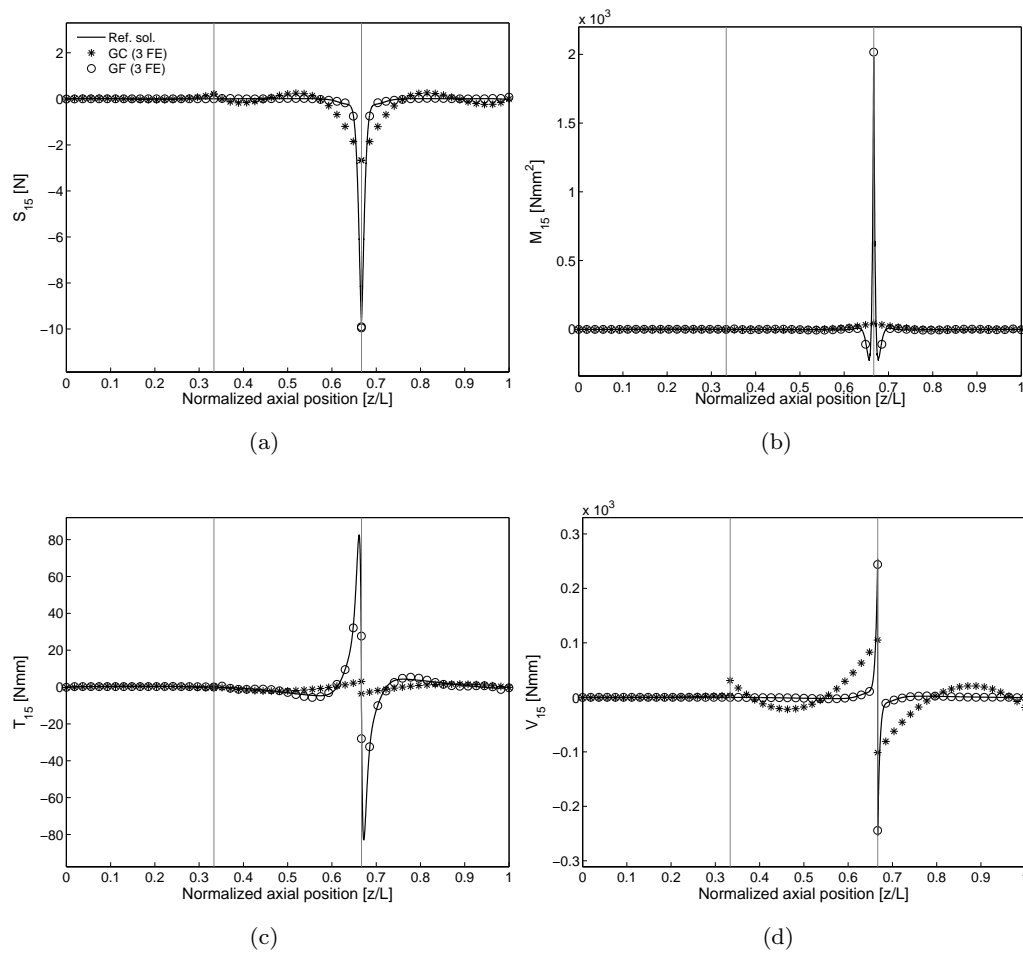


Figure 4.16: Clamped-clamped rack-section beam - Higher-order generalized stresses associated to mode 15: (a)  $S_{15}$ ; (b)  $M_{15}$ ; (c)  $T_{15}$ ; (d)  $V_{15}$ .

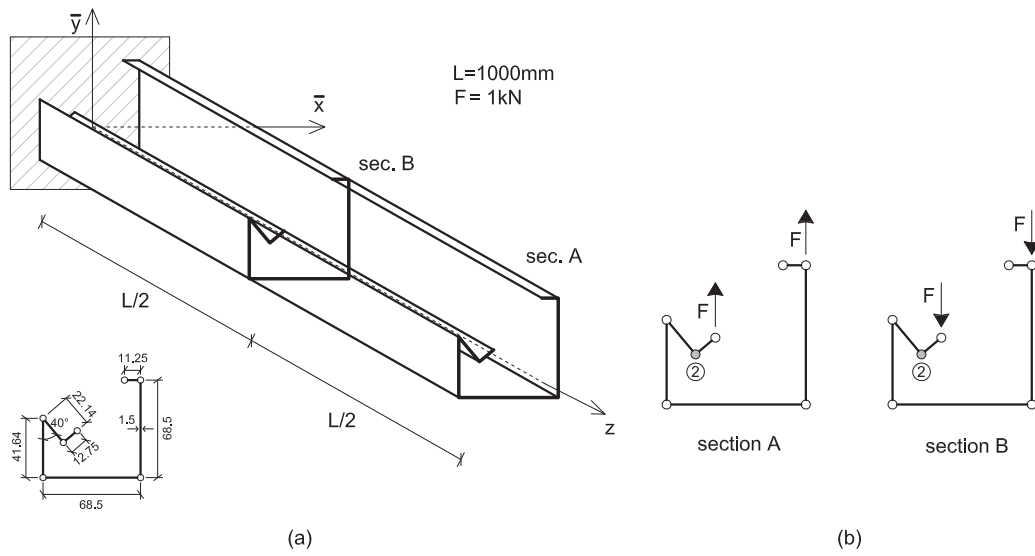


Figure 4.17: Cantilever beam with non-conventional cross-section: (a) geometry; (b) loads applied at section A and section B.

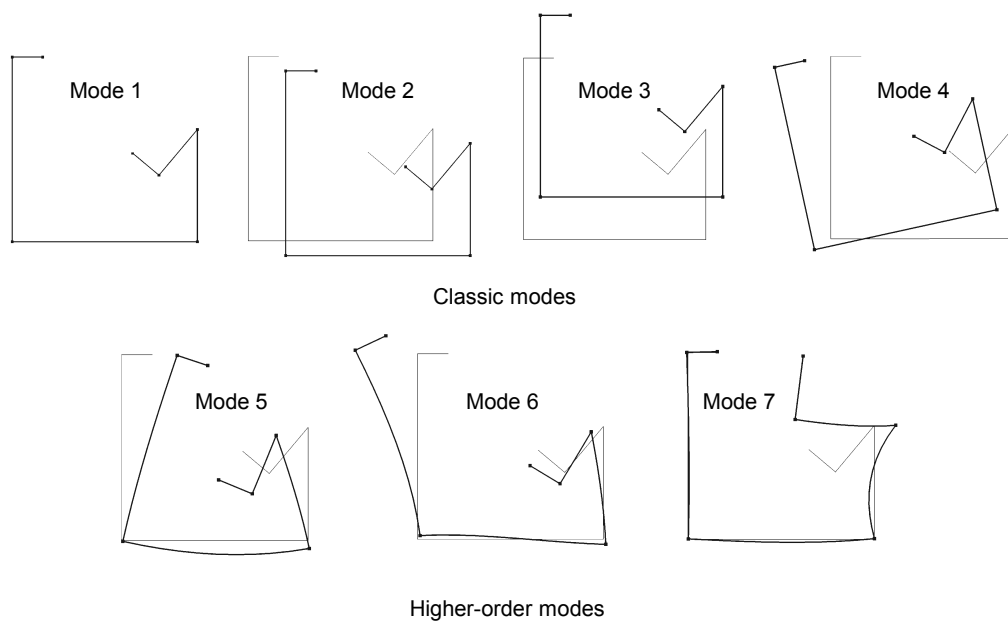


Figure 4.18: Cantilever beam with non-conventional cross-section: in-plane configurations of cross-section deformation modes.

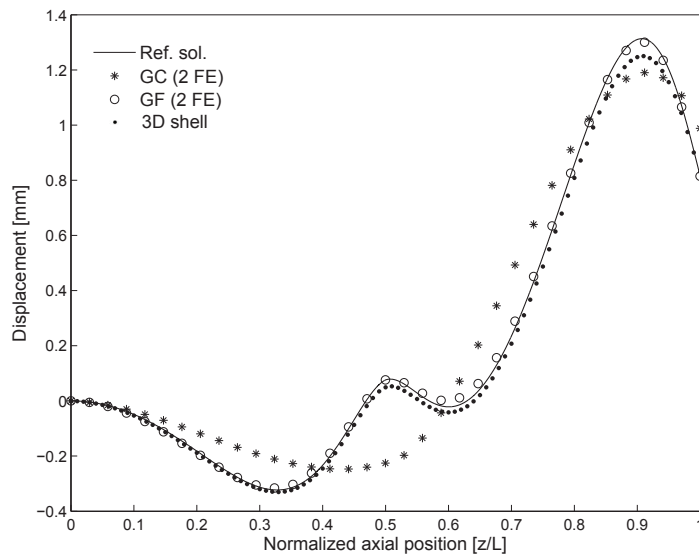


Figure 4.19: Cantilever beam with non-conventional cross-section:  $\bar{x}$ -displacement of natural node 2.

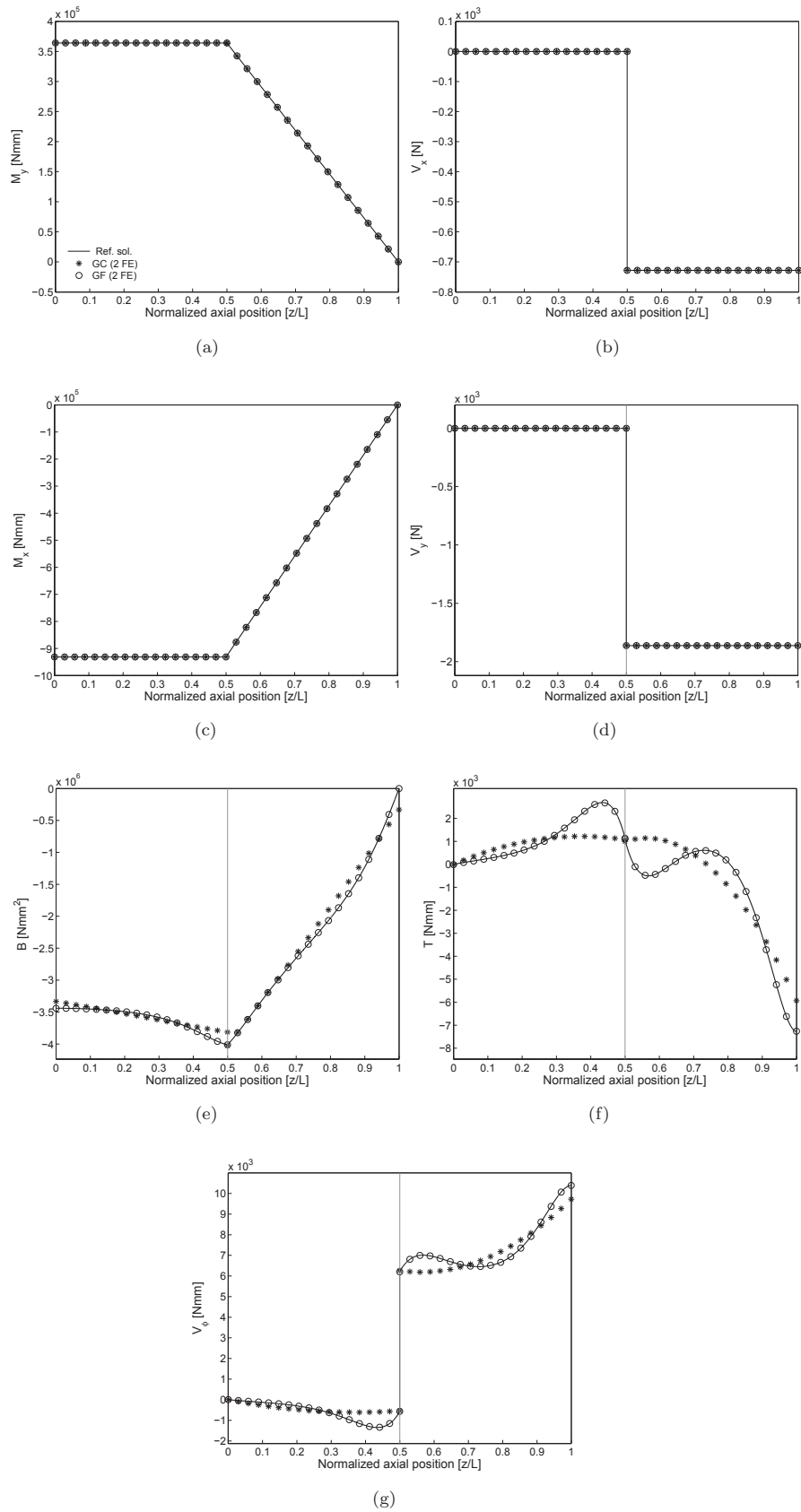


Figure 4.20: Cantilever beam with non-conventional cross-section - Classic generalized stresses: (a)  $M_y$ ; (b)  $V_x$ ; (c)  $M_x$ ; (d)  $V_y$ ; (e)  $B$ ; (f)  $T$ ; (g)  $V_\phi$ .

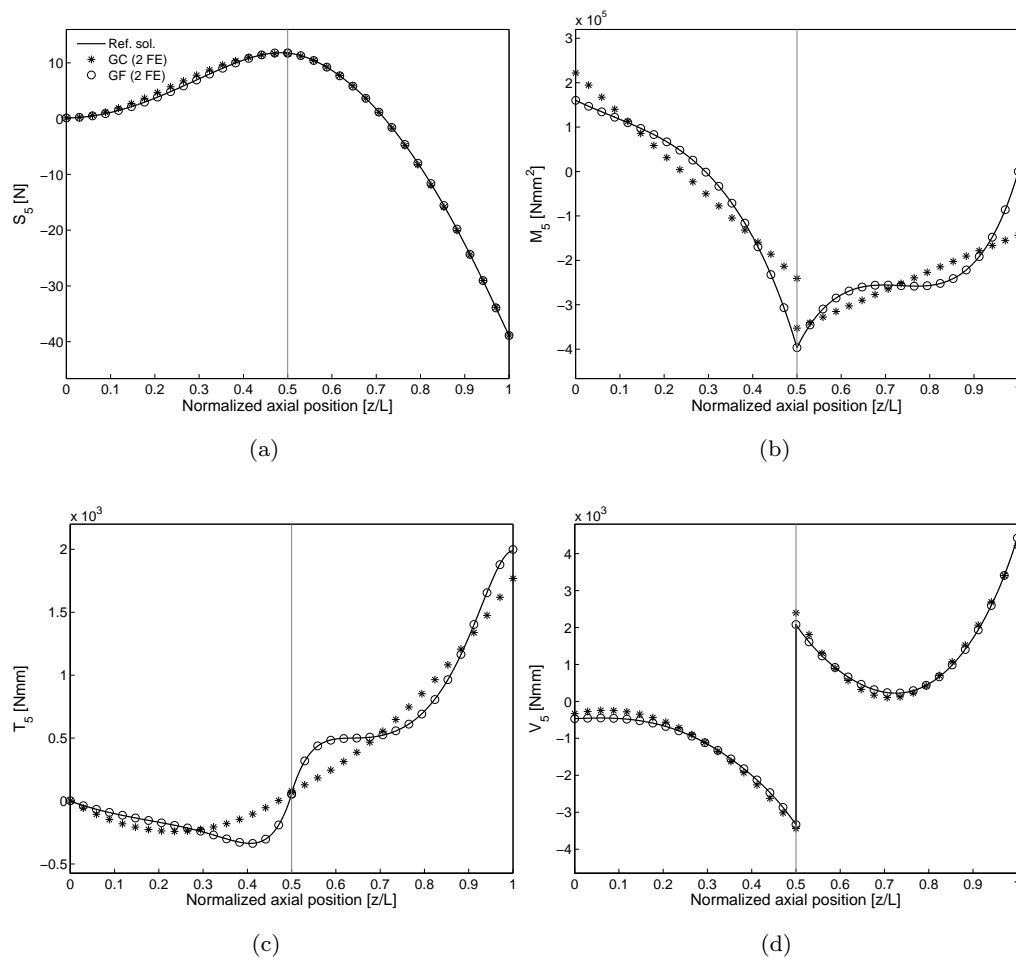


Figure 4.21: Cantilever beam with non-conventional cross-section - Higher-order generalized stresses associated to mode 5: (a)  $S_5$ ; (b)  $M_5$ ; (c)  $T_5$ ; (d)  $V_5$ .

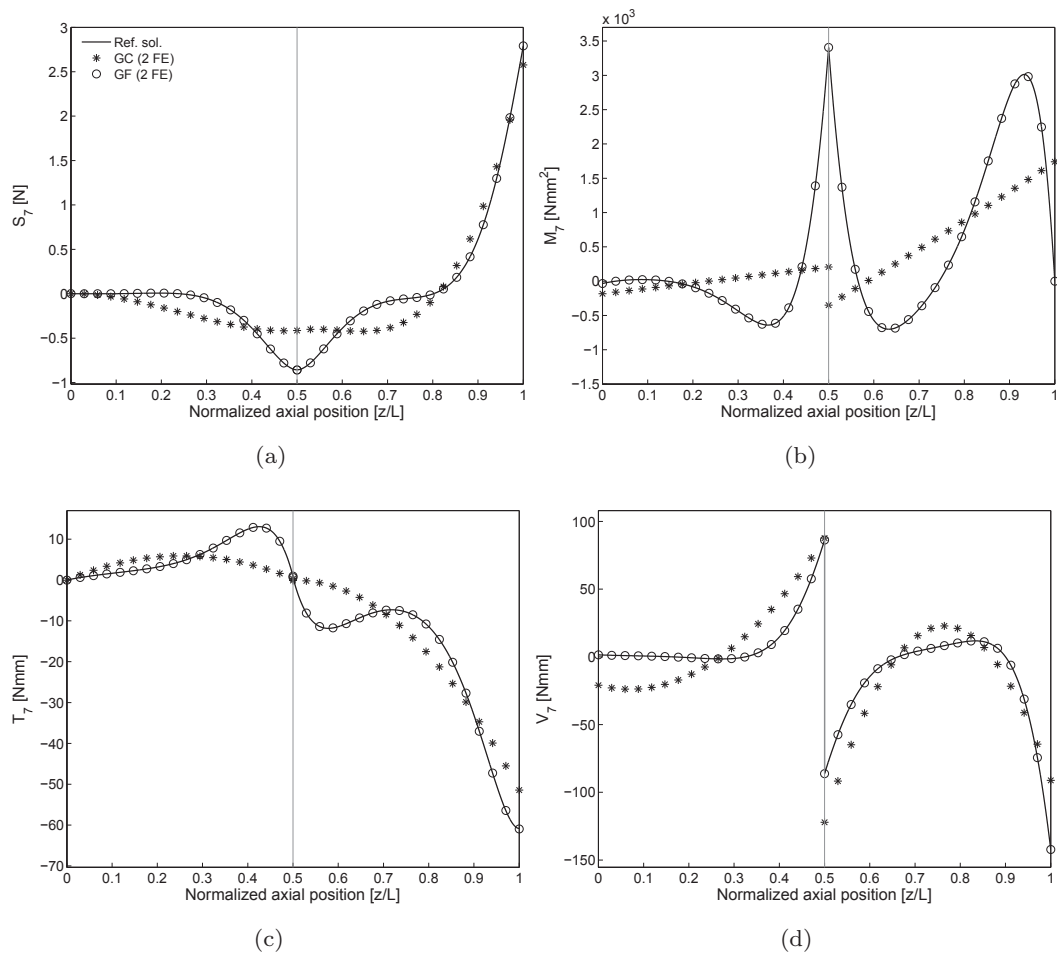


Figure 4.22: Cantilever beam with non-conventional cross-section - Higher-order generalized stresses associated to mode 7: (a)  $S_7$ ; (b)  $M_7$ ; (c)  $T_7$ ; (d)  $V_7$ .



# Chapter 5

## EuroCode3-compliant design approach: ESA

### Abstract

Following the idea early presented in [106] and more recently developed in [69] in the framework of thin-walled members stability check, a EuroCode3 (EC3) compliant approach that coherently accounts for distortional buckling is presented in this chapter. The approach, called Embedded Stability Analysis (ESA), embeds a stability analysis based on the Generalized Beam Theory of the members and is applicable in a simple and general way to the design of thin-walled members with arbitrary cross-section in the presence of local, global and distortional buckling with no limits about constraints and load conditions. Some numerical results comparing the stability check by the ESA approach and the EC3 are presented and discussed.

This chapter is organized as follows. After a brief overview on the simplified and general stability checks methods available in the EC3 (Section 5.1.1), a new verification approach, called Embedded

Stability Analysis (ESA), is presented in Section 5.1.2. A comparison between ESA approach and EC3 simplified methods is shown in Section 5.2.

## **5.1 Design of thin-walled profiles according to EC3**

In many practical cases the standards provide simplified formulas that allow the designer to project against distortional buckling, but are applicable in limited cases. For example, EC3 provides these formulas in a procedure hereinafter named EC3 “simplified method” (point 5.5.3 of [64]). Moreover, to overcome the limitations of the simplified method, the EC3 provides also a “general method” of design based on numerical analyses. In the following, these two methods are briefly illustrated.

### **5.1.1 EuroCode3 simplified and general methods**

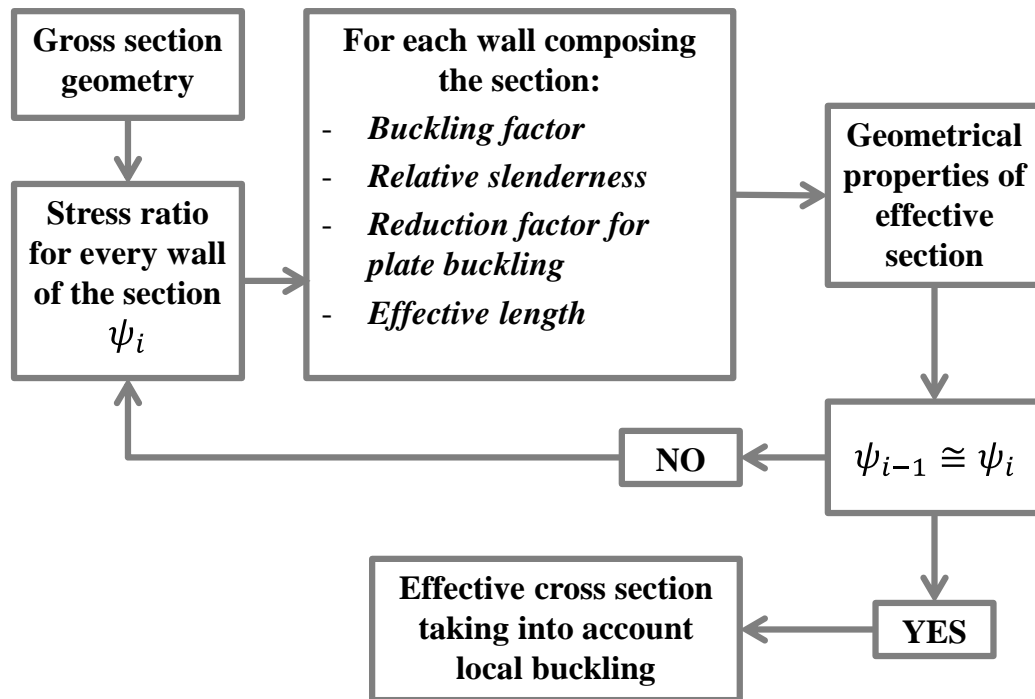
EC3 simplified method is an iterative procedure that, using the Effective Width Method (EWM) [64], considers the loss of effectiveness for each plate in the cross-section in order to take into account local buckling. Verification against distortional buckling is then carried out by reducing the effective area of flange stiffeners using an Effective Thickness Method and the calculation can be developed only after the evaluation of the effective quantities related to local

buckling, in sequential order. EC3 simplified method covers the effect of distortional-global interaction by using the effective cross-section for overall buckling strength checks. The workflows that characterize the evaluation of the effective quantities used in the EC3 simplified method are sketched in Fig. 5.1. Indeed, the effective cross-section quantities, used in the determination of the profile resistance, are obtained by means of coefficients that are provided only for special cases. This limits the applicability of the method to conventional boundary conditions. For example, it is not possible to consider the presence of continuous elastic restraints, commonly used in the modelling of purlin-roof panel interaction [29]. Moreover, if distortion phenomena are relevant and have to be taken into consideration, the simplified method is applicable only for limited cross-section shapes (Z or C) and it may be awkward and difficult to apply.

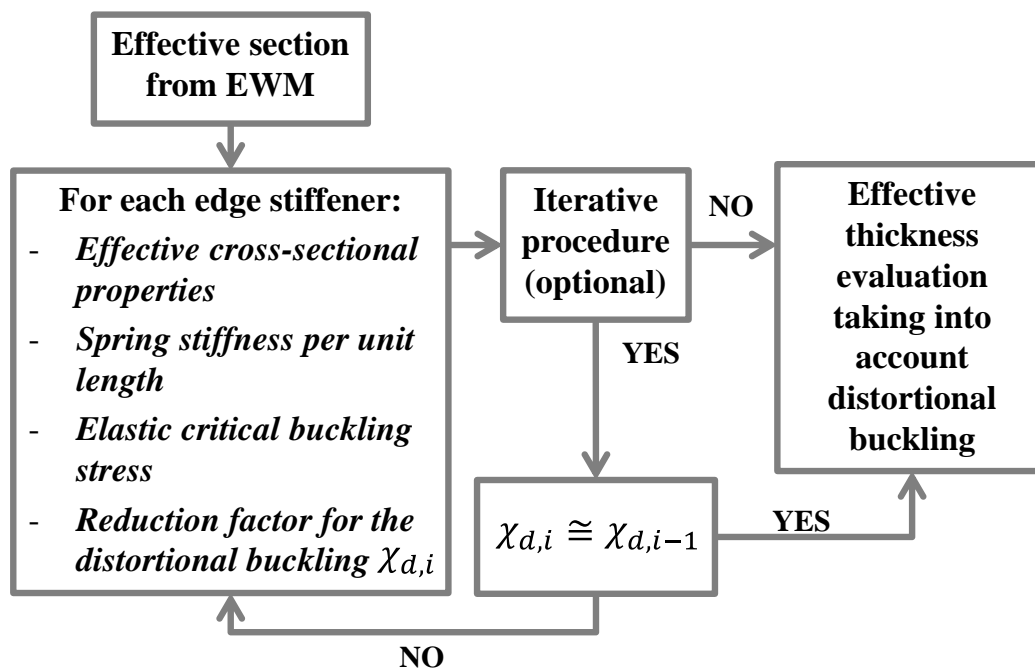
The EC3 general method is based on the use of numerical analyses and, more particularly, buckling analyses. In this case, the stability check is as follows:

$$\frac{\chi_{op}(\bar{\lambda}_{op}) \alpha_{ult,k}}{\gamma_{M1}} \geq 1 \quad (5.1)$$

where  $\chi_{op}$  is the resistance reduction factor,  $\gamma_{M1}$  is a partial safety factor,  $\alpha_{ult,k}$  is the minimum amplifier for the design loads to reach the elastic critical resistance of the most critical cross-section (commonly evaluated using the EWM) and  $\bar{\lambda}_{op} = \sqrt{\alpha_{ult,k}/\alpha_{cr,op}}$  is the non-dimensional slenderness that describes the attitude of the element to buckle in the relevant buckling mode, being  $\alpha_{cr,op}$  the



(a)



(b)

Figure 5.1: EC3 simplified method: a) Effective Width Method workflow, b) Effective Thickness Method workflow.

minimum amplifier for the design loads to reach the elastic critical resistance of the structural component with regards to lateral or lateral torsional buckling, considering distortional behaviour. In an EC3 general method compliant approach,  $\alpha_{cr,op}$  would be calculated with numerical analyses. To this purpose, the Constrained Finite Strip Method (cFSM), used in the American standard and implemented in CUFSM software [19], or three-dimensional finite element modelling performed by general purpose commercial software could be used. On this regard, it is worth to note that cFSM has not a general applicability because it does not allow generic cross-sections or generic loads and restraints. On the other hand, the use of three-dimensional finite element models built with general purpose commercial software allows to analyse general structural systems. However, in this case there are non-negligible operational difficulties related to the setup of the model and the interpretation of the results. Moreover, they are not generally applicable to large scale analyses because of their high computational cost. A further possibility, compliant with the EC3 general method, is given by the GBT, used in the ESA approach described in the following section.

### 5.1.2 ESA approach

The proposed ESA approach is developed along the same conceptual path of the EC3 general method, Eq. 5.1. As it is common in the engineering practice, in the ESA approach the stability check is done on an equivalent system, obtained “extracting” the

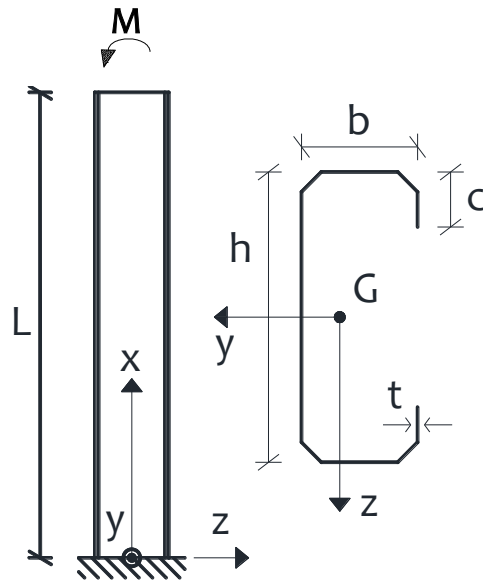
generic member to be verified from the parent structure and applying proper loads and constraints, both at the ends or at intermediate sections. One of the original aspects that characterizes the ESA approach consists in the evaluation of  $\alpha_{cr,op}$ . In fact, the minimum amplifier  $\alpha_{cr,op}$  is evaluated numerically, by means of a linear buckling analysis performed on a GBT-based finite element model of the equivalent system. In the GBT, the assumption of rigid in-plane cross-sections is removed, so allowing to consider in a comprehensive fashion the different instability phenomena, occurring at different wavelengths: local, distortional and global buckling. Thanks to its modal nature, the GBT allows to easily restraint modes related to distortional or local effects. Accordingly, using the GBT, two possible evaluations of the parameter  $\alpha_{cr,op}$  can be obtained, whether the distortional modes are present ( $\alpha_{cr,op}^{GBT}$ ) or restrained ( $\alpha_{cr,op}^{GBT_r}$ ). Moreover, it is possible to define the coefficient  $\bar{\beta} = \alpha_{cr,op}^{GBT} / \alpha_{cr,op}^{GBT_r}$ , which can be seen as an indicator of the importance of the section distortion. This parameter, not present in standards, is a way to control the influence of distortional buckling over the global behaviour of structural components: distortional buckling become more relevant as  $\bar{\beta}$  becomes lower than 1. In other words, it allows verifying, in a simple and intuitive manner, the goodness of a design choice without performing more complex calculations.

It is worth to mention that the described approach can handle complex support conditions and, also, elastic continuous restraints. It

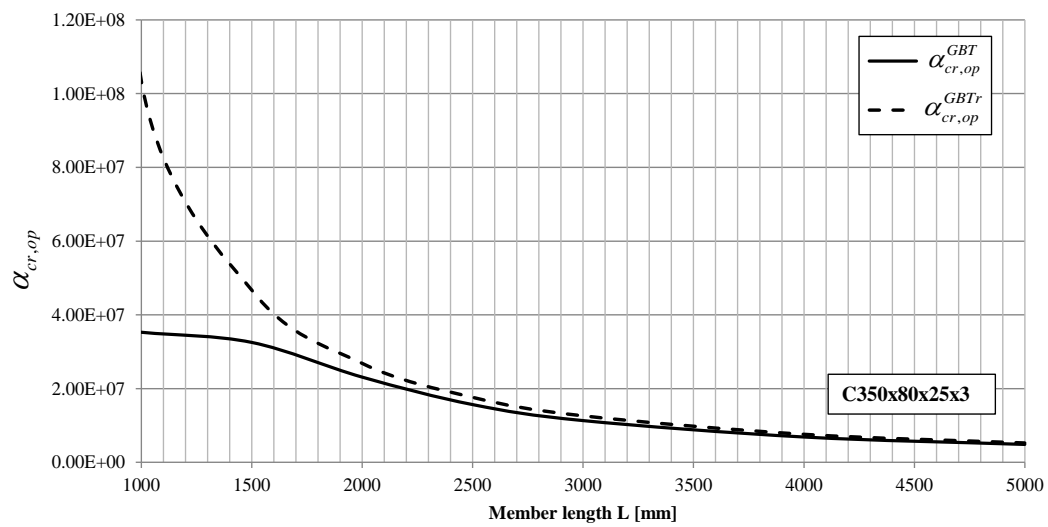
is also clear, from the above considerations, that is not necessary to define any effective length of the structural element and there are not limitations on the cross-section geometry (open, closed, branched or unbranched). For illustrative purposes, consider the C-section cantilever beam loaded by a concentrated moment  $M$  at the free end shown in Fig. 5.2a. The comparison between the two load amplifiers  $\alpha_{cr,op}^{GBT}$  and  $\alpha_{cr,op}^{GBT^r}$  for a C350x80x25x3 profile (assuming  $M = 1$ ) is shown in Fig. 5.2b. As it can be noted, the effects of section distortion become relevant for beam lengths  $L < 2000/2500mm$ .

## 5.2 Stability check: ESA vs EC3 simplified method

Here, the results of a comparison between the stability check of the proposed ESA approach and of the EC3 simplified method, on a large number of cases involving Class 4 steel cold-formed elements, are presented. A C-section cantilever beam loaded by a concentrated moment at the free end, shown in Fig. 5.2a, has been chosen as test case. 11 different C-sections have been considered, with web/flange ratios from 3 to 5. Moreover, various beam lengths have been considered in order to cover a wide range of longitudinal slenderness. Figs. 5.5-5.8 shows the buckling deformed shapes associated with the most representative results. In particular Figs. 5.5a, 5.6a, 5.7a, 5.8a show various distortional buckling modes, while Figs. 5.5b, 5.6b, 5.7b, 5.8b show lateral-torsional buckling modes. The results of the stability check, Eq. 5.1, expressed in terms of



(a)



(b)

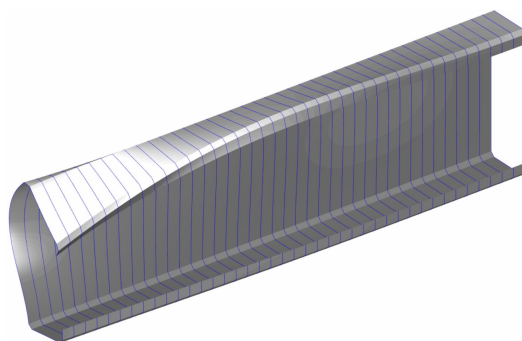
Figure 5.2: Cantilever beam: a) geometry, load and boundary conditions; b)  $\alpha_{cr,op}^{GBT}$ ,  $\alpha_{cr,op}^{GBT_r}$  comparison.

the ratio ESA/EC3 are collected in Fig. 5.3. For all the cases, the applied moment  $M$  is such that the EC3 stability check is equal to 1. As it can be noted, EC3 stability check is not always on the safe side: about 32% checks (23 cases out of 70) are not verified with the ESA approach (gray boxes in Fig. 5.3). This highlights the importance of properly considering distortional buckling. In fact, for elements with length  $< 2000mm$ , i.e. with high web/flange section ratio, the EC3 simplified method does not properly takes into account for the distortional behavior and is not on the safety side. The general checks trend shown in Fig. 5.3 is reflected in the pattern of Fig. 5.4 collecting parameter, so underlining the good predictive capability of this coefficient.

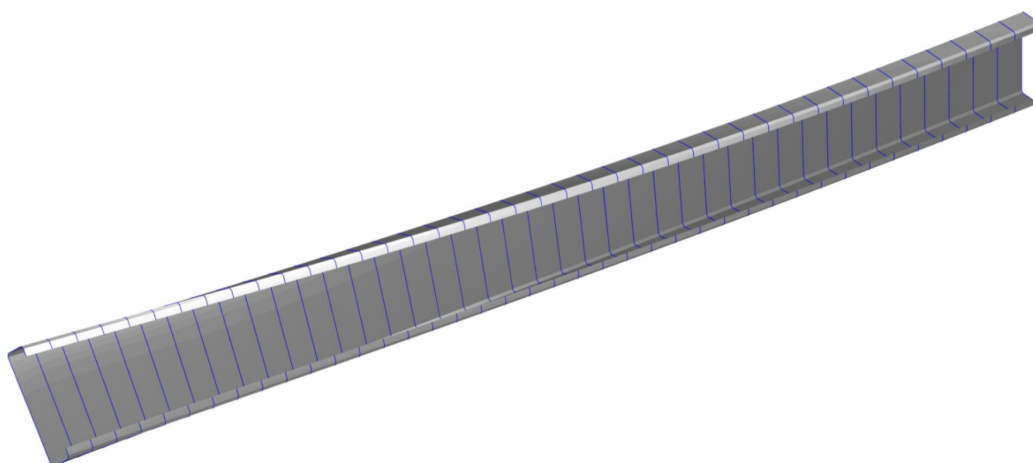
C-h*b*c*t [mm]	Cantilever length [mm]						
	1000	1500	2000	2500	3000	4000	5000
C-400*80*30*3	0.50	0.56	0.71	0.86	0.90	0.91	0.92
C-350*80*25*3	0.55	0.62	0.81	0.90	0.91	0.91	0.92
C-300*70*20*2.5	0.54	0.65	0.88	0.93	0.93	0.93	0.94
C-280*70*20*2.5	0.57	0.69	0.91	0.93	0.93	0.94	0.94
C-260*70*20*2	0.52	0.61	0.85	0.95	0.95	0.95	0.95
C-220*60*20*2	0.60	0.78	0.94	0.94	0.94	0.94	0.95
C-200*60*20*2	0.63	0.82	0.94	0.94	0.94	0.94	0.95
C-160*50*15*2	0.73	0.94	0.93	0.93	0.93	0.93	0.94
C-150*50*15*2	0.75	0.94	0.93	0.93	0.93	0.93	0.94
C-120*40*15*2	0.91	0.92	0.91	0.92	0.92	0.92	0.93

Figure 5.3: ESA/EC3 stability check.

C-h*b*c*t [mm]	Cantilever length [mm]						
	1000	1500	2000	2500	3000	4000	5000
C-400*80*30*3	0.08	0.28	0.58	0.81	0.88	0.90	0.91
C-350*80*25*3	0.09	0.34	0.70	0.86	0.89	0.90	0.91
C-300*70*20*2.5	0.12	0.43	0.82	0.90	0.92	0.92	0.93
C-280*70*20*2.5	0.13	0.46	0.85	0.91	0.92	0.92	0.93
C-260*70*20*2	0.10	0.36	0.76	0.92	0.93	0.94	0.94
C-220*60*20*2	0.17	0.61	0.90	0.93	0.93	0.94	0.94
C-200*60*20*2	0.19	0.67	0.91	0.93	0.93	0.94	0.94
C-160*50*15*2	0.34	0.89	0.91	0.92	0.92	0.93	0.93
C-150*50*15*2	0.36	0.89	0.91	0.92	0.92	0.93	0.93
C-120*40*15*2	0.73	0.89	0.90	0.91	0.92	0.92	0.92

Figure 5.4:  $\bar{\beta}$  parameter.

(a)



(b)

Figure 5.5: Buckling modes of C150x50x15x2 with length a) 500mm and b) 2000mm.

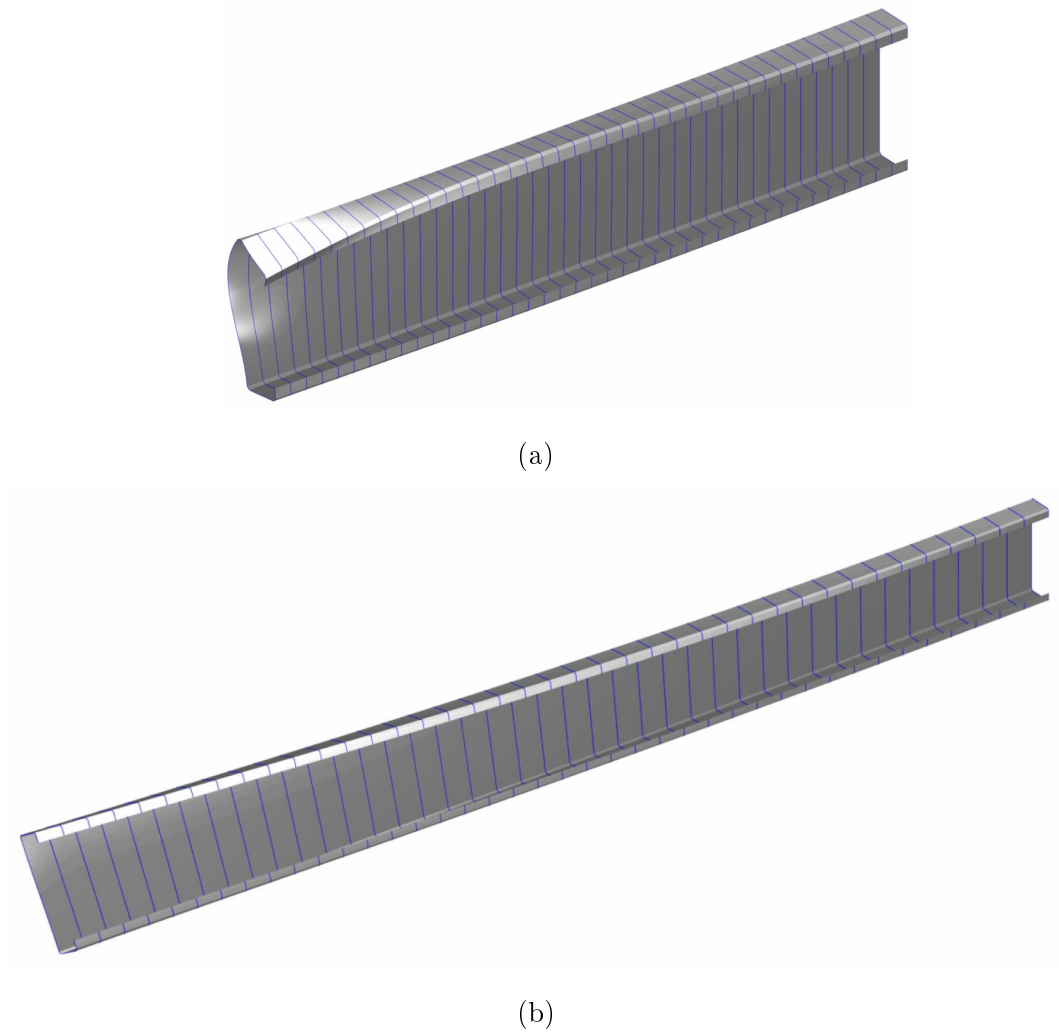
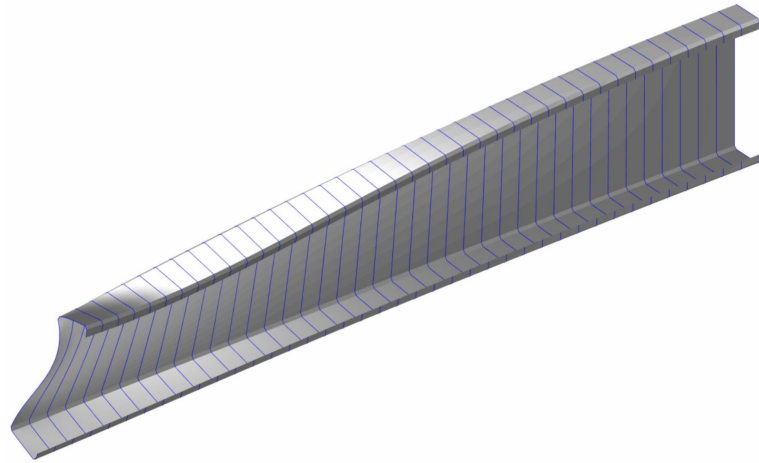
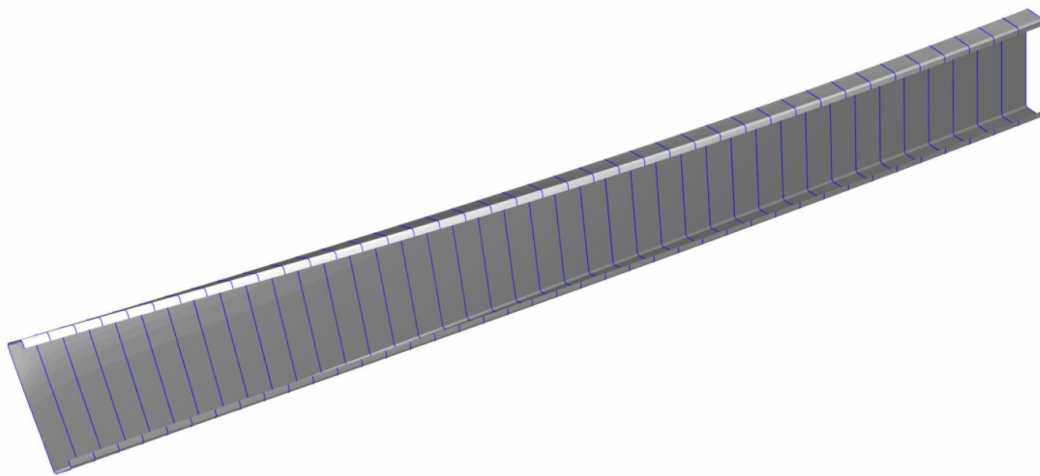


Figure 5.6: Buckling modes of C220x60x20x2 with length a) 1000mm and b) 2500mm.



(a)



(b)

Figure 5.7: Buckling modes of C280x70x25x2.5 with length a) 1500mm and b) 3000mm.

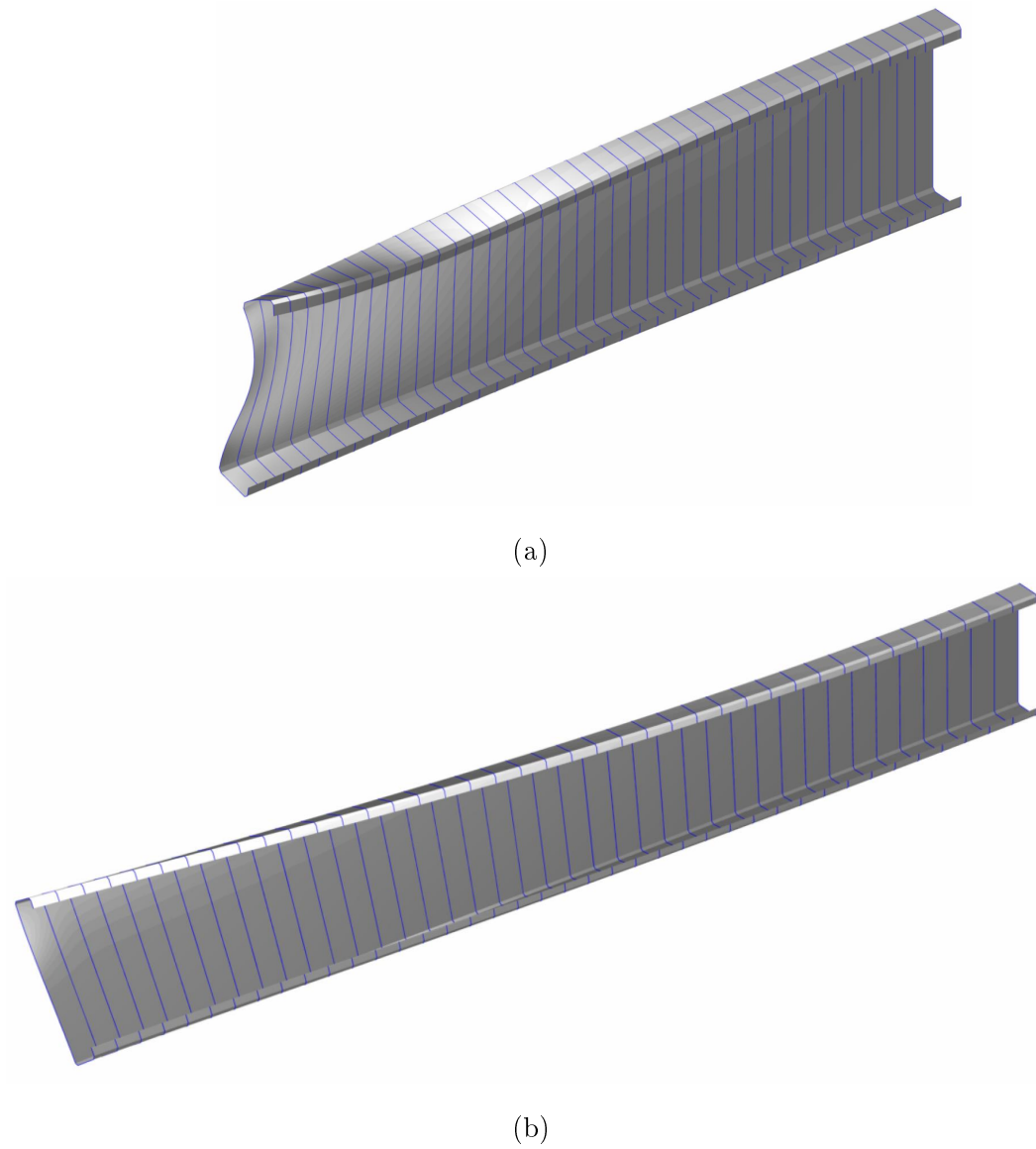


Figure 5.8: Buckling modes of C350x80x25x3 with length a) 1500mm and b) 3000mm.



# Chapter 6

## GBT-based ECBL approach

### Abstract

The Erosion of Critical Bifurcation Load (ECBL) approach is a practical tool to characterize the instability behaviour of thin-walled cold-formed steel members. In this framework, the GBT is used to find (1) the interaction point of buckling modes and (2) the erosion of the critical bifurcation load referred to this interactive buckling of two or more buckling modes associated with the same critical load. In this sense a modified version of the ECBL approach is presented. Some numerical results involving pallet rack uprights in compression are presented and compared with experimental ones, classical ECBL approach and EN 1993-1-3.

This chapter is organized as follows. After a brief overview of the conventional ECBL approach, a modified ECBL approach is presented in Section 6.1. In order to better explain the workflow, some numerical results related to pallet rack uprights in compression (RSB125x3.2 and RSB95x2.6) are shown in Section 6.2. In particular, after evaluating the interaction points using the GBT

(Section 6.2.1), the erosions and the ECBL buckling curves are shown and compared in Section 6.2.2.

## 6.1 Erosion of Critical Bifurcation Load

Coupled instabilities represent a characteristic of thin-walled steel members in compression or bending. The actual buckling curves included in the design codes, i.e. EN 1993-1-3 [65], are based on experimental tests carried out on hot-rolled sections. For the purpose of practical use these curves have been adapted in order to cover the stability design problems of thin-walled cold-formed steel members. In case of compact sections the erosion is due to the imperfections, while for thin-walled members, supplementary erosion is induced by the phenomenon of coupled instabilities. Given a member in compression, it is assumed that two simultaneous, interacting buckling modes may occur (Fig. 6.1). If  $N_u$  is the critical

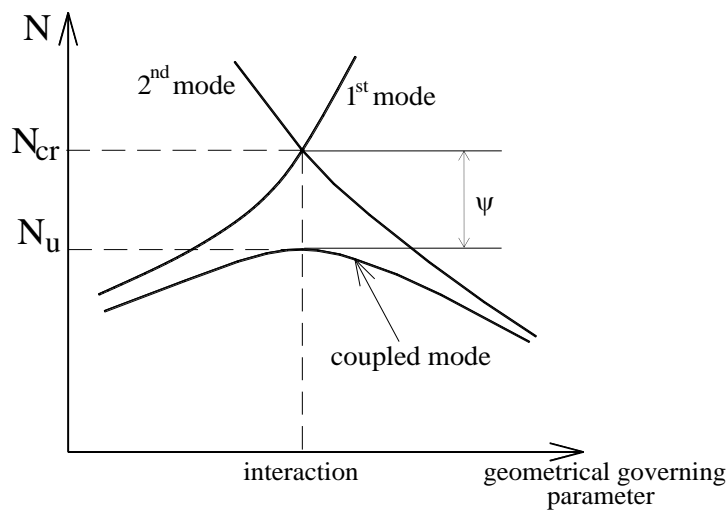


Figure 6.1: Sketch of two mode interaction [71].

ultimate load, and  $N_{cr}$  the ideal critical one, the following relation may be written:

$$N_u = (1 - \psi) N_{cr}, \quad (6.1)$$

where  $\psi$  is the erosion factor, introduced as a measure of erosion of critical load. Gioncu [72] classified the interaction types by means of this erosion factor, as follows:

- class I: weak interaction (W),  $\psi \leq 0.1$ ;
- class II: moderate interaction (M),  $0.1 < \psi \leq 0.3$ ;
- class III: strong interaction (S),  $0.3 < \psi \leq 0.5$ ;
- class IV: very strong interaction (VS),  $\psi > 0.5$ .

Obviously, an appropriate framing of each type of coupled instability into the relevant class is very important because the methods of analysis used for design have to be different from one class to another. In case of weak or moderate interaction, structural reliability will be provided by simply using design code safety coefficients, while in case of strong or very strong interaction, special methods are needed.

### 6.1.1 Classical ECBL approach

In [73], Dubina summarized the main coupled instability cases, which may appear within the bar members. In particular, based on the concept of Erosion of Critical Bifurcation Load (ECBL), Dubina proposed an approach to evaluate the ultimate strength

in local/distortional-global interactive buckling. This approach enables to use the Ayrton-Perry format of European buckling curves [72, 74] to calibrate appropriate buckling curves for any kind of interactive local/distortional-global buckling.

To illustrate the ECBL approach, let consider Fig. 6.2 showing the typical theoretical buckling curves of a thin-walled member in compression (black curves) and the actual one (green curve).

In Fig. 6.2, curve G denotes the quantities associated to global

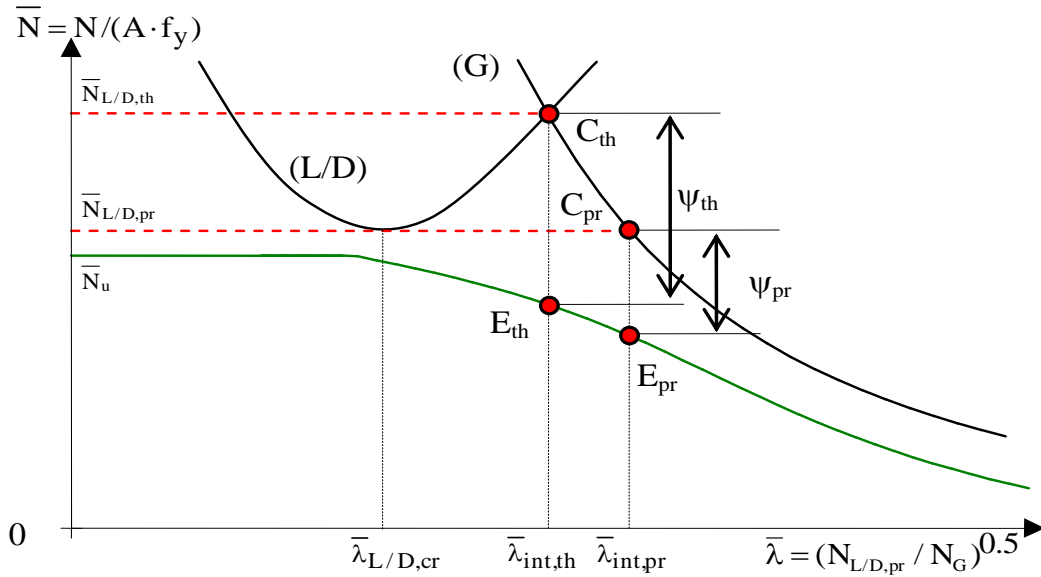


Figure 6.2: Interactive buckling model based on the ECBL approach.

buckling modes, while curve L/D those associated to local/distortional ones. Moreover,  $\bar{N}$  is the dimensionless axial force (being  $N$  the axial force and  $Af_y$  the plastic strength of full cross-section) and  $\bar{\lambda}$  is the dimensionless slenderness (being  $N_{L/D,pr}$  the smallest value between the non-dimensional local or distortional critical buckling load and the non-dimensional reduced section plastic resistance of the member, and  $N_G$  the critical global buckling load).

As it can be noted, global mode (G) interacts with local/distortional (L/D) one. The classical ECBL approach proposed by Dubina in [73] to evaluate the ultimate strength in global-local/distortional interactive buckling, hereinafter called  $ECBL_{pr}$ , is based on the main hypothesis that the erosion of the buckling load is most significant when the global buckling load is almost equal to the minimum value of local/distortional one [70, 71]. In particular, in the  $ECBL_{pr}$  the “practical interaction point”, marked as  $C_{pr}$  in Fig. 6.2, is assumed as the point where the erosion of the critical load,  $\psi_{pr}$ , is maximum. The erosion can be expressed as follows:

$$\psi_{pr} = 1 - \bar{N}_u / \bar{N}_{L/D,pr} \quad (6.2)$$

where  $\bar{N}_u$  is the dimensionless ultimate load.

In the framework of the  $ECBL_{pr}$  approach, the Ayrton-Perry formula can be written as

$$(\bar{N}_{L/D,pr} - \bar{N}) (1 - \bar{N}\bar{\lambda}^2) = \alpha_{pr}\bar{N} (\bar{\lambda} - 0.2) \quad (6.3)$$

where  $\alpha_{pr}$  is the imperfection factor. Substituting the coupling point  $E_{pr}$  in the above equation leads to

$$\alpha_{pr} = \frac{\psi_{pr}^2}{1 - \psi_{pr}} \frac{\sqrt{\bar{N}_{L/D,pr}}}{1 - 0.2\sqrt{\bar{N}_{L/D,pr}}}. \quad (6.4)$$

### 6.1.2 Modified ECBL approach

Inspecting the graph in Fig. 6.2, It is also possible to identify the “theoretical interaction point”, marked as  $C_{th}$ , corresponding to the

intersection of the two buckling modes. Its related erosion  $\psi_{th}$  is:

$$\psi_{th} = 1 - \bar{N}_u / \bar{N}_{L/D,th} \quad (6.5)$$

Following the same path outlined above, a new version of the ECBL approach, hereinafter called ECBL<sub>th</sub>, can be presented. It mainly consists in using the theoretical erosion,  $\psi_{th}$ , instead of the practical one,  $\psi_{pr}$ , to evaluate the buckling strength curves. The starting point is still Eq. 6.3, but now it is solved considering the coupling point  $E_{th}$  instead of  $E_{pr}$ . The following new expression for the imperfection factor, renamed  $\alpha_{th}$ , is obtained:

$$\alpha_{th} = \frac{\psi_{th}^2 + \left( \frac{\bar{N}_{L/D,pr}}{\bar{N}_{L/D,th}} - 1 \right) \psi_{th}}{1 - \psi_{th}} \frac{\sqrt{\bar{N}_{L/D,th}}}{1 - 0.2\sqrt{\bar{N}_{L/D,th}}} \quad (6.6)$$

Figs. 6.3, 6.4 and 6.5 show the variation of  $\alpha_{th}$  depending on  $\psi_{th}$ ,  $\bar{N}_{L/D,pr}$  and  $\bar{N}_{L/D,th}$ . The results related to the application of the ECBL<sub>th</sub> approach and the comparison with those coming from the ECBL<sub>pr</sub> one are shown in the following.

## 6.2 Numerical results

In this section, the numerical results obtained for the rack-section-members RSB125x3.2 and RSB95x2.6 in compression both with the ECBL<sub>pr</sub> approach and the ECBL<sub>th</sub> one are shown and compared with experimental results. Experimental results come from an extensive campaign [76, 77] carried out at the CEMSIG Research Center (<http://cemsig.ct.upt.ro/>) within the Department of Steel Structures and Structural Mechanics of the Politehnica University

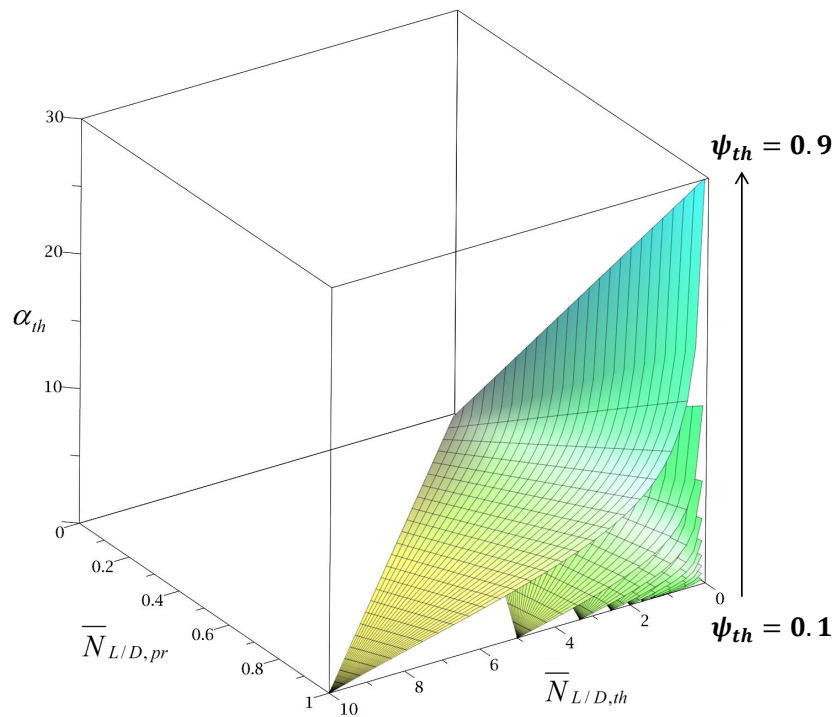


Figure 6.3: Variation of  $\alpha_{th}$  depending on  $\psi_{th}$ ,  $\bar{N}_{L/D,pr}$  and  $\bar{N}_{L/D,th}$ .

of Timisoara. Also, for comparison, the curve obtained with EN 1993-1-3 [64] is included. The theoretical buckling curves and the coupling points have been obtained using the GBT. The numerical ultimate loads have been obtained with Geometrically and Materially Nonlinear Analysis with Imperfections included (GMNIA) using shell finite elements implemented in the software ABAQUS/CAE [107]. Material properties, assumed as in [76], are summarized in table 6.1.

### 6.2.1 Interaction points

Figs. 6.6 and 6.7 show the theoretical buckling curves obtained using GBT, respectively of the rack-section-members RSB125x3.2 and RSB95x2.6 both in compression with simple support-simple

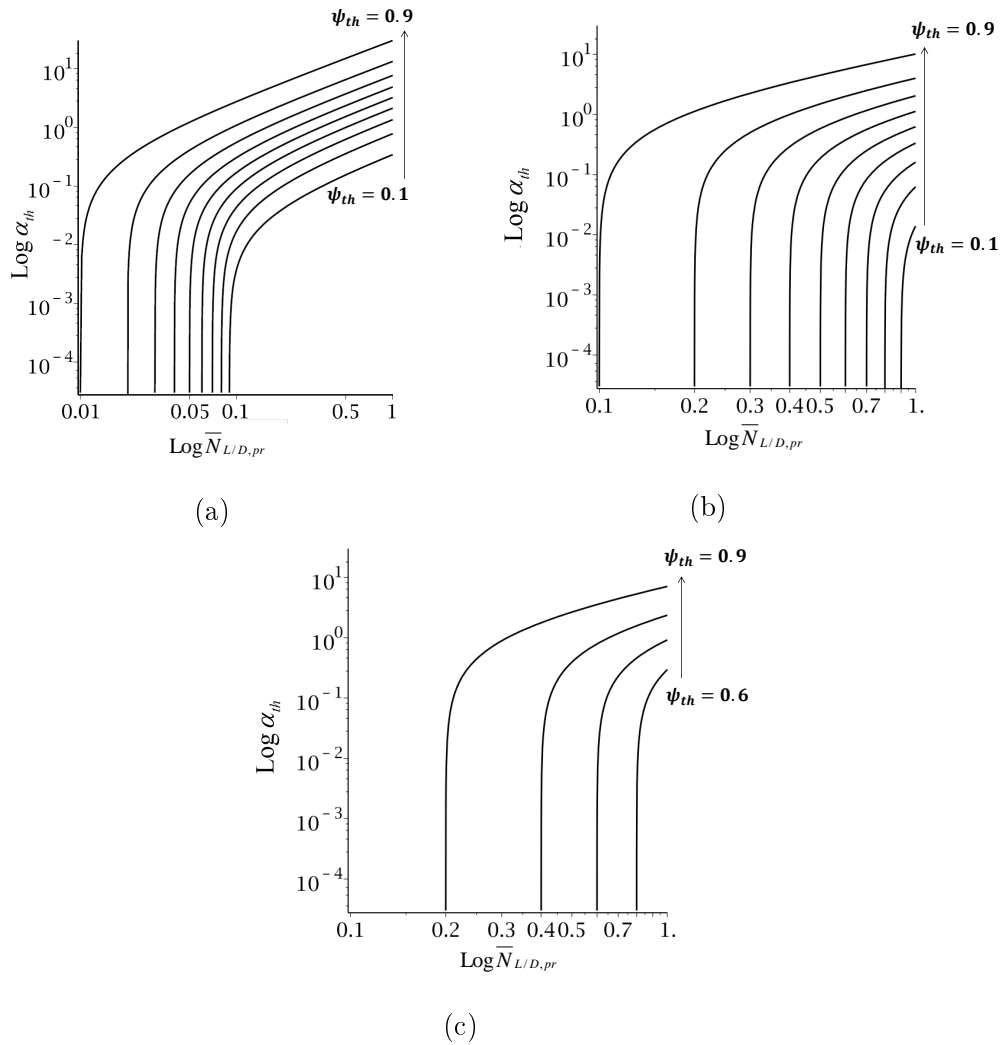


Figure 6.4: Variation of  $\alpha_{th}$  depending on  $\psi_{th}$  and  $\bar{N}_{L/D,pr}$  for a)  $\bar{N}_{L/D,th} = 0.1$   
 b)  $\bar{N}_{L/D,th} = 1.0$  c)  $\bar{N}_{L/D,th} = 2.0$ .

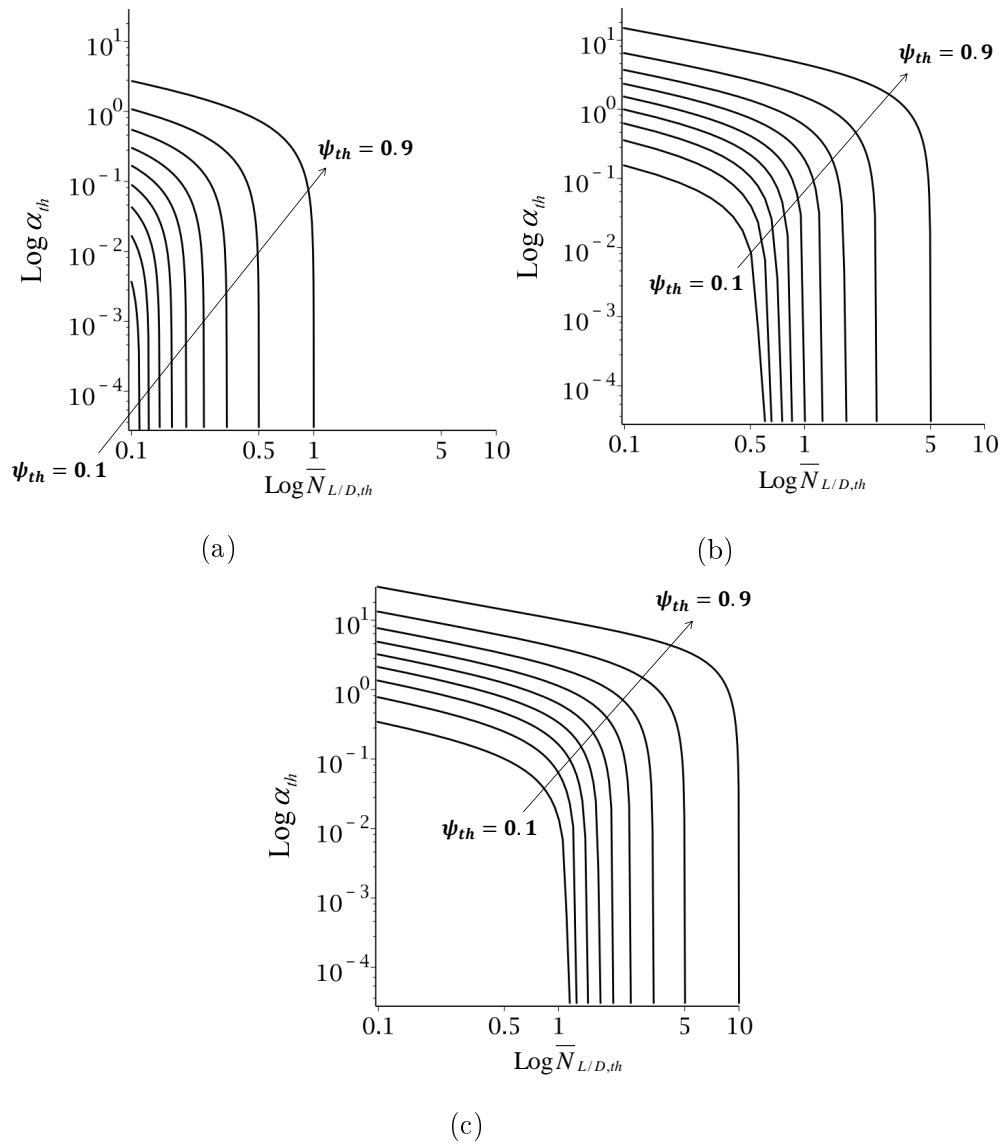


Figure 6.5: Variation of  $\alpha_{th}$  depending on  $\psi_{th}$  and  $\bar{N}_{L/D,th}$  for a)  $\bar{N}_{L/D,pr} = 0.1$   
 b)  $\bar{N}_{L/D,pr} = 0.5$  c)  $\bar{N}_{L/D,pr} = 1.0$ .

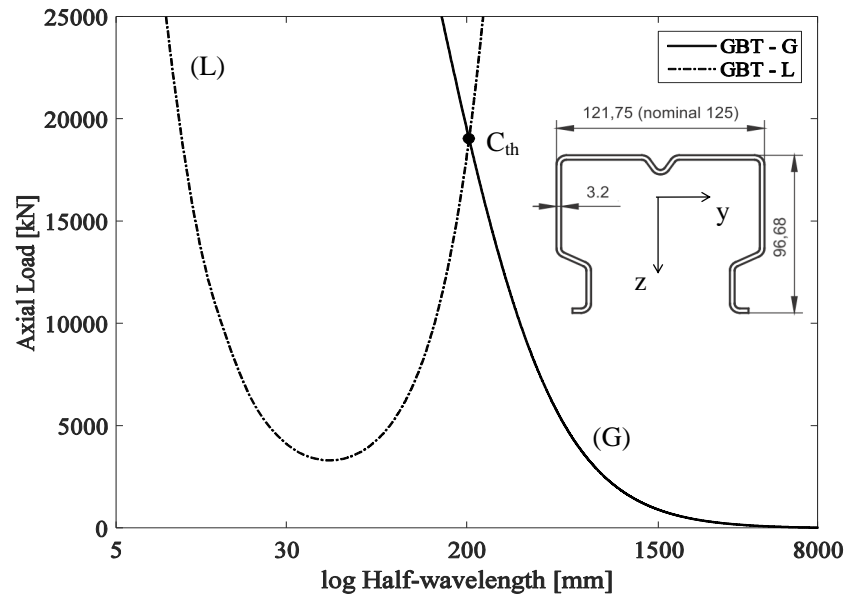
Table 6.1: Base material properties for studied sections (mean values).

Specimen	Yield strength [ $N/mm^2$ ]	Young modulus [ $N/mm^2$ ]	Ultimate strength [ $N/mm^2$ ]	Elongation at maximum load [%]
RSB95	461.41	207463.67	538.90	15.77
RSB125	465.18	202941.28	537.40	15.50

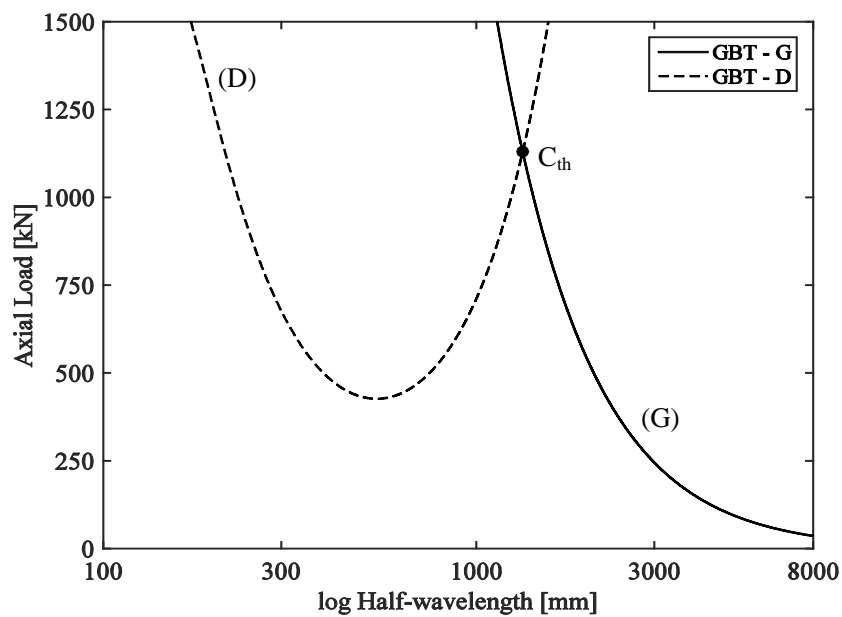
support boundary conditions. A distinction between Global-Local (GL) and Global-Distortional (GD) interaction points is made. The results show that the GD interaction points are characterized by lower critical loads with respect to GL interaction points for both cases. Accordingly, only the GD interaction points are considered in the following.

### 6.2.2 Erosion of buckling strength and ECBL buckling curves

As anticipated, in order to evaluate the ultimate load, GMNIA shell finite element analyses of the rack section members RSB125x3.2 and RSB95x2.6 in compression have been carried out using ABAQUS. In particular, rectangular 4-noded shell elements with reduced integration (S4R) have been used, with mesh size of about 5 mm x 5 mm. Two types of geometrical imperfections have been considered: overall geometric imperfection, with maximum size at the mid-length equal to 1/750 of column length (as proposed by ECCS Recommendations [108]), and local/distortional imperfection according to the Schafer and Peköz codification [109]. Restraints

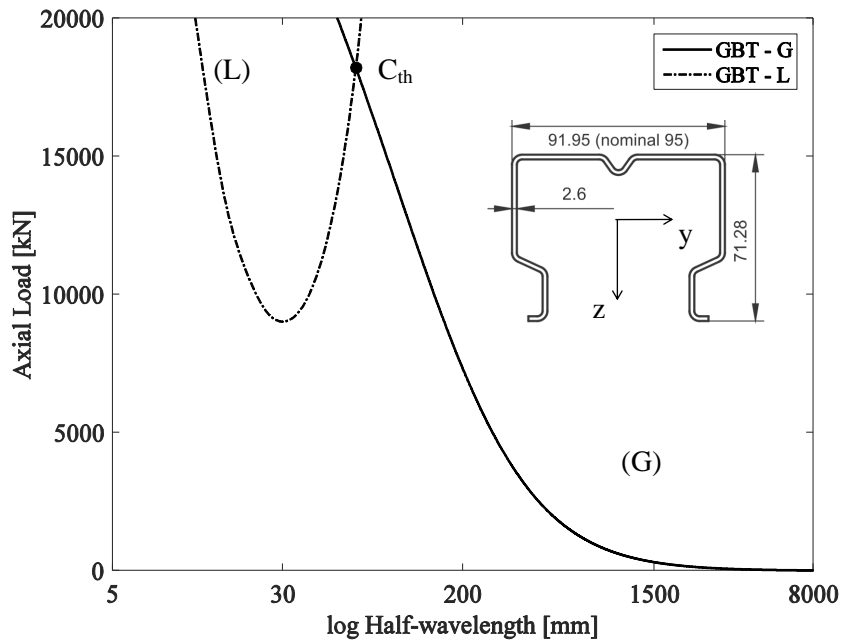


(a)

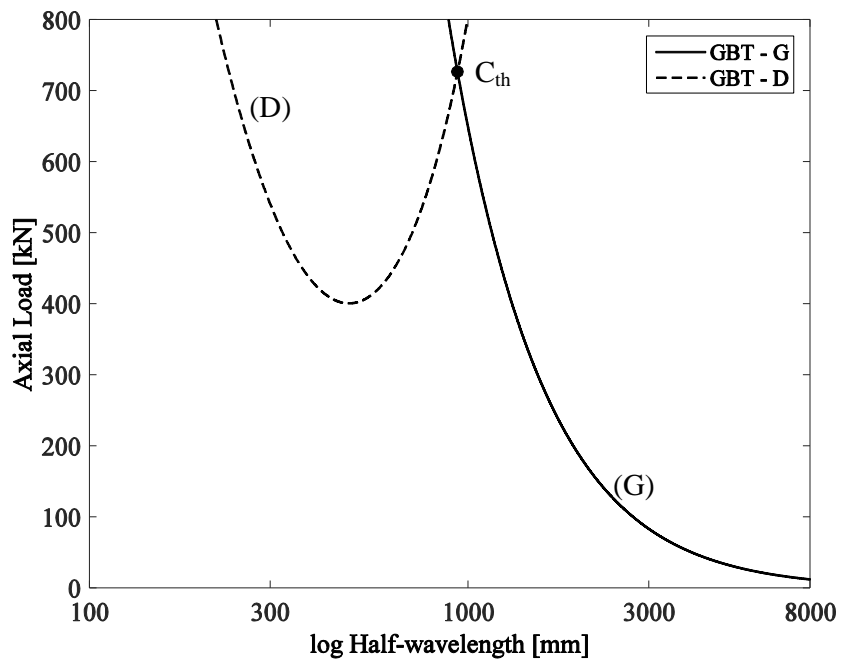


(b)

Figure 6.6: Theoretical buckling curves for RSB125x3.2: a) GL and b) GD.



(a)

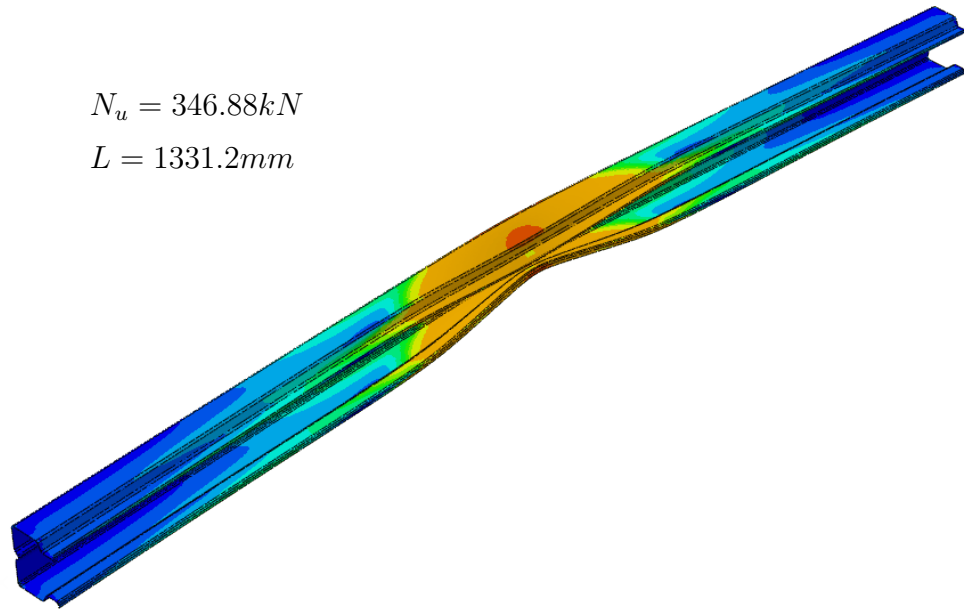


(b)

Figure 6.7: Theoretical buckling curves for RSB95x2.6: a) GL and b) GD.

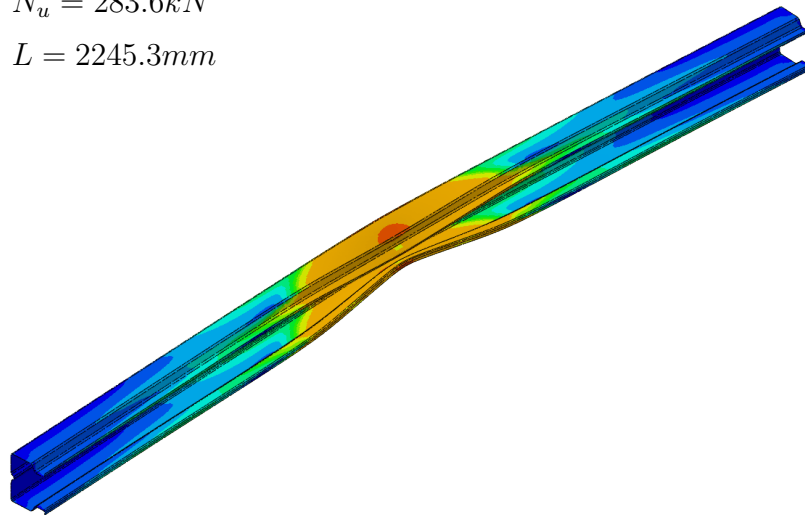
have been set to reproduce the simple supported boundary condition with warping and section distortion restrained at both beam ends. Only rotations about y-axis and z-axis were allowed on beam ends, torsion being prevented. The lengths of the specimen, were the lengths corresponding to (1)  $C_{th}$  interactive point to determine the theoretical erosion,  $\psi_{th}$  and (2)  $C_{pr}$  interactive point to determine the practical erosion,  $\psi_{pr}$ , as presented in Fig. 6.2. The analyses have been conducted into two steps. The first step consists in a GBT linear buckling analysis useful to find a buckling mode or combination of buckling modes affine with the relevant imperfections. Two buckling analyses for each case were performed: the first one using only classical global GBT modes to find a global imperfection shape and a second buckling analysis using only distortional GBT modes to find a distortional imperfection shape. After imposing the initial geometric imperfection, obtained as a scaled linear combination of buckling modes from the previous step, a GMNIA analysis with arc-length solver was performed to determine the ultimate load (Figs. 6.8, 6.9). The residual stresses, induced by the cold-forming process, are not considered because they have no significant influence on the ultimate strength of the member [77]. Once the ultimate loads, and hence  $\psi_{pr}$  and  $\psi_{th}$ , have been evaluated, the ECBL buckling curves have been obtained as described in Section 6.1. Figs. 6.10(a) and 6.11(a) shows the theoretical buckling curves obtained by the GBT, while the buckling curves calculated with both the  $ECBL_{pr}$  and the  $ECBL_{th}$  approaches are

shown in Fig. 6.10(b) and 6.11(b) and compared with the one obtained using the design according to EN15512:2009 [110]. The very good agreement between  $ECBL_{th}$  and experimental results can be observed. On the other hand,  $ECBL_{pr}$  and EN15512 results are not always on the safe side.



(a)

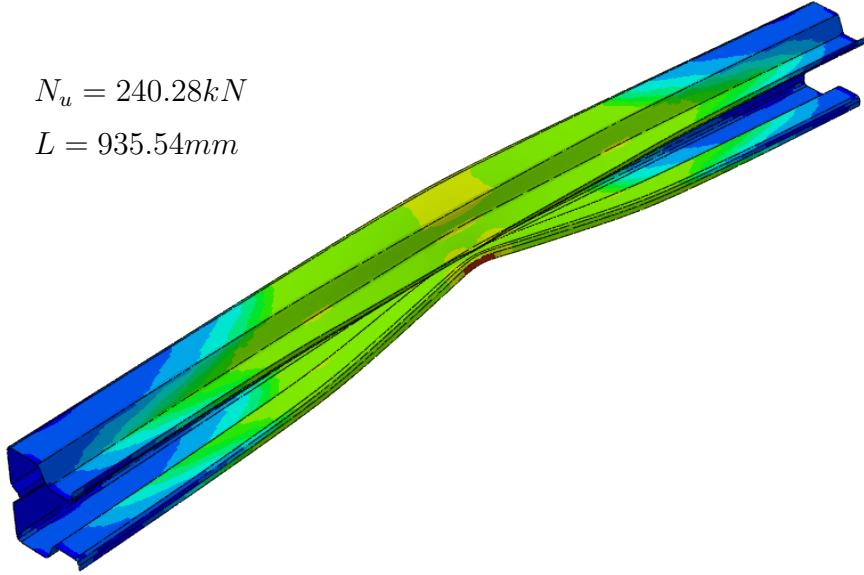
$N_u = 283.6kN$   
 $L = 2245.3mm$



(b)

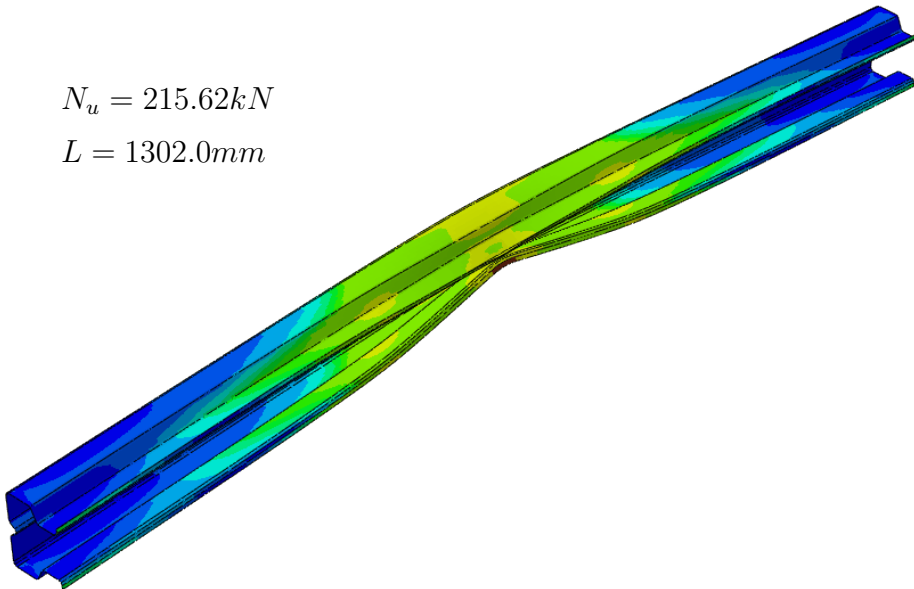
Figure 6.8: Failure mode for RSB125x3.2 in a)  $C_{th}$  and b)  $C_{pr}$ .

$$N_u = 240.28kN$$
$$L = 935.54mm$$



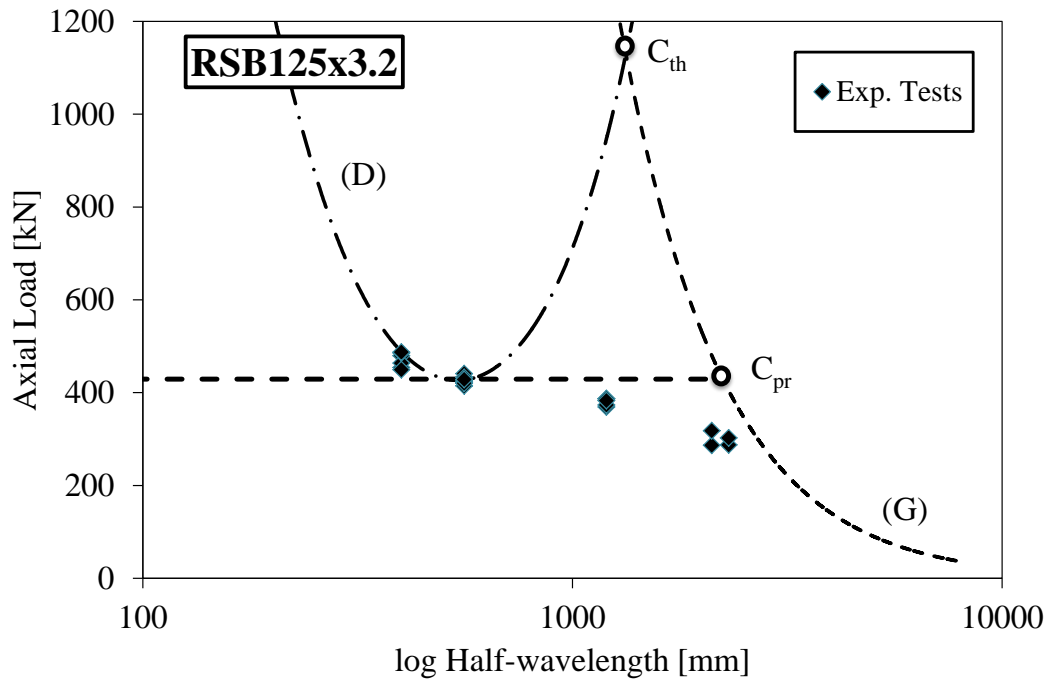
(a)

$$N_u = 215.62kN$$
$$L = 1302.0mm$$

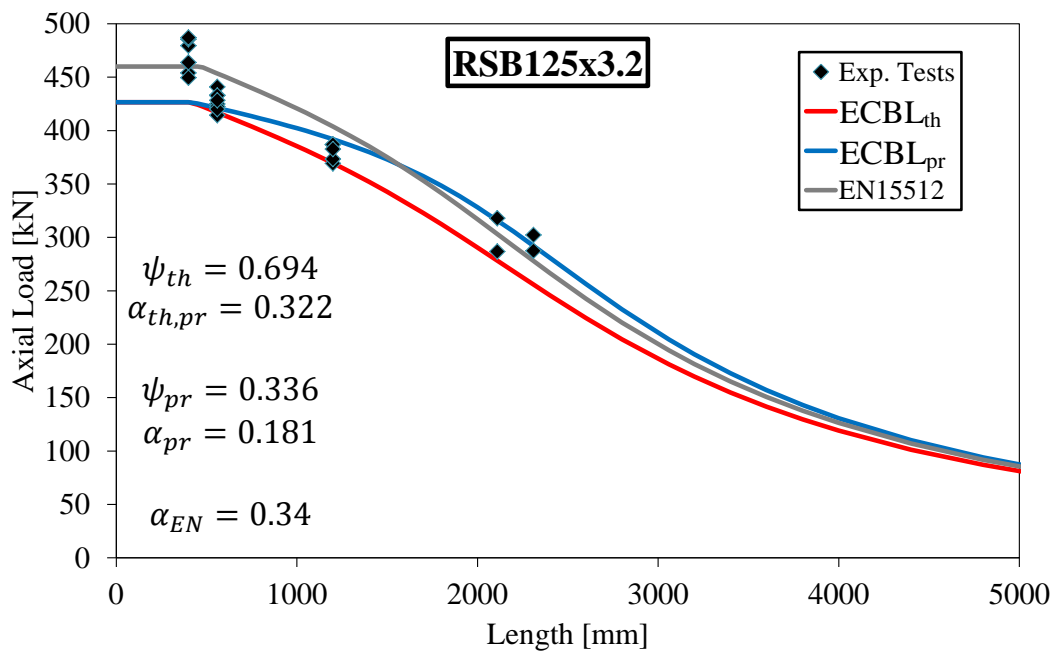


(b)

Figure 6.9: Failure mode for RSB95x2.6 in a)  $C_{th}$  and b)  $C_{pr}$ .

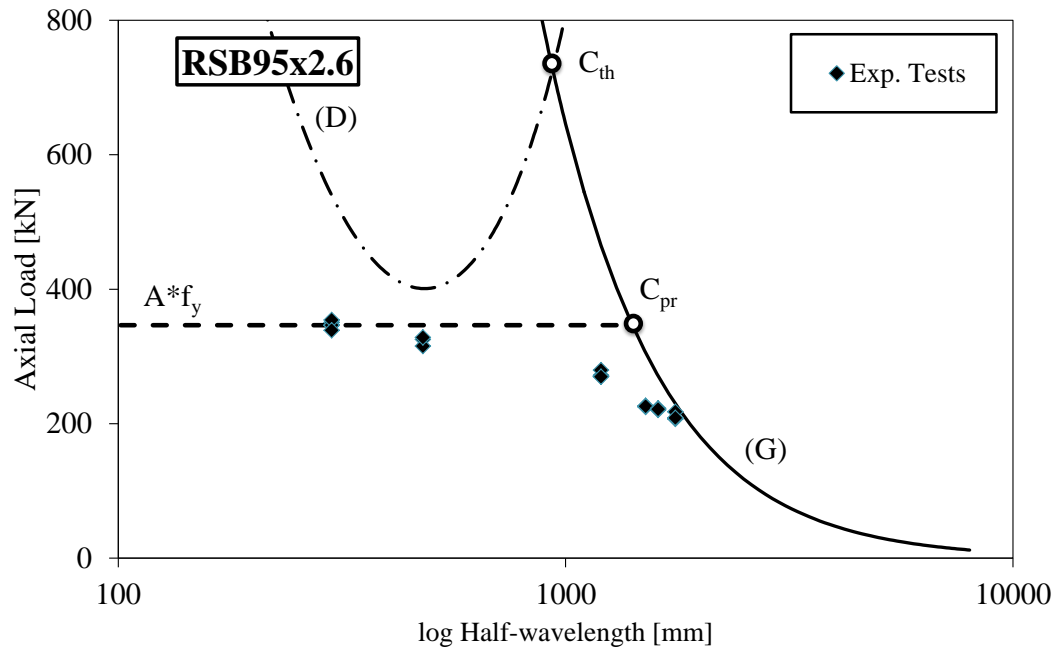


(a)

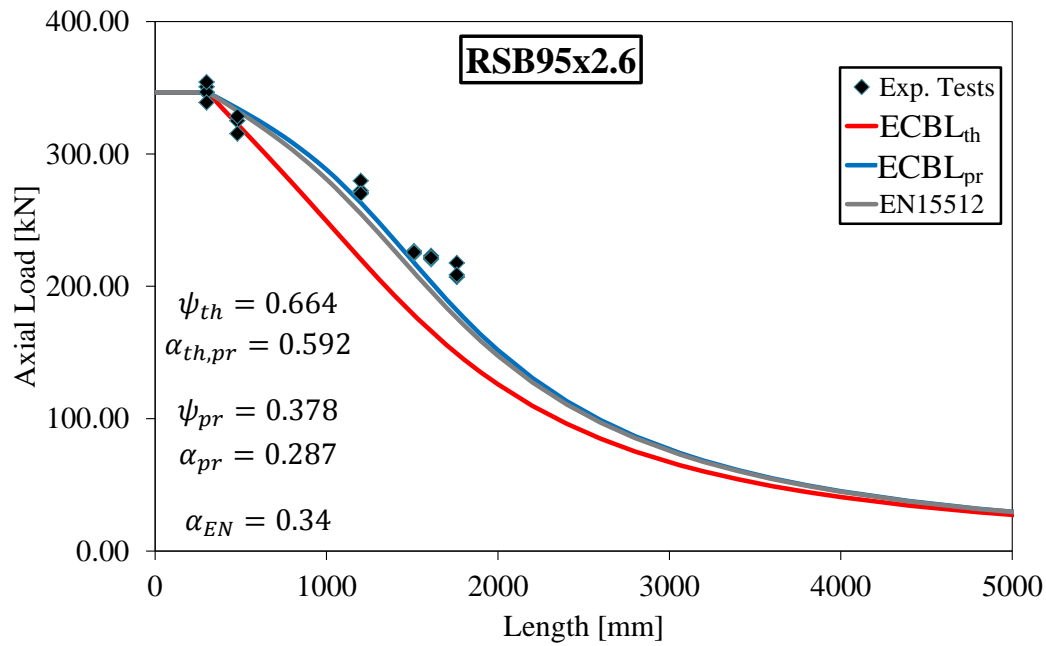


(b)

Figure 6.10: a) Theoretical buckling curves for RSB125x3.2 and b) buckling strength curves for RSB125x3.2.



(a)



(b)

Figure 6.11: a) Theoretical buckling curves for RSB95x2.6 and b) buckling strength curves for RSB95x2.6.

# Conclusions

In the thin-walled beams, bending, torsion, cross-section distortion and local effects act together in a coupled manner, leading to a complex mechanical behavior. In order to face this problem it is possible to use three-dimensional models or mono-dimensional beam models. Mono-dimensional beam models are simpler to use with respect to three-dimensional ones but it is necessary to look over the classical beam theories, not capable to describe the whole kinematics of thin-walled members, and consider more refined tools. At the same time, easy usage and good predictive capabilities are desired features of a tool available to the engineers in the everyday design. In this field, the Generalized Beam Theory (GBT) has been proven to account for section distortion and local effects (identifying these deformations in well defined cross-section mode families), along with classical beam kinematics, ensuring an easy interpretation of the results with a low computational cost.

In this thesis, after a quick review of the well-known approaches to describe the behavior of thin-walled members and an introduction to their mechanics (chapter 1), an overview on the evolution of the shear deformable GBT has been presented (chapter 2). In

particular, the attention has been focused on a recently proposed GBT formulation that solves the problem of a non-perfect coherence between bending and shear strain components and enables the possibility to establish a clear relationship between the GBT results and those of the classical beam theories. It is a crucial issue for a correct theoretical positioning of the GBT within the framework of the other existing beam theories as well as for the application of the GBT in the current engineering practice. This GBT formulation has been assumed as starting point for further developments discussed in the thesis.

Within the outlined framework, a new approach able to provide appropriate constitutive relations for GBT based beam models has been presented (chapter 3). The approach starts from a systematic classification of the internal constraints introduced by the GBT formulation and, basing on energetic arguments, is able to automatically take into account the effect of the adopted kinematics, providing constitutive relations which mitigate the over-stiffening of the model due to the adopted kinematic ansatz. Furthermore, it has been shown that the consistency between the stress and strain fields plays a crucial role in determining the performance of GBT models. In particular, such effect is proved to be particularly remarkable when orthotropic materials are considered due to the strong couplings induced by the constitutive relations. Adopting consistency as a conceptual framework, a detailed study of the role played by each of the cross-section deformation mode families, usually consid-

ered in GBT formulations, has been carried out highlighting that the use of all the mode families is needed in order to mitigate the consistency defects intrinsic in the GBT. Numerical results confirm the soundness of the approach by showing that inconsistent stress/strain fields lead to inaccurate results which can be predicted and efficiently improved within the proposed framework.

From the numerical point of view, the solution of the GBT equations is usually obtained resorting to the finite element method. With regard to this, a new 2-node flexibility-based GBT finite element has been presented in chapter 4. The formulation is rather simple and based on the hybrid complementary energy functional, involving nodal generalized displacements and equilibrating generalized stresses within each element. The stress approximation is rationally derived basing on analytical solutions of the GBT equations of some particular cases. Displacements in the element interior are a posteriori recovered using shape functions based the same analytical solutions and ruled by the standard nodal degrees of freedom. The final set of finite element equations has the typical format of assumed displacement finite elements. Hence, the element is easily implementable into existing finite element codes. Numerical results on some test problems evidence its excellent predictive capability for both displacements and stresses.

From a practical point of view, the thin-walled beams are usually made by cold-forming of steel laminates and commonly classified as Class 4 members. These members must be designed against

local/distortional buckling. In this framework, an approach for the design of thin-walled members undergoing distortional buckling has been presented in chapter 5. The proposed approach, called Embedded Stability Analysis (ESA), allows to perform stability checks on every type of thin-walled structural element, without limitations on section type, constraints or loads. In fact, the GBT, on which the proposed approach is based, allows to properly account for the global and distortional instability and to coherently consider the shear deformation of the elements, fulfilling all the specifications required by the codes to the designer. Numerical results show how the EuroCode3 simplified procedure is not always on the safety side, particularly when section distortion phenomena become relevant. Hence, a synthetic parameter allowing the designer to evaluate when it is more appropriate to consider the distortional effects in Class 4 thin-walled profiles stability checks has been provided.

Thin-walled members are also prone to the phenomenon of coupled instabilities (for example, two simultaneous buckling modes occur), inducing supplementary erosion of ideal buckling curves. On this regard, in chapter 6, basing on the use of the GBT to find the interaction points of simultaneous buckling modes and the related imperfections, a modified version of the Erosion of Critical Bifurcation Load (ECBL) approach has been discussed. The proposed approach has been applied to steel rack-section members, with RSB125x3.2 and RSB95x2.6 sections. Numerical results coming from both the classical and the modified ECBL approach have

been compared with experimental ones, showing that the modified ECBL approach is in very good agreement with experimental results, while results from the classical ECBL approach are not always on the safe side.



# Bibliography

- [1] Vlasov, V.Z.. Thin-walled elastic beams. 2nd ed Jerusalem, Israel: Israel Program for Scientific Translation 1961;doi:10.1007/s13398-014-0173-7.2. arXiv:arXiv:1011.1669v3.
- [2] Kang, Y.J., Yoo, C.H.. Thin-Walled Curved Beams. I: Formulation of Nonlinear Equations. Journal of Engineering Mechanics 1994;120(10):2072–2101. URL: [http://ascelibrary.org.ezproxy.uct.ac.za/doi/abs/10.1061/\(ASCE\)0733-9399\(1994\)120:10\(2072\).](http://ascelibrary.org.ezproxy.uct.ac.za/doi/abs/10.1061/(ASCE)0733-9399(1994)120:10(2072).) doi:10.1061/(ASCE)0733-9399(1994)120:10(2072).
- [3] Kim, M.H., Min, B.C., Suh, M.W.. Spatial stability of non-symmetric thin walled curved beams, I: analytical approach. Journal of Engineering Mechanics-ASCE 2000;126:497–505.
- [4] Wilson, J.F., Wang, Y., Threlfall, I.. Responses of near-optimal, continuous horizontally curved beams to transit loads. Journal of Sound and Vibration 1999;222(4):565–578. URL: <http://www.scopus.com/inward/record.url?eid=2-s2.0-0040477603{&}partnerID=tZ0tx3y1>.
- [5] Stavridis, L.T., Michaltsos, G.T.. Eigenfrequency

- analysis of thin-walled girders curved in plan. *Journal of Sound and Vibration* 1999;227(2):383–396. URL: <http://www.scopus.com/inward/record.url?eid=2-s2.0-0040882990&partnerID=tZ0tx3y1>.
- [6] Capurso, M.. Sul calcolo delle travi in parete sottile in presenza di forze e distorsioni. *La ricerca scientifica* 1964;6:241–286.
- [7] Capurso, M.. Influenza delle componenti di scorrimento nella deformazione delle travi di parete sottile con sezione aperta. *Giornale del Genio Civile* 1984;122:127–144.
- [8] Laudiero, F., Savoia, M.. Shear strain effects in flexure and torsion of thin-walled beams with open or closed cross-section. *Thin-Walled Structures* 1990;10(2):87–119. URL: <http://www.scopus.com/inward/record.url?eid=2-s2.0-0025245256&partnerID=tZ0tx3y1>. doi:10.1016/0263-8231(90)90058-7.
- [9] Laudiero, F., Savoia, M., Zaccaria, D.. The influence of shear deformations on the stability of thin-walled beams under non-conservative loading. *International Journal of Solids and Structures* 1991;27(11):1351–1370. URL: <http://www.scopus.com/inward/record.url?eid=2-s2.0-0025791219&partnerID=tZ0tx3y1>. doi:10.1016/0020-7683(91)90036-F.
- [10] Bauchau, O.A.. Beam theory for anisotropic

- materials. *Journal of Applied Mechanics, Transactions ASME* 1985;52(2):416–422. URL: <http://www.scopus.com/inward/record.url?eid=2-s2.0-0022078313&partnerID=tZ0tx3y1>.
- [11] De Lorenzis, L., La Tegola, A.. Effect of the actual distribution of applied stresses on global buckling of isotropic and transversely isotropic thin-walled members: Numerical examples. *Composite Structures* 2005;71(1):83–100. URL: <http://www.scopus.com/inward/record.url?eid=2-s2.0-24744444912&partnerID=tZ0tx3y1>. doi:10.1016/j.compstruct.2004.09.022.
- [12] Ferradi, M.K., Cespedes, X.. A new beam element with transversal and warping eigenmodes. *Computers & Structures* 2014;131:12–33. URL: <http://www.scopus.com/inward/record.url?eid=2-s2.0-84888052943&partnerID=tZ0tx3y1>. doi:10.1016/j.compstruc.2013.10.001.
- [13] Piovan, M.T., Cortínez, V.H., Rossi, R.E.. Out-of-plane vibrations of shear deformable continuous horizontally curved thin-walled beams. *Journal of Sound and Vibration* 2000;237(1):101–118. URL: <http://www.scopus.com/inward/record.url?eid=2-s2.0-0342906590&partnerID=tZ0tx3y1>. doi:10.1006/jsvi.2000.3055.
- [14] Gendy, A.S., Saleeb, A.F.. *Vibration Anal-*

- ysis of Coupled Extensional/Flexural/Torsional Modes of Curved Beams With Arbitrary Thin-Walled Sections. *Journal of Sound and Vibration* 1994;174(2):261–274. URL: <http://www.scopus.com/inward/record.url?eid=2-s2.0-0028767489&partnerID=tZ0tx3y1>. doi:10.1006/jsvi.1994.1275.
- [15] Kim, M.Y., Kim, S.B., Kim, N.I.. Spatial stability of shear deformable curved beams with non-symmetric thin-walled sections. I: Stability formulation and closed-form solutions. *Computers & Structures* 2005;83(31-32):2525–2541. URL: <http://www.scopus.com/inward/record.url?eid=2-s2.0-27344436958&partnerID=tZ0tx3y1>. doi:10.1016/j.compstruc.2005.07.004.
- [16] Carrera, E., Cinefra, M., Petrolo, M., Zappino, E.. *Finite element analysis of structures through Unified Formulation*. Wiley; 2014.
- [17] Genoese, A., Genoese, A., Bilotta, A., Garcea, G.. A generalized model for heterogeneous and anisotropic beams including section distortions. *Thin-Walled Structures* 2014;74:85–103. URL: <http://www.scopus.com/inward/record.url?eid=2-s2.0-84886517060&partnerID=tZ0tx3y1>. doi:10.1016/j.tws.2013.09.019.
- [18] Genoese, A., Genoese, A., Bilotta, A., Garcea, G.. Buckling analysis through a generalized beam model including

- section distortions. *Thin-Walled Structures* 2014;85:125–141. URL: <http://www.scopus.com/inward/record.url?eid=2-s2.0-84907553529{%&}partnerID=tZ0tx3y1>. doi:10.1016/j.tws.2014.08.012.
- [19] Schafer, B.W., Ádány, S.. Buckling analysis of cold-formed steel members using CUFSM: Conventional and constrained finite strip methods. In: *Eighteenth International Specialty Conference on Cold-Formed Steel Structures: Recent Research and Developments in Cold-Formed Steel Design and Construction*; vol. 2006. 2006, p. 39–54. URL: <http://www.scopus.com/inward/record.url?eid=2-s2.0-33846941186{%&}partnerID=tZ0tx3y1>.
- [20] Schardt, R.P.. *Verallgemeinerte Technische Biegetheorie*. Berlin: Springer; 1989.
- [21] Schardt, R.P.. Generalized Beam Theory - an adequate method for coupled stability problems. *Thin-Walled Structures* 1994;19:161–180.
- [22] Dinis, P.B., Camotim, D., Silvestre, N.. GBT formulation to analyse the buckling behaviour of thin-walled members with arbitrarily ‘branched’ open cross-sections. *Thin-Walled Structures* 2006;44(1):20–38. URL: <http://www.scopus.com/inward/record.url?eid=2-s2.0-32344440845{%&}partnerID=tZ0tx3y1>. doi:10.1016/j.tws.2005.09.005.

- [23] Gonçalves, R., Dinis, P.B., Camotim, D.. GBT formulation to analyse the first-order and buckling behaviour of thin-walled members with arbitrary cross-sections. *Thin-Walled Structures* 2009;47(5):583–600. URL: <http://www.scopus.com/inward/record.url?eid=2-s2.0-60949087415&partnerID=tZ0tx3y1>. doi:10.1016/j.tws.2008.09.007.
- [24] Davies, J.M., Leach, P., Heinz, D.. Second-order Generalized Beam Theory. *Journal of Constructional Steel Research* 1994;31:221–241.
- [25] Camotim, D., Basaglia, C., Silvestre, N.. GBT buckling analysis of thin-walled steel frames: A state-of-the-art report. *Thin-Walled Structures* 2010;48(10-11):726–743. URL: <http://www.scopus.com/inward/record.url?eid=2-s2.0-77954339350&partnerID=tZ0tx3y1>. doi:10.1016/j.tws.2009.12.003.
- [26] Bebiano, R., Camotim, D., Silvestre, N.. Dynamic analysis of thin-walled members using Generalised Beam Theory (GBT). *Thin-Walled Structures* 2013;72:188–205. doi:10.1016/j.tws.2013.07.004.
- [27] Andreassen, M.J., Jönsson, J.. A distortional semi-discretized thin-walled beam element. *Thin-Walled Structures* 2013;62:142–157. doi:10.1016/j.tws.2012.07.011.
- [28] de Miranda, S., Miletta, R., Ruggerini, A., Ubertini, F..

- On the numerical modeling of thin-walled cold-formed roof systems. In: Proceedings of the IV European Conference on Computational Mechanics. Paris, France; 2010, p. xx–xx.
- [29] Braham, M., Ruggerini, A., Ubertini, F.. A numerical model for roof detailing of cold-formed purlin-sheeting systems. *Stahlbau* 2008;77(4):238–246. URL: <http://www.scopus.com/inward/record.url?eid=2-s2.0-43049101161&partnerID=tZ0tx3y1>. doi:10.1002/stab.200810035.
- [30] de Miranda, S., Gutierrez, A., Miletta, R.. Equilibrium-based reconstruction of three-dimensional stresses in GBT. *Thin-Walled Structures* 2014;74:146–154. URL: <http://www.scopus.com/inward/record.url?eid=2-s2.0-84886678740&partnerID=tZ0tx3y1>. doi:10.1016/j.tws.2013.09.021.
- [31] Ádány, S., Silvestre, N., Schafer, B.W., Camotim, D.. GBT and cFSM: Two modal approaches to the buckling analysis of unbranched thin-walled members. In: *Advanced Steel Construction*; vol. 5. 2009, p. 195–223. URL: <http://www.scopus.com/inward/record.url?eid=2-s2.0-77952944047&partnerID=tZ0tx3y1>.
- [32] Silvestre, N., Camotim, D., Silva, N.F.. Generalized Beam Theory revisited: from the kinematical assumptions to the deformation mode determination. *International Journal*

- of Structural Stability and Dynamics 2011;11(05):969–997. URL: <http://www.scopus.com/inward/record.url?eid=2-s2.0-80052002124&partnerID=tZ0tx3y1>. doi:10.1142/S0219455411004427.
- [33] Garcea, G., Gonçalves, R., Bilotta, A., Manta, D., Bebiano, R., Leonetti, L., et al. Deformation modes of thin-walled members: A comparison between the method of Generalized Eigenvectors and Generalized Beam Theory. *Thin-Walled Structures* 2016;100:192–212. URL: <http://www.scopus.com/inward/record.url?eid=2-s2.0-84952815368&partnerID=tZ0tx3y1>. doi:10.1016/j.tws.2015.11.013.
- [34] Abambres, M., Camotim, D., Silvestre, N.. Physically non-linear GBT analysis of thin-walled members. *Computers and Structures* 2013;129:148–165. doi:10.1016/j.compstruc.2013.04.022.
- [35] Abambres, M., Camotim, D., Silvestre, N., Rasmussen, K.J.. GBT-based structural analysis of elastic–plastic thin-walled members. *Computers & Structures* 2014;136:1–23. URL: <http://www.scopus.com/inward/record.url?eid=2-s2.0-84894114194&partnerID=tZ0tx3y1>. doi:10.1016/j.compstruc.2014.01.001.
- [36] Abambres, M., Camotim, D., Silvestre, N.. Modal decomposition of thin-walled member collapse mech-

- anisms. Thin-Walled Structures 2014;74:269–291.  
URL: <http://www.scopus.com/inward/record.url?eid=2-s2.0-84888083035&partnerID=tZ0tx3y1>.  
doi:10.1016/j.tws.2013.10.002.
- [37] Nedelcu, M., Cucu, H.L.. Buckling modes identification from FEA of thin-walled members using only GBT cross-sectional deformation modes. Thin-Walled Structures 2014;81:150–158.  
doi:10.1016/j.tws.2013.06.007.
- [38] Nedelcu, M.. Buckling mode identification of perforated thin-walled members by using GBT and shell FEA. Thin-Walled Structures 2014;82:67–81. URL: <http://linkinghub.elsevier.com/retrieve/pii/S0263823114001189>  
doi:10.1016/j.tws.2014.04.005.
- [39] Casafont, M., Marimon, F., Pastor, M., Ferrer, M.. Linear buckling analysis of thin-walled members combining the Generalised Beam Theory and the Finite Element Method. Computers & Structures 2011;89(21-22):1982–2000. URL: <http://www.scopus.com/inward/record.url?eid=2-s2.0-80052948201&partnerID=tZ0tx3y1>.  
doi:10.1016/j.compstruc.2011.05.016.
- [40] Nedelcu, M.. GBT formulation to analyse the behaviour of thin-walled members with variable cross-section. Thin-

- Walled Structures 2010;48(8):629–638. doi:10.1016/j.tws.2010.03.001.
- [41] Nedelcu, M.. GBT formulation to analyse the buckling behaviour of isotropic conical shells. Thin-Walled Structures 2011;49(7):812–818. doi:10.1016/j.tws.2011.02.006.
- [42] Ranzi, G., Luongo, A.. A new approach for thin-walled member analysis in the framework of GBT. Thin-Walled Structures 2011;49(11):1404–1414. URL: <http://www.scopus.com/inward/record.url?eid=2-s2.0-80052268378&partnerID=tZ0tx3y1>. doi:10.1016/j.tws.2011.06.008.
- [43] Piccardo, G., Ranzi, G., Luongo, A.. A complete dynamic approach to the Generalized Beam Theory cross-section analysis including extension and shear modes. Mathematics and Mechanics of Solids 2013;19(8):900–924. URL: <http://www.scopus.com/inward/record.url?eid=2-s2.0-84910075054&partnerID=tZ0tx3y1>. doi:10.1177/1081286513493107.
- [44] Silvestre, N., Camotim, D.. Nonlinear Generalized Beam Theory for cold-formed steel members. International Journal of Structural Stability and Dynamics 2003;3:461–490.
- [45] Silvestre, N., Camotim, D.. Influence of shear deformation on the local and global buckling behaviour of composite

- thin-walled members. In: Loughlan, J., editor. Thin-walled structures: advances in research, design and manufacturing technology. Bristol: Institute of Physics Publishing; 2004, p. 659–668.
- [46] de Miranda, S., Gutiérrez, A., Miletta, R., Ubertini, F.. A generalized beam theory with shear deformation. *Thin-Walled Structures* 2013;67:88–100. URL: <http://www.scopus.com/inward/record.url?eid=2-s2.0-84875202123&partnerID=tZ0tx3y1>. doi:10.1016/j.tws.2013.02.012.
- [47] de Miranda, S., Madeo, A., Miletta, R., Ubertini, F.. On the relationship of the shear deformable Generalized Beam Theory with classical and non-classical theories. *International Journal of Solids and Structures* 2014;51(21-22):3698–3709. URL: <http://www.scopus.com/inward/record.url?eid=2-s2.0-84906948329&partnerID=tZ0tx3y1>. doi:10.1016/j.ijsolstr.2014.07.001.
- [48] Silva, N.F., Silvestre, N., Camotim, D.. GBT formulation to analyse the buckling behaviour of FRP composite open-section thin-walled columns. *Composite Structures* 2010;93(1):79–92. URL: <http://www.scopus.com/inward/record.url?eid=2-s2.0-77955273064&partnerID=tZ0tx3y1>. doi:10.1016/j.compstruct.2010.06.013.
- [49] Silva, N.F., Silvestre, N., Camotim, D.. On the influence of

- the constitutive law modelling on the structural behaviour of composite plates and members. In: et Al., C.d.S.J., editor. Numerical and computational methods in engineering. Porto; 2007, p. xx–xx.
- [50] Silva, N.F.. Behaviour and Strength of Thin-Walled Laminated FRP Composite Structural Elements. Ph.d. thesis; Universidade Tecnica de Lisboa; 2013.
- [51] De Miranda, S., Gutierrez, A., Melchionda, D., Patruno, L.. Linearly elastic constitutive relations and consistency for GBT-based thin-walled beams. *Thin-Walled Structures* 2015;92:55–64. doi:10.1016/j.tws.2015.02.022.
- [52] Prathap, G.. *The Finite Element Method in Structural Mechanics*. Kluwer Academic; 1993.
- [53] Patel, B.P., Ganapathi, M., Saravanan, J.. Shear flexible field-consistent curved spline beam element for vibration analysis. *International Journal for Numerical Methods in Engineering* 1999;46(3):387–407. URL: <http://www.scopus.com/inward/record.url?eid=2-s2.0-0032689418&partnerID=tZ0tx3y1>.
- [54] Marur, S.R., Prathap, G.. Consistency and correctness evaluation of shear deformable anisoparametric formulations. *International Journal of Solids and Structures* 2000;37(5):701–713. URL: <http://www.scopus.com/inward/record.url?eid=2-s2.0-0033883030&partnerID=tZ0tx3y1>.

- [55] De Miranda, S., Ubertini, F.. On the consistency of finite element models in thermoelastic analysis. *Computer Methods in Applied Mechanics and Engineering* 2001;190(18-19):2411–2427. doi:10.1016/S0045-7825(00)00244-9.
- [56] de Miranda, S., Ubertini, F.. Consistency and recovery in electroelasticity Part I: Standard finite elements. *Computer Methods in Applied Mechanics and Engineering* 2003;192(7-8):831–850. doi:10.1016/S0045-7825(02)00600-X.
- [57] de Miranda, S., Ubertini, F.. Consistency and recovery in electroelasticity. Part II: Equilibrium and mixed finite elements. *Computer Methods in Applied Mechanics and Engineering* 2004;193(23-26):2155–2168. doi:10.1016/j.cma.2004.01.014.
- [58] De Miranda, S., Ubertini, F.. Recovery of consistent stresses for compatible finite elements. *Computer Methods in Applied Mechanics and Engineering* 2002;191(15-16):1595–1609. doi:10.1016/S0045-7825(01)00338-3.
- [59] Erkmén, R.E.. Shear deformable hybrid finite-element formulation for buckling analysis of thin-walled members. *Finite Elements in Analysis and Design* 2014;82:32–45. URL: <http://www.scopus.com/inward/record.url?eid=2-s2.0-84892598633&partnerID=tZ0tx3y1>. doi:10.1016/j.finel.2013.12.005.
- [60] Molari, L., Ubertini, F.. A flexibility-based finite element for

- linear analysis of arbitrarily curved arches. *International Journal for Numerical Methods in Engineering* 2006;65(8):1333–1353. URL: <http://www.scopus.com/inward/record.url?eid=2-s2.0-32444441456&partnerID=tZ0tx3y1>. doi:10.1002/nme.1497.
- [61] Pian, T.H.H., Sze, K.Y.. Hybrid Stress Finite Element Methods for Plate and Shell Structures. *Advances in Structural Engineering* 2001;4(1):13–18. URL: <http://www.scopus.com/inward/record.url?eid=2-s2.0-0035247912&partnerID=tZ0tx3y1>. doi:10.1260/1369433011502309.
- [62] Madeo, A., Zagari, G., Casciaro, R., de Miranda, S.. A Mixed 4-Node 3D Plate Element Based on Self-Equilibrating Isostatic Stresses. *International Journal of Structural Stability and Dynamics* 2015;15(04):1450066. URL: <http://www.scopus.com/inward/record.url?eid=2-s2.0-84929207956&partnerID=tZ0tx3y1>. doi:10.1142/S0219455414500667.
- [63] de Miranda, S., Madeo, A., Melchionda, D., Ubertini, F.. A high performance flexibility-based GBT finite element. *Computers & Structures* 2015;158:285–307. URL: <http://www.scopus.com/inward/record.url?eid=2-s2.0-84934780308&partnerID=tZ0tx3y1>. doi:10.1016/j.compstruc.2015.06.010.

- 
- [64] EN 1993-1-3:2006(E) Part 1-3 Supplementary rules for cold formed members and sheeting. Brussels; 2006.
- [65] UNI EN 1993-1-3, Progettazione delle strutture in acciaio - Parte 1-3: Regole generali - Regole supplementari per l'impiego dei profilati e delle lamiere sottili piegati a freddo. Brussels; 2005.
- [66] AS/NZS 4600, Cold-formed steel structures. Sydney, Wellington; 2005.
- [67] NAS, North American Specification for the design of cold-formed steel structural members (AISI-S100-07). Washington DC; 2004.
- [68] JGJ 227-2011, Technical specification for low-rise cold-formed thin-walled steel structures. Beijing; 2011.
- [69] de Miranda, S., Melchionda, D., Miletta, R., Ruggerini, A., Ubertini, F.. Design of thin-walled members undergoing distortional buckling: A simple EC3-compliant approach based on the GBT. In: EuroSteel. Napoli, Italy; 2014, p. xx-xx.
- [70] van der Neut, A.. The interaction of local buckling and column failure of thin-walled compression members. In: Heteny M.K., V.W., editor. 12th Int. Congress on Applied Mechanics, Heteny M.K., Vincenti W.G. (eds.). Berlin: Springer-Verlag; 1969, p. 389-399.

- [71] Dubina, D., Ungureanu, V.. Instability mode interaction: From Van Der Neut model to ECBL approach. *Thin-Walled Structures* 2014;81:39–49.  
URL: <http://www.scopus.com/inward/record.url?eid=2-s2.0-84900822132&partnerID=tZ0tx3y1>.  
doi:10.1016/j.tws.2013.10.014.
- [72] Gioncu, V.. General theory of coupled instabilities. *Thin-Walled Structures* 1994;19(2-4):81–127.  
URL: <http://www.scopus.com/inward/record.url?eid=2-s2.0-0028712925&partnerID=tZ0tx3y1>.  
doi:10.1016/0263-8231(94)90024-8.
- [73] Dubina, D.. The ECBL approach for interactive buckling of thin-walled steel members. *Steel and Composite Structures* 2001;1:75–96.
- [74] Rondal, J., Maquoi, R.. Formulations d'Ayrton-Perry pour le flambement des barres metalliques. 1979.  
URL: <http://www.scopus.com/inward/record.url?eid=2-s2.0-0018737773&partnerID=tZ0tx3y1>.
- [75] de Miranda, S., Melchionda, D., Ungureanu, V., Dubina, D.. GBT-based buckling analysis of rack systems in the framework of ECBL approach. In: *Stability of Structure 14th Symposium SSK*. Zakopane, Poland; 2015, p. xx–xx.
- [76] Crisan, A., Ungureanu, V., Dubina, D.. Behaviour of cold-formed steel perforated sections in compression. Part

- 1—Experimental investigations. *Thin-Walled Structures* 2012;61:86–96. URL: <http://www.scopus.com/inward/record.url?eid=2-s2.0-84867681327&partnerID=tZ0tx3y1>. doi:10.1016/j.tws.2012.07.016.
- [77] Crisan, A., Ungureanu, V., Dubina, D.. Behaviour of cold-formed steel perforated sections in compression: Part 2—numerical investigations and design considerations. *Thin-Walled Structures* 2012;61:97–105. URL: <http://www.scopus.com/inward/record.url?eid=2-s2.0-84867665740&partnerID=tZ0tx3y1>. doi:10.1016/j.tws.2012.07.013.
- [78] Winter, G.. Performance of Compression Plates as Parts of Structural Members. *Research, Engineering Structures Supplement, Colston Papers* 1949;2:179.
- [79] Dubina, D., Ungureanu, V., Landolfo, R.. Design of cold-formed steel structures. *ECCS – European Convention for Constructional Steelwork*; 2012.
- [80] Rhodes, J.. *Design of Cold-Formed Steel Members*. London and New York: Elsevier Applied Science; 1991.
- [81] Bivolaru, D.. Numerical methods and technical experimentation in determination of residual stresses in cold-formed profiles. Ph.D. thesis; University of Liege; 1993.

- [82] Timoshenko, S.P., Gere, J.M.. Theory of Elastic Stability. New York: McGraw-Hill; 1961.
- [83] Murray, N.W.. Introduction to the Theory of Thin-Walled Structures. New York: Oxford University Press; 1984.
- [84] De Lorenzis, L., La Tegola, A.. Static behavior of pultruded fiber-reinforced polymer thin-walled beams. Composite Structures 2003;60(3):231–244. URL: <http://www.scopus.com/inward/record.url?eid=2-s2.0-0037404709&partnerID=tZ0tx3y1>. doi:10.1016/S0263-8223(03)00017-5.
- [85] Genoese, A., Genoese, A., Bilotta, A., Garcea, G.. A mixed beam model with non-uniform warpings derived from the Saint Venant rod. Computers & Structures 2013;121:87–98. URL: <http://www.scopus.com/inward/record.url?eid=2-s2.0-84876545963&partnerID=tZ0tx3y1>. doi:10.1016/j.compstruc.2013.03.017.
- [86] Genoese, A., Genoese, A., Bilotta, A., Garcea, G.. A composite beam model including variable warping effects derived from a generalized Saint Venant solution. Composite Structures 2014;110(1):140–151. URL: <http://www.scopus.com/inward/record.url?eid=2-s2.0-84893005077&partnerID=tZ0tx3y1>. doi:10.1016/j.compstruct.2013.11.020.
- [87] Garcea, G., Madeo, A., Zagari, G., Casciaro,

- R.. Asymptotic post-buckling FEM analysis using corotational formulation. *International Journal of Solids and Structures* 2009;46(2):377–397.  
URL: <http://www.scopus.com/inward/record.url?eid=2-s2.0-55649083295&partnerID=tZ0tx3y1>.  
doi:10.1016/j.ijsolstr.2008.08.038.
- [88] Garcea, G., Madeo, A., Casciaro, R.. The implicit corotational method and its use in the derivation of non-linear structural models for beams and plates. *Journal of Mechanics of Materials and Structures* 2012;7(6):509–538. URL: <http://www.scopus.com/inward/record.url?eid=2-s2.0-84872816970&partnerID=tZ0tx3y1>.  
doi:10.2140/jomms.2012.7.509.
- [89] Carrera, E., Filippi, M., Mahato, P.K., Pagani, A.. Accurate static response of single- and multi-cell laminated box beams. *Composite Structures* 2016;136:372–383. URL: <http://www.scopus.com/inward/record.url?eid=2-s2.0-84945583475&partnerID=tZ0tx3y1>.  
doi:10.1016/j.compstruct.2015.10.020.
- [90] Dan, M., Pagani, A., Carrera, E.. Free vibration analysis of simply supported beams with solid and thin-walled cross-sections using higher-order theories based on displacement variables. *Thin-Walled Structures* 2016;98:478–495. URL: <http://www.scopus.com/inward/record>.

- url?eid=2-s2.0-84945403683{&}partnerID=tZ0tx3y1.  
doi:10.1016/j.tws.2015.10.012.
- [91] Cheung, Y.K., Tham, L.G.. The Finite Strip Method. Florida: CRC Press; 1997.
- [92] Kantorovich, L.V., Kyrlov, V.I.. Approximate method of higher analysis. New York: Interscience Publishers; 1958.
- [93] Silvestre, N., Camotim, D.. GBT-based local and global vibration analysis of loaded composite open-section thin-walled members. International Journal of Structural Stability and Dynamics 2006;06(01):1–29. URL: <http://www.scopus.com/inward/record.url?eid=2-s2.0-33644991606{&}partnerID=tZ0tx3y1>. doi:10.1142/S0219455406001800.
- [94] Silva, N.F., Silvestre, N.. On the influence of material couplings on the linear and buckling behavior of I-section composite columns. International Journal of Structural Stability and Dynamics 2007;07(02):243–272. URL: <http://www.scopus.com/inward/record.url?eid=2-s2.0-34250725947{&}partnerID=tZ0tx3y1>. doi:10.1142/S0219455407002307.
- [95] Silvestre, N., Camotim, D.. Shear Deformable Generalized Beam Theory for the Analysis of Thin-Walled Composite Members. Journal of Engineering Mechanics 2013;139(8):1010–1024. URL:

<http://www.scopus.com/inward/record.url?eid=2-s2.0-84881327537&partnerID=tZ0tx3y1>.  
doi:10.1061/(ASCE)EM.1943-7889.0000506.

- [96] Zagari, G., Madeo, A., Casciaro, R., de Miranda, S., Ubertini, F.. Koiter analysis of folded structures using a corotational approach. *International Journal of Solids and Structures* 2013;50(5):755–765.  
URL: <http://www.scopus.com/inward/record.url?eid=2-s2.0-84872932805&partnerID=tZ0tx3y1>.  
doi:10.1016/j.ijsolstr.2012.11.007.

- [97] Jönsson, J., Andreassen, M.J.. Distortional eigenmodes and homogeneous solutions for semi-discretized thin-walled beams. *Thin-Walled Structures* 2011;49(6):691–707. URL: <http://www.scopus.com/inward/record.url?eid=2-s2.0-79953647058&partnerID=tZ0tx3y1>.  
doi:10.1016/j.tws.2010.12.009.

- [98] Kim, N.I., Ku Shin, D., Kim, M.Y.. Exact solutions for thin-walled open-section composite beams with arbitrary lamination subjected to torsional moment. *Thin-Walled Structures* 2006;44(6):638–654.  
URL: <http://www.scopus.com/inward/record.url?eid=2-s2.0-33746225531&partnerID=tZ0tx3y1>.  
doi:10.1016/j.tws.2006.05.001.

- [99] Piovan, M.T., Cortínez, V.H.. *Mechanics of thin-walled*

- curved beams made of composite materials, allowing for shear deformability. *Thin-Walled Structures* 2007;45(9):759–789. URL: <http://www.scopus.com/inward/record.url?eid=2-s2.0-35548977690&partnerID=tZ0tx3y1>. doi:10.1016/j.tws.2007.06.005.
- [100] Sheukh, A., Thomsen, O.. An efficient beam element for the analysis of laminated composite beams of thin-walled open and closed cross sections. *Composites Science and Technology* 2008;68(10-11):2273–2281. URL: <http://www.scopus.com/inward/record.url?eid=2-s2.0-44749088385&partnerID=tZ0tx3y1>. doi:10.1016/j.compscitech.2008.04.018.
- [101] Code\_Aster. 2015. URL: <http://www.code-aster.org/>.
- [102] de Miranda, S., Ubertini, F.. A simple hybrid stress element for shear deformable plates. *International Journal for Numerical Methods in Engineering* 2006;65(6):808–833. URL: <http://www.scopus.com/inward/record.url?eid=2-s2.0-31644435915&partnerID=tZ0tx3y1>. doi:10.1002/nme.1467.
- [103] Yuan, K.Y., Huang, Y.S., Pian, T.H.H.. New strategy for assumed stresses for 4-node hybrid stress membrane element. *International Journal for Numerical Methods in Engineering* 1993;36(10):1747–1763.

- URL: <http://www.scopus.com/inward/record.url?eid=2-s2.0-0027589789&partnerID=tZ0tx3y1>.
- [104] Pian, T.H.H.. Hybrid models. In: S.J. Fenves, R. Perrone, R. Robinson, W., Schonbrich, , editors. Numerical and Computer Methods in Structural Mechanics. New York: Academic Press; 1973, p. 50–80.
- [105] Rendek, S., Baláž, I.. Distortion of thin-walled beams. *Thin-Walled Structures* 2004;42(2):255–277. URL: <http://www.scopus.com/inward/record.url?eid=2-s2.0-0344874691&partnerID=tZ0tx3y1>. doi:10.1016/S0263-8231(03)00059-4.
- [106] Miletta, R.. Travi in parete sottile con deformabilità a taglio e distorsione di sezione: formulazione teorica, modellazione numerica e applicazioni. Ph.D. thesis; Bologna; 2013.
- [107] Hibbit, D., Karlson, B., Sorenson, P.. ABAQUS, Theory manual. 2007.
- [108] European recommendations for the design of light gauge steel members. Brussels; 1987.
- [109] Schafer, B.W., Peköz, T.. Computational modeling of cold-formed steel: Characterizing geometric imperfections and residual stresses. *Journal of Constructional Steel Research* 1998;47(3):193–210. URL:

---

<http://www.scopus.com/inward/record.url?eid=2-s2.0-0032156660&partnerID=tZ0tx3y1>.

- [110] EN 15512, Steel static storage systems - adjustable pallet racking systems - principles for structural design. Brussels; 2009.